No. 71 February 2017

CLIVAR Exchanges

CLIVAR Open Science Conference Award Winners

Participants of the CLIVAR Early Career Scientists Symposium, FIO/SOA, Qingdao, China

CLIVAR Ocean and Climate: Variability, Predictability and Change is the World Climate Research Programme's core project on the Ocean-Atmosphere System

WCRP World Climate Research Programme
WMO IOC ICSU International Council for Science

Editorial

Nico Caltabiano

International CLIVAR Project Office, Southampton, UK

The past year was an amazing year for CLIVAR. The celebration of our 20 years of success culminated with the CLIVAR Open Science Conference in September. Almost 700 scientists from 50 countries gathered in Qingdao, China, and over the course of five days, scientists showcased major advances in climate and ocean research. By design, more than one third of participants were early career scientists, who presented their work through 234 posters and oral presentations, including plenary talks.

One of the important aims of the conference was to engage the future generation. Jointly with the OSC, CLIVAR successfully organized an Early Career Scientists Symposium (ECSS), hosted by China's First Institute of Oceanography (SOA/FIO). More than 120 students and early career scientists participated in the symposium. Participants enjoyed an informal atmosphere, while discussing in groups the key research challenges that the scientific climate community faces at the moment and highlighting the need for international science collaboration. They also discussed the best ways to engage potential stakeholders with their scientific information and suggested their vision for the future of CLIVAR. I would like to say a big thank you to all those involved in the organisation of the ECSS. Without them, the success of the symposium would not have been possible.

The conference injected an amazing degree of enthusiasm about CLIVAR's research and fortified the notion that CLIVAR is and will be critical to meet society's needs for climate information. International cooperation of the type that CLIVAR fosters will continue to be indispensable to developing the human capacity and infrastructure that underpin all major scientific breakthroughs. The conference certainly helped in handing over the enthusiasm for CLIVAR and its science to the next generation, whose excitement is a promise for a very bright future. This issue of Exchanges showcases some of high quality research done by young researchers that were presented with outstanding poster awards at the OSC. A team of over 50 senior and early career scientists reviewed the 234 qualifying posters, and the full list of winners can be seen at this url: http://www.clivar.org/news/clivar-osc-poster-awards.

Also, this past year saw the departure of Valery Detemmerman from the ICPO. Valery has supported CLIVAR activities for more than two decades, initially from her position at the WCRP's Joint Planning Staff (JPS) in Geneva, and then as the Executive Director of the ICPO in Qingdao, since 2014. Valery is now enjoying a well deserved retirement, and her always optimistic approach will be missed by all in the CLIVAR community.

But we are also pleased that, after an extensive search, we would like to welcome the new Executive Director of the International CLIVAR Project Office (ICPO), José Luis Santos Davila. José obtained his Ph.D. in Atmospheric Sciences from the Georgia Institute of Technology of Atlanta, USA in 1995. He has been a Professor at the Marine Sciences and Maritime Engineering Department of the Escuela Superior Politecnica del Litoral, located in Guayaquil, Ecuador since 1989. He was the Director of the International Research Center on El Niño (CIIFEN) between 2002-2005. His current research interest are El Niño-Southern Oscillation variability and impacts, and Climate Change and variability on tropical areas. The ICPO Executive Director will be based at the International CLIVAR Global Project Office, generously hosted at the First Institute of Oceanography (FIO), in Qingdao, China. José will move to Qingdao and officially start on his position at the beginning of April.

Reflections on the CLIVAR Early Career Scientists Symposium 2016

Noel C. Baker, Eric Behrens, Julius Busecke, Victor Dike, Jonathan V. Durgadoo, Ariane Frassoni, Sarah Kang, Gaby Langendijk, Debashis Nath, Kevin Reed, Neil Swart

The CLIVAR Early Career Scientists Symposium was hosted by the First Institute of Oceanography in Qingdao, China, on September 18 and 24-25, 2016. 135 early career scientists (ECS) from 34 countries participated. The first day of the symposium provided the opportunity for ECS to network with peers and senior scientists, to become familiar with the institutional structure of CLIVAR, and to prepare for the upcoming Open Science Conference (OSC). During the weekend following the OSC, the symposium served as a forum to actively engage the ECS and challenge them to find solutions to critical issues in atmospheric and ocean science. Participants worked in diverse international teams to complete the following tasks: highlight key research challenges and goals; identify major challenges facing international science collaboration; discuss how to effectively engage the audience of their scientific information; and suggest their vision for the future of CLIVAR.

As the next generation of scientists, the ECS participants recognized their critical role in shaping the future of climate science by answering pressing research challenges and goals. In agreement with CLIVAR's Science Challenges outlined in the Science Plan, ECS participants emphasized the need for improved understanding of 1) regional climate change and variability, 2) internal variability, 3) ocean carbon and heat uptakes, and 4) climate processes and feedbacks. The community would also benefit from coordinated climate model developments, an improved and expanded global observation network, and further efforts towards seamless prediction across space and time scales. The ECS recognized the need for increased interdisciplinary research and are committed to bridging the gaps between disciplines.

International collaboration was highlighted as instrumental to the success of the global science community, as the ECS recognized that climate challenges are not contained by political borders, and international cooperation is critical for developing solutions. Collaboration is dampered by asymmetries between nations, which include: unequal access to data and journals, unequal funding and resources, language barriers, and political limitations such as overly-restrictive visa requirements which too often hinder travel. Potential solutions include two-way collaborative exchanges of scientists between countries, promoting regional networks and capacity building (particularly within developing nations), and encouraging participation in international networks and organizations to link scientists and increase visibility of their work. An overarching theme which emerged repeatedly at the symposium was the need for increased openness and standardization of scientific content such as access to journal articles, open-source code, and universal accessibility and increased standardization of data. A proposed solution to address travel restrictions due to cumbersome visa requirements is for CLIVAR to take a leading role as a global entity representing climate scientists to formulate an open letter highlighting the issue and addressing it to local science ministries and foreign affairs departments.

Education at all levels, from schools to seniors, was seen as key to engaging the audience of information produced by the climate science community. An active debate emerged on the appropriate spread of CLIVAR efforts between conducting core scientific research versus engaging in communication. It was recognized that effectively informing adaptation measures would require far greater inclusion of "external disciplines," including the social sciences, engineering and planning communities, while still requiring significant input from the CLIVAR science community.

The ECS expressed general support for the priorities and implementation strategies laid out in the CLIVAR Science Plan while making concrete suggestions for improving the plan to better reflect the full community. The next generation of climate scientists is dedicated to overcoming the challenges outlined in this summary and looking forward to advancing CLIVAR's mission and activities by leveraging the new ideas and collaborations forged at the 2016 ECS Symposium.

A further article titled "Summary of the CLIVAR Early Career Scientists Symposium 2016", with an overview of the activities of the ECC Symposium, has been submitted to Nature Climate and Atmospheric Science, and should be published soon.

Indian Ocean sea surface partial pressure CO_2 and air-sea CO_2 flux interannual variability in the CMIP5-ESM models

Rondrotiana Barimalala[1], Annalisa Bracco[2], Lei Zhou[1]

[1]Shanghai Jiao Tong University, Shanghai, China

[2]Georgia Institute of Technology, Atlanta, GA, USA

Contact e-mail: *rbarimal@sjtu.edu.cn*

Introduction

Studies on interannual variability in biogeochemistry are still limited in the tropical Indian Ocean (IO), particularly with regard to the air-sea CO_2 gas exchanges. Existing studies, mostly focused on annual means and seasonal variability, present large uncertainties as observations spread in space and time over IO are still lacking. For instance, using ship observational data, Takahashi et al. (2009) found that the tropical Indian Ocean is a source of CO_2 to the atmosphere with an annual mean of $0.09\pm0.005 PgC.yr^{-1}$. Similarly Valsala et al. (2013) found that the Indian Ocean is a source of $0.12\pm0.04 PgC.yr^{-1}$ to the atmosphere using a simple ocean biogeochemical model. On the other hand, Gurney et al. (2004) found that the Indian Ocean is a sink of CO_2 with an annual mean of $0.32\pm0.33 PgC.yr^{-1}$ using inverse techniques.

Previous studies show that changes in physical climate can affect the exchange of CO_2 between the atmosphere, land and ocean. The resulting changes in CO_2 concentration in turn affect the physical climate, through the so-called climate-carbon feedback (e.g. Friedlingstein et al., 2006, Arora et al., 2013). The well-known interannual variability in the IO might, therefore, affect the air-sea CO_2 variability, that can then feedback to its physical modes. However, most studies on air-sea CO_2 fluxes and their interannual variability are focused on the tropical Pacific and Atlantic as the Indian Ocean does not contribute significantly to the global CO_2 flux variability (e.g, Le-Quere et al., 2000; McKinley et al., 2004; Valsala et al., 2014; Wang et al., 2015). Nevertheless, although the IO air-sea CO_2 variability may not contribute on a global scale, it can play an important role regionally.

Among the few existing studies, Valsala et al. (2013) found that the interannual anomalies of CO_2 emission over the northern Indian Ocean are about 30% to 40% of the seasonal amplitudes. However, due to the biases and magnitude errors in their analyses, which may be due to lack of an ecosystem module in their model, they suggest that further studies are needed. Recently, the fifth Coupled Model Intercomparison Project (CMIP5 - Taylor et al., 2012) provides a large enough ensemble of Earth System Models (ESM) designed to simulate the interaction between physical, chemical and biological processes in the atmosphere, land and ocean to allow for reconsidering this problem.

The aim of this study is therefore to evaluate how the CMIP5-ESM models represent the interannual variability of surface pCO_2 partial pressure and air-sea CO_2 flux over the Indian Ocean. Moreover, we seek to investigate the linkages between pCO_2 variability and the well-known physical modes that impact the Indian Ocean circulation: the El-Niño Southern Oscillation (ENSO) and the Indian Ocean Dipole (IOD). Four models from the CMIP5-ESM are analyzed in this work. Overall, the models depict a realistic seasonal cycle in surface pressure CO_2 ($spco_2$) and air-sea CO_2 fluxes ($fgco_2$). The whole IO (north of 30^oS) is found to be a net sink in CO_2 both in the observations (with an annual mean of $0.06 PgC.yr^{-1}$) and in the models (with an annual mean ranging from $0.003 PgC.yr^{-1}$ to $0.05 PgC.yr^{-1}$). In the models, the interannual variability in $fgco_2$ varies from 25% to 95% of the respective seasonal amplitude. However, further investigation is needed to explain the driving mechanisms of the air-sea CO_2 flux interannual variability as no precise conclusion could be deduced from the present study.

Models and data description

Outputs from four models participating in the CMIP5-ESM ensemble are analyzed in this study. These models are used based on the availability of the data when the analysis was initiated. However a more complete set of the models will be published in a later report.

The models are CESM1-BGC, GFDL-ESM2G, HadGEM2-ES and MPI-ESM-LR. One realization from each model is used. Monthly mean from the outputs are utilized through the study. We focus on the historical simulations

and on the period extending from 1950 to 2005.

We also use the HadISST reanalysis (Rayner et al., 2003) as observational counterpart of sea surface temperature (SST), and the climatological data from Takahashi et al. (2009) to evaluate the $spco_2$ and $fgco_2$ fluxes. The anomalies of any given variable throughout this study are calculated as the difference between the variable and the time dependent mean for the period of study.

Nino3.4 index defined as the area average of SST anomalies within 190E-210E, 5S-5N is used to represent ENSO, and the IOD index is defined as the difference between the area average SST anomalies within east IO (EIO; 90E - 110E, 10S - 0) and west IO (WIO; 50E-70E, 10S - 10N).

Climatology

Fig 1 shows the climatological SST, $spco^2$ and $fgco_2$ (downward positive) averaged over the whole IO domain (30E-110E, 35S-30N). In general, the models represent well the seasonal cycle of these three variables.

For SST, the highest mean temperature occurs during boreal spring, in correspondence with the monsoon reversal period. The lowest temperature is seen in late boreal summer when different upwelling systems over the basin (e.g., Somalia upwelling system, east IO) are at their peak.

Compared to the observations, CESM1-BGC shows a warm bias throughout the year, whereas the other three models are colder than HadISST, with HadGEM2-ES being the closest to the observations, except for April.

Similarly, the $spco_2$ annual cycle has its maximum in boreal spring and minimum in August, confirming the partial role of SST in driving the $spco_2$. The annual variation in $spco^2$ throughout the year is around 2Pa. HadGEM2-ES shows the strongest bias with respect to the climatological observations of Takahashi et al. (2009), while the other three models are close to each other and displaying weaker levels than the observations, especially from June onward.

On the other hand, the air-sea CO_2 flux reaches a maximum during boreal summer season and a minimum in winter. In this study, positive $fgco_2$ represents flux from the atmosphere into the ocean. In the observational reanalysis the whole IO is therefore a net sink of CO_2(0.06PgC.yr^{-1}) in all months. The models, however, display negative $fgco_2$ (source to the atmosphere) in winter extending into spring and early boreal summer depending on the model. On average, the annual mean in $fgco_2$ is found to be 0.047PgC.yr^{-1} in CESM1-BGC, 0.05PgC.yr^{-1} in GFDL-ESM2G, 0.01PgC.yr^{-1} in HadGEM2-ES and 0.003PgC.yr^{-1} in MPI-ESM-LR. By separating the north and south IO, the models agree with previous studies,

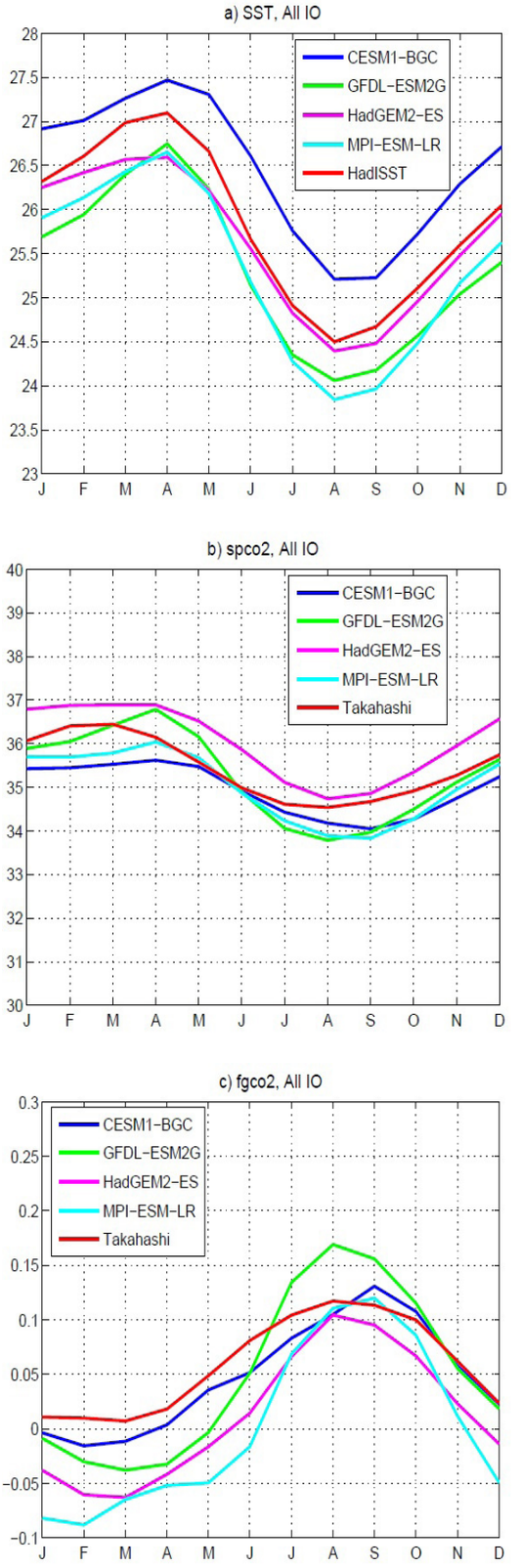

Figure 1: Seasonal cycle averaged over the India Ocean (30E-110E, 35S-30N) for **(a)** SST (Units: degree C), **(b)** ocean surface pco_2 (Units: Pa) and **(c)** air-sea CO_2 flux in which positive sign represents a downward flux (Units: PgC.yr^{-1})

suggesting that the north IO is a perennial source of CO_2 to the atmosphere, whereas the south is a sink (e.g. Sarma et al., 2013). The magnitudes of CO_2 fluxes are mostly underestimated in the models, except during boreal summer when GFDL-ESM2G depicts higher fgco^2 than in the observational data set.

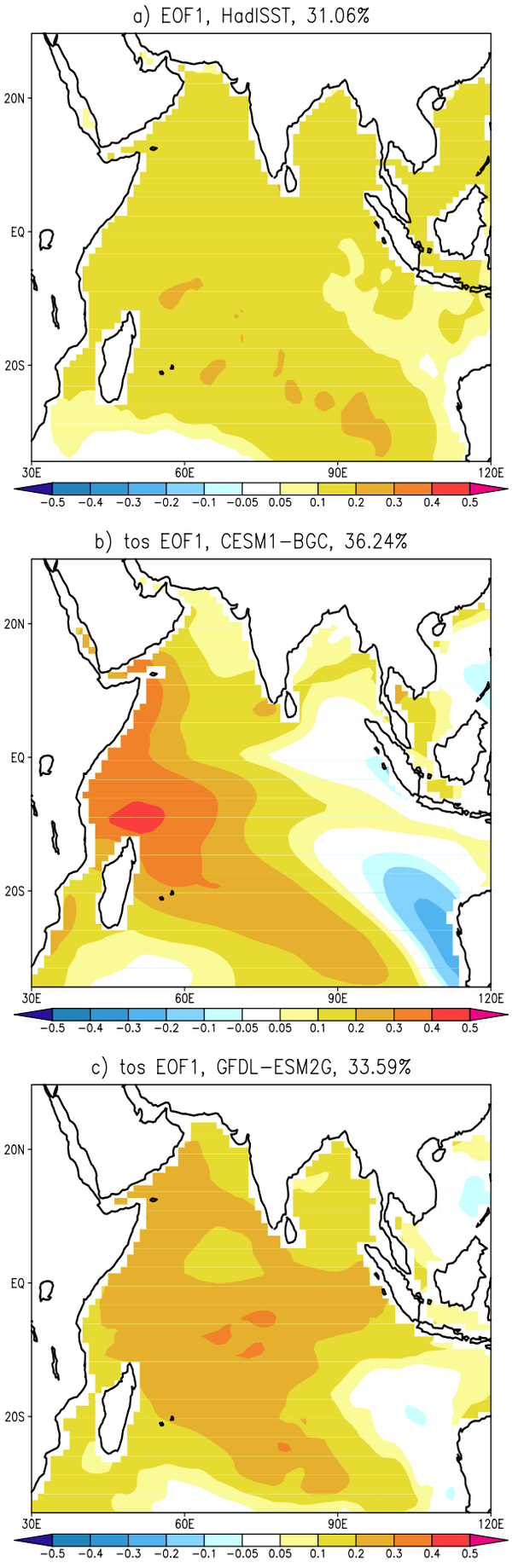

Figure 2: SST first EOF for **(a)** HadISST, **(b)** CESM1-BGC, **(c)** GFDL-ESM2G, **(d)** HadGEM2-ES, **(e)** MPI-ESM-LR. (Units: degree C)

Long-term trend and interannual variability

Before analyzing the interannual variability in $spco_2$ and $fgco_2$, the model representation of the dominant climate modes in SST is evaluated with an Empirical Orthogonal Function (EOF) analysis. This is important given that the surface ocean temperatures are a major driver of the$spco_2$ (and therefore $fgco_2$) seasonal cycle and they are likely to influence the interannual variability as well. All interannual analyses are computed after removing the linear trend in the data and using a 12 months running mean of the monthly data from 1950-2005.

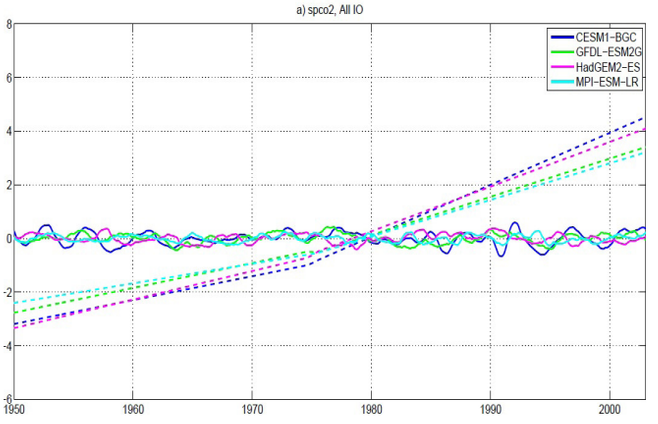

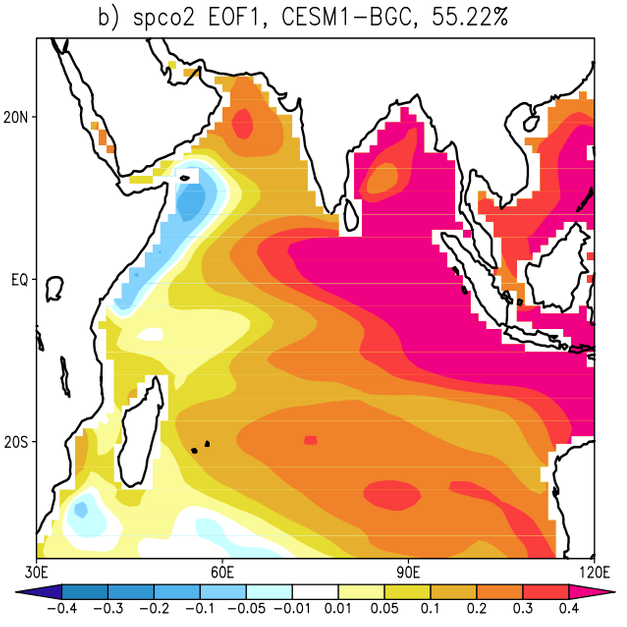

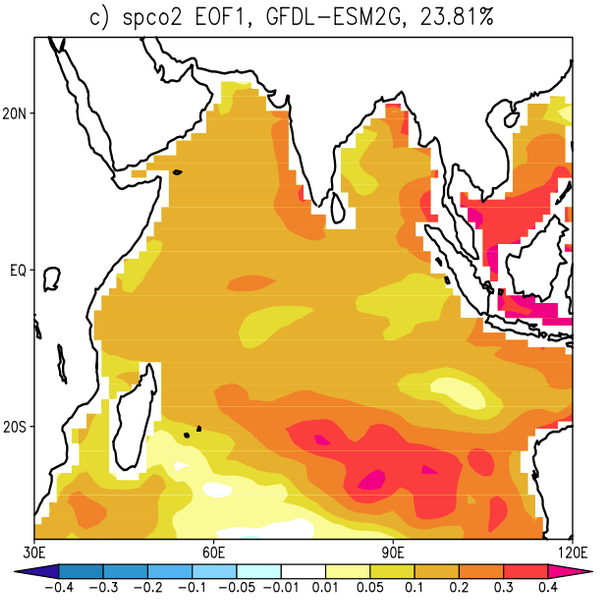

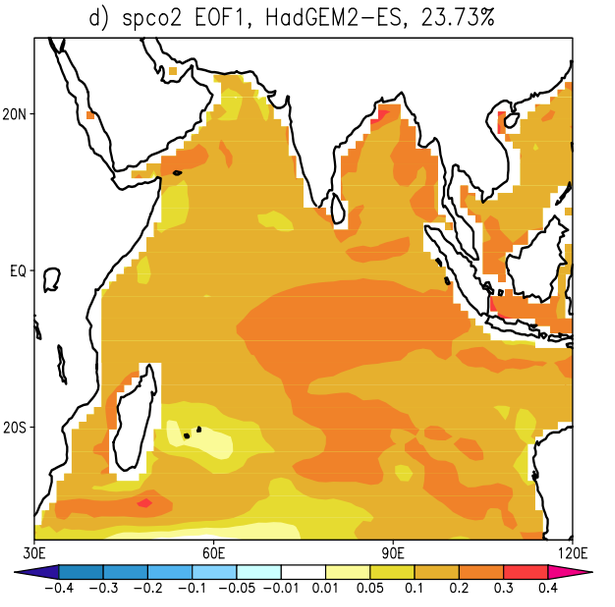

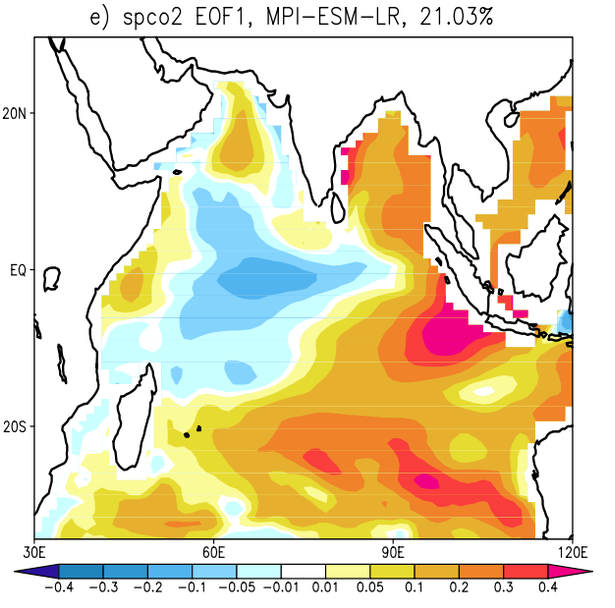

Figure 3: (a) $spco_2$ interannual variability (continuous line) and linear trend (dashed line). $spco_2$ first EOFs for CESM1-BGC **(b)** CESM1-BGC, **(c)** GFDL-ESM2G, **(d)** HadGEM2-ES, **(e)** MPI-ESM-LR(Units: Pa)

Fig 2 shows the first EOF (EOF1) of the SST anomalies in the HadISST reanalysis and in the models. The observational data set displays a basin-wide warming, in which the first Principal Component (PC1) is significantly correlated to the Nino3.4 time series (corr = 0.57) and explains 31% of the total variance, whereas PC2 (not shown) is significantly linked to the IOD index (corr 0.32) In general, the models reproduce the observed dominant modes. For instance, CESM1-BGC, GFDL-ESM2G and MPI-ESM-LR depict the basin wide warming as EOF1, explaining respectively 36%, 33.6% and 29.9% of their total variances. The correlations between PC1 and Nino3.4 in these three models are higher than in the observations (0.62, 0.63 and 0.65, respectively).

In HadGEM2-ES the EOF1 pattern mostly consists of a positive anomaly but a cooling signal can be seen in the eastern part of the basin, forming a dipole-like pattern. The correlation between PC1 and Nino3.4 is also lower (0.63) than that of PC1-IOD (0.68), suggesting that the dominant mode of variability in this model is the IOD.

The temporal evolution of the IO $spco_2$ anomalies in the CMIP5-ESM models are shown in Fig 3a. Continuous lines show the linearly detrended anomalies, and dashed lines represent the linear trends for each model. Overall the models show positive trends up to 1.8Pa.decade^{-1}. By considering the whole period of 1950-2005, a change in linear trend is noticed in the models. Change in trend detection technique is therefore applied and the models depict an acceleration of trend from after 1975 compared to previous years. These two linear trends are then removed from the models accordingly. However, no observational data can be used to verify such change in the trend.

The interannual anomalies in $spco_2$ have relatively weak magnitude with respect to the trend, and are contained within ±0.3Pa. The patterns of the first EOFs in $spco_2$ (Figs 3b-e) show quite a disagreement between the models. For instance, CESM-BGC displays a dipole-like pattern with an increase in $spco_2$ in the east IO and a decrease in the west. EOF1 explains 55% of the total variance. The correlation between PC1 with Nino3.4 and IOD are respectively 0.4 and 0.63. The relatively high correlation between PC1 and IOD suggests that the dominant mode of variability in $spco_2$ for CESM1-BGC is the IOD. For GFDL-ESM2G and HadGEM2-ES, the EOF1 is characterized by a basin-wide increase in $spco_2$, which explains about 23% of the variance. The correlations between PC1 and Nino3.4 are respectively 0.43 and 0.56 in the two models. The correlation between PC1 and IOD, however, is not statistically significant for GFDL-ESM2G and is 0.36 for HadGEM2-ES. Thus, for these two models, ENSO modulates the $spco_2$ interannual variability. Finally in MPI-ESM-LR, although EOF1 represents 21% of the total variance, the dominant mode does not show any significant correlation with either of the two physical modes.

Fig 4a shows the area integrated interannual anomalies of $fgco_2$ in the IO. For the period of 1950-2005, all models show a weak upward $fgco_2$ trend in which CESM1-BGC displays the highest trend of 0.008PgC. decade^{-1} and GFDL-ESM2G shows the lowest at 0.002PgC. decade^{-1}.The amplitudes of the interannual anomalies range between -0.025PgC.yr^{-1} and 0.03PgC.yr^{-1}, about 25% to 95% of their respective seasonal amplitudes.

The first EOFs of $fgco_2$ in the IO explain respectively 41.9%, 20.6%, 17.1% and 21.2% of the variance for CESM1-BGC, GFDL-ESM2G, HadGEM2-ES and MPI-ESM-LR. In the four models, common patterns of positive air-sea CO_2 flux are seen over the south IO (mainly along the thermocline ridge) and the Bay of Bengal. These are known areas of net sink CO_2 in the IO. In other parts of the basin, the models show a significant mismatch. For instance, the eastern equatorial IO is a CO_2 sink in CESM1-BGC and HadGEM2-ES, but it is a source in the other two models. Moreover, in the western IO, CESM1-BGC and GFDL-ESM2G depict negative $fgco_2$ whereas HadGEM-ES and MPI-ESM-LR show positive anomalies.

Overall, the EOF pattern for CESM1-BGC clearly reflects the influence of the IOD on the air sea CO_2 flux; the correlation between PC1 and IOD is 0.62. For GFDL-ESM2G, and HadGEM-ES, although the dominant mode in $spco_2$ is linked to ENSO, the correlation between $fgco_2$ PC1 and Nino3.4 (0.27 for GFDL-ESM2G and 0.48 for HadGEM-ES) does not differ much from that of PC1 and IOD (0.28 and 0.51). Similar correlations are also found in MPI-ESM-LR, despite the fact that the correlation between the two physical modes with $spco_2$ was not statistically significant.

No clear conclusion on the relative role of IOD and ENSO can be deduced yet from these last three models. These results need further investigation given that the effect of ENSO and IOD in these models could be complementary throughout the fifty year-period of study (as found by Valsala et al. (2013) in their work on the Northern IO), triggering very close correlations between PC1 and each of the indices.

Summary

Outputs from 4 models within CMIP5-ESM are used to investigate the interannual variability in $spco_2$ and air-sea CO_2 flux in the tropical Indian Ocean. The models reproduce reasonably well the seasonal cycle over the whole IO. However, the interannual variability along with the dominant driving mechanisms differs considerably between the models. The IOD is found to be the main driver of the air-sea CO_2 flux variability in CESM1-BGC, while both the IOD and ENSO appear to play a comparable role in the other models. A closer look at different parts of the IO will also help understanding the CO_2 interannual variability and its mechanisms over the

basin. In addition, to better quantify the contribution of the physical forcings, a decomposition of the $spco_2$ responseto SST, salinity, alkalinity and dissolved inorganic carbon changes should be performed.

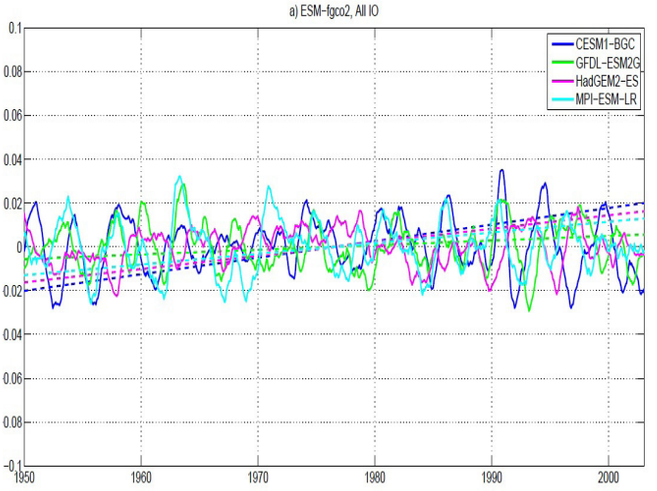

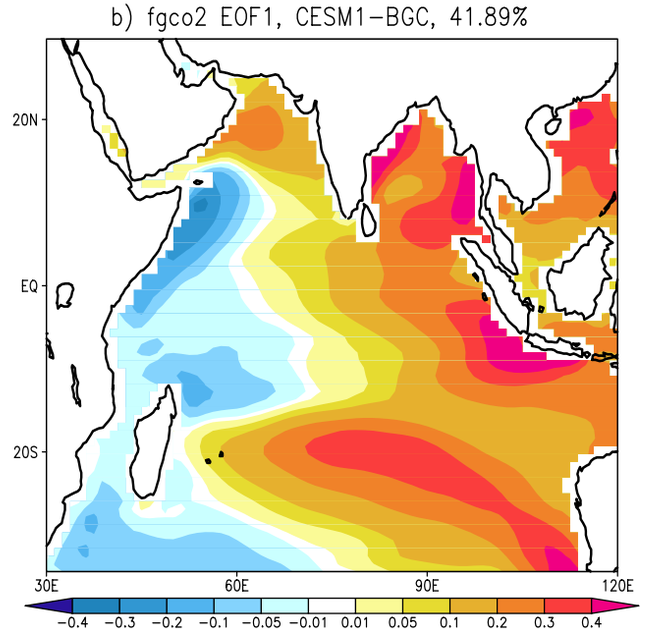

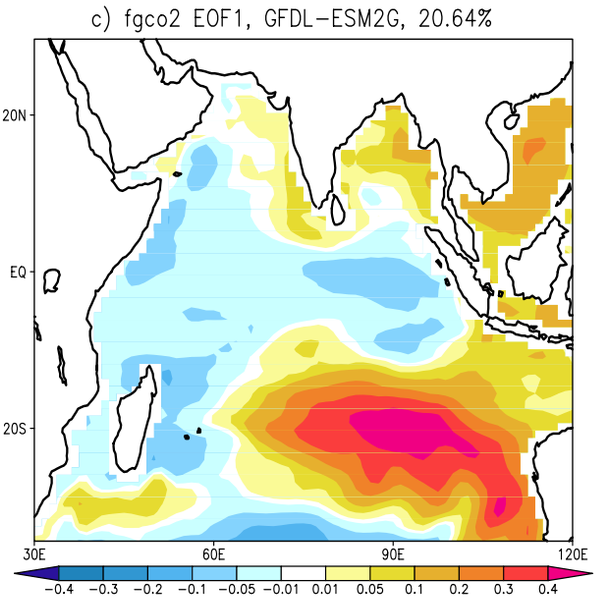

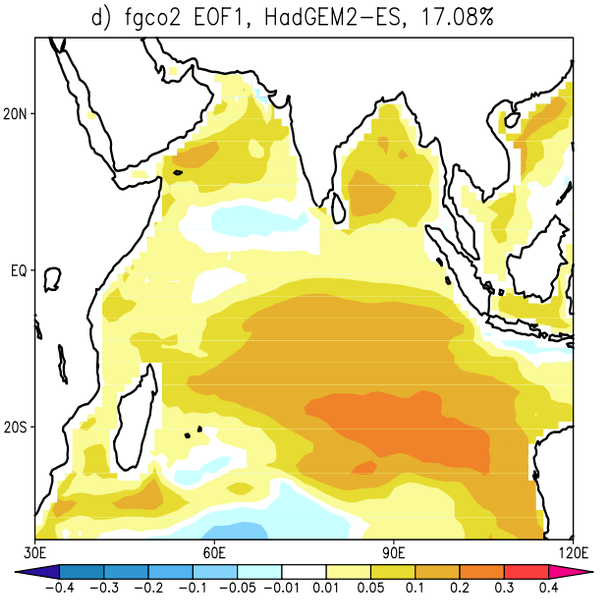

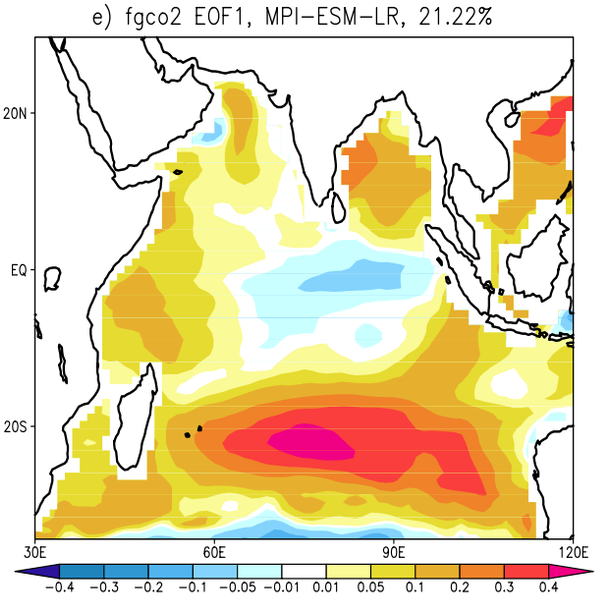

Figure 4: Same as Fig 3 but for $fgco_2$ (Units: 10-1PgC.yr^{-1})

References

Arora, V., G. Boer, P. Friedlingstein, et al. 2013: Carbon-concentration and carbon-climate feedbacks in CMIP5 Earth system models. J. Climate. doi:10.1175/JCLI-D-12-00494.1

Friedlingstein P., P. Cox, R. Betts et al. 2006: Climate-carbon cycle feedback analysis: results from the (CMIP)-M-4 model intercomparison. J. Climate, 19, 3337–3353.

Gurney K.R., R.M. Law, A.S. Denning, P.J. Rayner, B. Pak 2004: Transom-3-L2-modelers Transcom-3 inversion intercomparison: model mean results for the estimation of seasonal carbon sources and sinks. Glob Biogeochem Cycles 18. doi:10.1029/2003GB002111

Le-Quere C., J.C. Orr, P. Monfray, O. Aumont, G. Madec 2000: Interannual variability of the oceanic sink of CO2 from 1979 through 1997. Glob Biogeochem Cycles 14:1247–1265

McKinley G.A., M.J. Follows, J. Marshall 2004: Mechanism of air-sea CO2 flux variability in the equatorial Pacific and North Atlantic. Glob Biogeochem Cycles 18. Doi:10.1029/2003GB002179

Rayner N.A., D.E.Parker, E.B. Horton et al. 2003: Global analysis of SST, sea ice and night marine air temperature since the late nineteenth century. J Geophys Res. Doi:10.1029/2002JD002670.

Sarma V. V. S. S., A. Lenton , R.M. Law et al. 2013: Sea-air CO2 fluxes in the Indian Ocean between 1990 and 2009. Biogeosciences, 10, 7035-7052. doi:10.5194/bg-10-7035-2013.

Takahashi T., S.C. Sutherland, R. Wanninkhof, C. Sweeney, R.A. Feely 2009: Climatological mean and decadal changes in surface ocean pCO2, and net sea–air CO2 flux over the global oceans. Deep-Sea Res Part 2, 56,554–577.

Taylor K.E., R.J. Stouffer, G.A. Meehl 2012: An overview of CMIP5 and the experiment design. Bulletin of the American Meteorological Society, 93, 4: 485-498.

Valsala V.,S. Maksyutov 2013: Interannual variability of the air-sea CO2 flux in north Indian Ocean. Ocean Dynamics 63, 165. Doi:10.1007/s10236-012-0588-7

Valsala V., M.K. Roxy, K. Ashok, R. Murtugudde 2014: Spatiotemporal characteristics of seasonal to multidecadal variability of pCO2 and air-sea CO2 fluxes in the equatorial Pacific Ocean. Journal of Geophysical Research: Oceans, 119, 12, 8987-9012. doi: 10.1002/2014JC010212

Wang X., R. Murtugudde, E. Hackert, J. Wang, J. Beauchamp 2015: Seasonal to decadal variations of sea surface pco2 and sea-air CO2 flux in the equatorial oceans over 1984-2013: A basin-scale comparison of the Pacific and Atlantic Oceans. Glob Biogeochem Cycles 29. Doi:10.1002/2014GB005031.

On the vorticity dynamics of the downwelling branch of the AMOC

Nils Brüggemann[1], Caroline A. Katsman[1], Henk A. Dijkstra[2]

[1]Delft University of Technology, Netherlands

[2]Institute for Marine and Atmospheric Research Utrecht, Netherlands

Contact e-mail: *n.bruggemann@tudelft.nl*

Introduction

The zonally averaged transport in the Atlantic, the Atlantic Meridional Overturning Circulation (AMOC), is responsible for a maximum northward heat transport of about 1PW (Trenberth and Caron, 2001). It is therefore a key player in the climate system and subject of many climate research studies. Despite the enormous research effort, open questions regarding e.g. the strength and sensitivity of the AMOC remain. Especially, it is unclear how the AMOC changes in the course of projected climate change. This article is intended to give a brief introduction about our approach to better understand where and how the northward flowing water masses sink before they return southward at depth. In particular, we aim to investigate which dynamical processes are involved in this sinking process that we refer to as the downwelling branch of the AMOC.

Idealized studies indicate that the downwelling is confined to lateral boundary currents around the marginal seas of the North Atlantic (e.g. Spall, 2001; Straneo, 2006; Spall, 2010). These studies further indicate that eddies play an important role for the downwelling since they influence e.g. the heat and vorticity budget of the boundary current. This than effects the horizontal convergence of the flow and therefore the downwelling itself.

In the presence of rotation, vertical motion is linked to a change of vorticity. Spall (2010) and Cenedese (2012), use the vorticity budget to identify how the downwelling causing a vorticity stretching is balanced by other terms in the vorticity balance. They find that vorticity advection and dissipation plays an important role in balancing the stretching.

We follow the approach of Spall (2010) and Cenedese (2012) and diagnose the vorticity budget but further expand it by separating the mean advection term from the eddy advection term. This enables us to distinguish between the role of the mean flow and that of the eddies on the downwelling. Beside using idealized studies similar to that of Spall (2010), we also diagnose the vorticity budget in a more realistic strongly-eddying (0.1 degree) global ocean model.

The downwelling in a realistic configuration

The realistic model that we use to diagnose the downwelling and the vorticity budget is a strongly-eddying configuration of POP (Parallel Ocean Program) with a nominal grid spacing of 0.1°and 42 vertical levels (Maltrud et al., 2010). The model is forced by the "normal year" Coordinated Ocean Reference Experiment (CORE) forcing dataset. This dataset, consists of a single annual cycle that is repeated every model year (Large and Yeager, 2004). Details of the model configuration can be found in the auxiliary material of Weijer et al. (2012).

Fig 1a shows the sea surface temperature in the Labrador Sea in winter. It shows a warm boundary current circulating anti-clockwise around the colder interior of the Labrador Sea. At the west coast of Greenland a topographic narrowing destabilizes the boundary current and warm-core anti-cyclonic eddies form. These eddies play an important role in exchanging heat and vorticity between the boundary current and the interior.

All along the boundary current, patterns of enhanced vertical velocities can be found (Fig. 1b) often with alternating signs. Since Fig. 1b was derived from a 10 year mean, the alternating up- and downwelling signal cannot be associated with mesoscale eddies.

An exception to this alternating up- and downwelling signal can be found downstream of Cape Desolation in the West Greenland Current. Here, a large stripe of downward velocities can be identified, accompanied by a weaker upwelling signal further offshore. This strong downwelling signal is responsible for most of the net downwelling in the Labrador Sea and therefore of particular interest for this study.

The downwelling in an idealized configuration

To further investigate the dynamics that are involved in the downwelling, we use an idealized model configuration. The main aim of this idealized model simulation is to reproduce the basic circulation of the Labrador Sea, in particular the enhanced downwelling pattern offshore of Cape Desolation. At the same time, we try to avoid

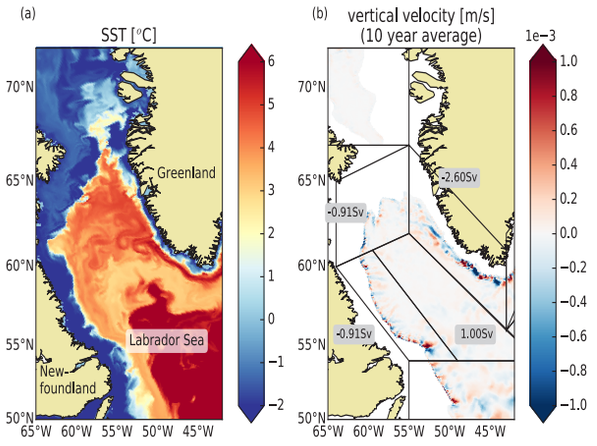

Figure 1: Circulation of the realistic strongly eddying ocean simulation. **(a)** Wintertime sea surface temperature (SST) snapshot of model year 302 and **(b)** vertical velocity at 1000m averaged over 10 years (year 296 to 306) Labelled values in (b) denote vertical transports over marked regions.

generating complicated patterns of up- and downwelling as found in the realistic model (Fig. 1b) by using a simplified topography.

Our idealized model configuration of the MITgcm is similar to that one used by Spall (2010). The model domain consists of a closed basin with a simple topography that decays exponentially from the lateral boundaries towards the interior (see Fig. 2). By increasing the e-folding scale of the topographic slope, we introduce a topographic narrowing at the eastern part of our domain. This topographic narrowing is mimicking the steep slopes offshore of Cape Desolation.

We use a horizontal resolution of 2km and 20 vertical levels of 150m, yielding a maximum depth of 3000m. By using partial bottom cells, we obtain a smoother representation of the topographic slope. Further idealizations of our model consist of applying the beta-plane approximation and using a linear equation of state with temperature as the only active tracer. Biharmonic dissipation and diffusion operators are applied with no-slip boundary conditions at the lateral and bottom boundaries.

A warm boundary current, representing current systems like the West Greenland Current, is induced by restoring temperature in the southernmost part of the domain to a reference profile with constant vertical and meridional gradients. Furthermore, we restore velocity in this region to be in thermal wind balance and add a barotropic component such that there is a zero flow at the bottom. We represent surface cooling by applying a constant heat flux of 50 W/m^2. In cases of static instability, we increase the vertical diffusivity as a parameterization of convection since our simulations are hydrostatic.

After a spin-up of five years, the flow field is in statistical equilibrium. A warm boundary current is established (Fig. 2a) and a rich warm-core anti-cyclonic eddy field is responsible for exchanging heat between the warm boundary current and the cold interior balancing the surface heat loss (Fig. 2a and b). The mean flow derived from a five-year average following a five year spin-up demonstrates enhanced vertical velocities along the topographic narrowing, with a downward transport of 4.4Sv (Fig. 2c).

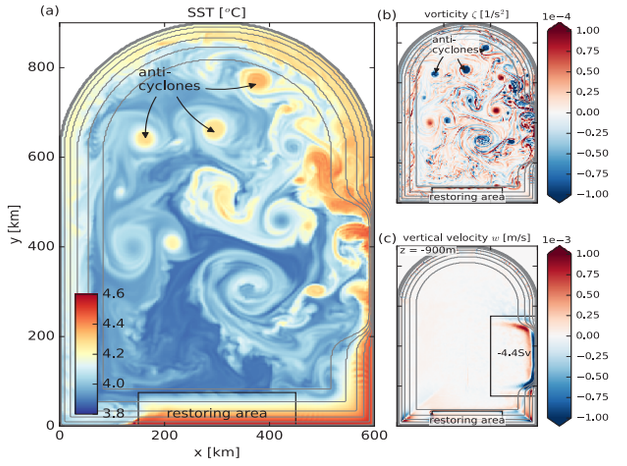

Figure 2: Snapshot of **(a)** sea surface temperature and **(b)** surface vertical vorticity component after 9.5 years; **(c)** five year average (year 6 to 10) of vertical velocity at 900m. Grey lines denote topography contours with intervals of 500m. Averaging the vertical velocity over the region indicated by the black square yields a net downwelling of 4.4Sv.

The vorticity budget

Spall (2010) used the vorticity budget in a similar setup as our idealized configuration to find that stretching of planetary vorticity is primarily balanced by eddy flux divergences of relative vorticity and, close to the lateral boundary, by friction. We expand the diagnostics of Spall (2010) by separating the vorticity advection term into a mean and an eddy component. This facilitates the explanation of both terms but most importantly, it allows to separate the role of the eddies from that of the mean flow.

In fact, we find that both terms are of similar magnitude but play a different role in setting the downwelling. The mean flow is most dominant up- and downstream of the narrowing where the topographic slope changes and the current converges. It has a strong downward component upstream and slightly weaker upward component downstream of the narrowing. It therefore indicates how a topographic sill can induce strong down- and upward motion. We speculate that similar topographic features are responsible for the complicated up- and downwelling patterns in the realistic model (Fig. 1b).

The eddy term is most dominant at the narrow slope

itself. As found by Spall (2010), the eddy component of the vorticity advection is towards the boundary. Therefore, it induces vorticity stretching offshore and vorticity squeezing onshore. Indeed, the offshore stretching can be identified with the strong downwelling pattern along the topographic narrowing (Fig. 2c). However, there is no upwelling signal onshore. Here, dissipation and the mean component of the vorticity advection cancel the eddy component of the vorticity advection.

Conclusion

The aim of this study is to better understand the dynamics of enhanced downwelling and therewith to better understand the downwelling branch of the AMOC. Measuring vertical velocities remains a challenge and observations of vertical velocities barely exist. Therefore, we use a combination of realistic and idealized models to study the downwelling. With the idealized simulations, we are able to focus on the most crucial dynamical processes contributing to the downwelling. By excluding e.g. complex topographic features, the downwelling pattern becomes more regular and easier to interpret. Diagnosing the dynamics that are involved in the downwelling of the idealized model then facilitates to interpret the more complex downwelling patterns in the realistic model simulation.

Finally, we think that our results are helpful for understanding and interpreting the sensitivity of the dynamics involved in the downwelling branch of the AMOC. In particular, we expect to gain more insight into the sensitivity of the downwelling or the eddy activity with respect to external parameters like the wind stress or surface heat fluxes over marginal seas like the Labrador Sea.

Acknowledgments

We would like to thank Michael Kliphuis in supporting us with the POP simulations. The simulations have been performed on the Cartesius supercomputer at SURFsara (https://www.surfsara.nl) through the projects SH-350-15 and SH-284. Funding for Nils Brüggemann is provided by the Netherlands Organisation for Scientific Research (NWO-ALW VIDI grant 864.13.011 awarded to Caroline Katsman).

References

Cenedese, C., 2012: Downwelling in Basins Subject to Buoyancy Loss. J. Phys. Oceanogr., 42, 1817-1833

Large W. G. & Yeager, S., 2004: Diurnal to decadal global forcing for ocean and sea-ice models: The data sets and flux climatologies. NCAR Technical Note NCAR/TN-460+STR

Spall, M. A., 2010: Dynamics of Downwelling in an Eddy-Resolving Convective Basin. J. Phys. Oceanogr., 40, 2341-2347

Straneo, F., 2006: On the Connection between Dense Water Formation, Overturning, and Poleward Heat Transport in a Convective Basin. J. Phys. Oceanogr., 36, 1822-1840

Trenberth, K. E. & Caron, J. M., 2001: Estimates of Meridional Atmosphere and Ocean Heat Transports. J. Climate, 14, 3433-3443

Weijer, W.; Maltrud, M. E.; Hecht, M. W.; Dijkstra, H. A. & Kliphuis, M. A., 2012: Response of the Atlantic Ocean circulation to Greenland Ice Sheet melting in a strongly-eddying ocean model. Geophys. Res. Lett., 39

Observed and Simulated Summer Rainfall Variability in Southeastern South America

Leandro B. Díaz, Carolina S. Vera, Ramiro I. Saurral

Centro de Investigaciones del Mar y la Atmósfera/CONICET-UBA DCAO/FCEN, UMI-IFAECI/CNRS, Buenos Aires, Argentina

Contact e-mail: *ldiaz@cima.fcen.uba.ar*

Introduction

The climate changes observed in the last decades have raised concern among policy and decision makers about the importance of improving the knowledge and prediction of climate. In particular, the Southeastern South America (SESA) is one of the few regions in the world which have experimented both large positive summer precipitation trends in mean and extremes during the 20th century (e.g. Liebmann et al., 2004; Re and Barros, 2009; Penalba and Robledo, 2010; Saurral et al., 2016). Furthermore, a precipitation increase is projected over the region for the current century (Hartmann et al., 2013). These changes pose a significant threat for many socio-economic sectors within this region.

Recently, Vera and Díaz (2015) have shown that the fifth phase of the Coupled Model Intercomparison Project of the World Climate Research Program (CMIP5, Taylor et al., 2012) multi-model historical simulation dataset (i.e. including all observed forcings) is able to represent the sign of the trends of the last century over SESA, although with a weaker magnitude. When comparing results from the historical simulation including all forcings against those only including natural forcings and only considering greenhouse gases forcing, they concluded that anthropogenic forcing in CMIP5 models has a detectable influence in explaining the observed positive precipitation trends.

Through teleconnection patterns, tropical ocean variability is one of the main precipitation forcings in SESA. The El Niño Southern Oscillation (ENSO) has been shown to be the main influence for SESA rainfall variability on interannual scales (e.g. Ropelewski and Halpert, 1987; Kiladis and Diaz, 1989). However, the way in which ENSO affects SESA rainfall seems to be modulated by ocean lower-frequency patterns as the Pacific Decadal Oscillation (PDO) (Kayano and Andreoli, 2007) and the Atlantic Multidecadal Oscillation (AMO) (Kayano and Capistrano, 2014). Furthermore, Barreiro et al. (2014) found that both, PDO and AMO, have also an influence on summer SESA rainfall independently from ENSO.

How anthropogenic forcings are combined with low frequency natural climate variability to modulate the regional rainfall variability and trends in SESA has not been explored in detail yet. Therefore, a deeper knowledge of decadal climate variability in the region is needed in order to project near term future changes with a larger degree of confidence. According to this, our goal is to understand the influence of the large-scale interannual variability of sea surface temperatures (SST) on austral summer rainfall in SESA in a global warming context and to evaluate if CMIP5 models are able to represent that influence properly.

Leading observed co-variability pattern of SST and SESA rainfall

Rainfall data from the Global Precipitation Climatology Centre (GPCC) dataset (Schneider et al., 2011) were used in this study, with a spatial resolution of 2.5°. This product considers station-based records, and thus it only has continental coverage. SST monthly values were derived from the NOAA Extended Reconstructed Sea Surface Temperature Version 3b (ERSSTv3b, Smith et al., 2008) with a spatial resolution of 2°. Summer was defined as the December–January–February (DJF) trimester. Anomalies were computed from the corresponding long-term means considering the period 1902–2010. Both undetrended and detrended anomalies were defined for both variables. Non-linear trends were removed through a linear regression between global mean SST time series and those for SST or precipitation anomalies at each grid point. Removing linear trends instead of non-linear produce slightly different results in variability patterns obtained, especially for higher order modes. As global warming trend is non-linear, the removal of non-linear trends allows to better identified variability beyond the global warming signal.

The influence of the observed large-scale interannual variability of the SST anomalies on austral summer rainfall in SESA is described through a singular value decomposition analysis (SVD) performed jointly on the summer seasonal rainfall anomalies over SESA

(39°S-16°S;64°W-31°W) and SST anomalies from 45°N to 45°S. The temporal variability of each mode is described by the time series of the expansion coefficients (hereinafter SVD time series) resulted for each variable from the SVD analysis. Correlation maps between the SVD time series of SST and SST anomalies at each grid point (i.e. homogeneous correlation map) were computed to describe the SST patterns associated with the modes. On the other hand, the correlation maps between the SVD time series of SST and precipitation anomalies at each grid point (i.e. heterogeneous correlation map) were used to describe the mode influence on precipitation in southern South America.

The temporal series of the first mode (SVD1), which accounts for 71% of the total squared covariance, exhibits significant variability on interannual timescales, modulated by long-term trends (Fig 1a). The mode is positively correlated with SST anomalies almost everywhere with maximum values in the tropical portions of the Pacific and Indian Oceans (Fig 1b). It also exhibits positive correlations with rainfall anomalies in northern Argentina, Uruguay and Southern Brazil (Fig 1c).

The SVD analysis was also performed considering the detrended anomalies of both variables. The corresponding SVD1 accounts for 51% of the total squared covariance and it presents a strong decadal modulation of its year-to-year activity with phase shifts at around the 1930s, 1970s and 1990s (Fig 1d). This mode shows positive correlations with rainfall anomalies in SESA (Fig 1f) and SST anomalies in equatorial Pacific and Indian Oceans (Fig 1e). Moreover, the mode presents negative correlations with SST anomalies in the North and South Pacific distributed in a 'horseshoe-like' spatial pattern resembling that associated with ENSO or the PDO. A similar SST and precipitation correlation pattern was identified by Grimm (2011) for the second variability mode of summer precipitation for the period 1961-2000, considering almost all South America. Furthermore, the characteristics of the SVD1 obtained here are also similar to the ones obtained by Robledo et al. (2013), computing a SVD analysis between global SST anomalies and daily precipitation extreme index in SESA.

The SVD time series resulting from the analysis of both undetrended and detrended anomalies (Fig 1a and Fig 1d, respectively) shows periods in which the expansion coefficients of the two variables are in phase, while in others they are not. The correlation between those two series can be considered a measure of the strength of the coupling between SST and precipitation patterns obtained from SVD1 (e.g. Venegas et al., 1997). Then, in order to explore changes in the coupling between global SST and SESA rainfall, a 19-year sliding correlation analysis was performed to the SVD time series resulting from the undetrended and detrended anomalies of both variables. Fig 2 shows that sliding correlations are positive for all the period considered, although decadal variations are noticeable. Periods of high coupling (1930s-1940s, 1990s) and low coupling (1980s) can be identified. The results agree with those obtained by Martín-Gómez et al. (2016) using a complex network methodology to detect synchronization periods among the tropical oceans and the precipitation over SESA. In general, sliding correlations are higher for the detrended case (Fig 2), indicating that trends for both variables show different behaviour in some periods, which reduce the corresponding correlation. Preliminary exploratory analysis (not shown) for the detrended case suggest that during positive (negative) events of SDV1, defined as those years in which the SVD1 time series for SST is above 1 (below -1), negative (positive) Southern Annular Mode (SAM) phases seem to reinforce the teleconnections, induced by the tropical Pacific-Indian ocean conditions, in the vicinity of South America. The SAM influence on the Pacific teleconnection has been proposed earlier by Vera et al. (2004) and Fogt and Bromwich (2006).

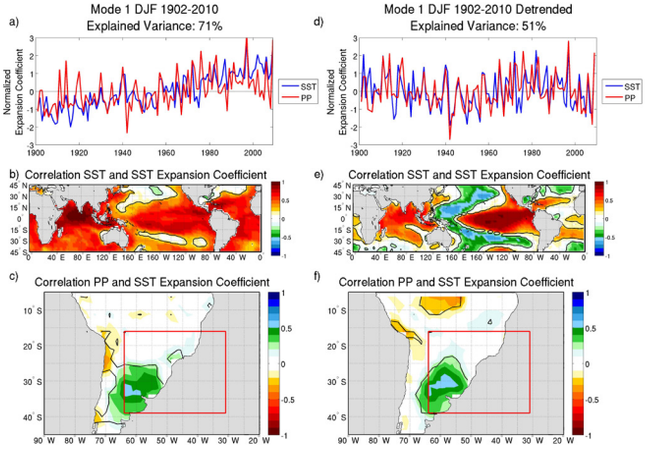

Figure 1: (a) SVD time series of SST (blue) and rainfall anomalies (red) over SESA (region indicated by the red rectangle in c). **(b)** Homogeneous correlation map between the SVD time series of SST and SST grid point anomalies. **(c)** Heterogeneous correlation map between the SVD time series of SST and rainfall grid point anomalies. **(d)**, **(e)** and **(f)** same as (a), (b) and (c), but for the detrended anomalies. Contours indicate 95% significance level.

Leading simulated co-variability pattern of SST and SESA rainfall

A preliminary evaluation of coupled general circulation models' ability in representing the main SVD1 features was made. Historical simulations from 39 models included in CMIP5 were considered. The simulated spatial SVD1 patterns obtained from detrended anomalies were computed over the period 1902-2005 (available period for both observations and models), and compared with those resulted from the observed datasets. An index (M) was defined as the spatial correlation between the simulated and observed patterns for SST, times the spatial correlation between the simulated and observed patterns

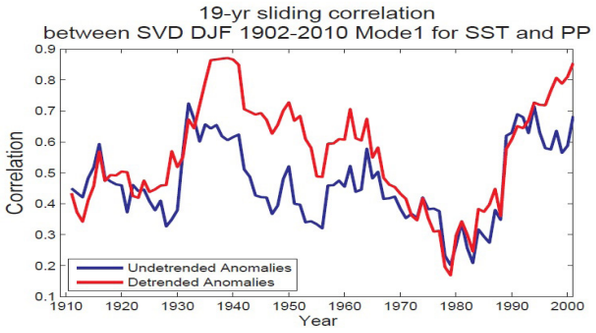

Figure 2: 19-year sliding correlation between SVD time series for SST and rainfall anomalies over SESA for the undetrended (blue) and detrended (red) anomalies.

for rainfall. If M is close to 1, both SST and precipitation patterns are represented properly by the models, while values close to 0 or negatives indicate that models fail in representing properly the observed patterns. To obtain the model ensemble mean, mean of M for each model is computed over all of their members. Inter model dispersion are described by the corresponding standard deviation.

Some CMIP5 models are able to reproduce the spatial patterns corresponding to the leading mode of co-variability, although other are not skillful (Fig 3). The M index value averaged over all models is 0.35, with 25 models from a total of 39, with M values above it. Inter member dispersion is highly variable between models. For some models, like GISS-E2_H, IPSL-CM5A-LR or NorESM1-M, M value could be positive, negative or close to zero depending on the realization selected. In other models, like CCSM4 or HadGEM2-ES, an outlier member mostly affects model performance. On the other hand, there are models that have high M values and low inter member dispersion, as CanESM2, CNRM-CM5, GFDL-CM3 or GISS-E2-R. On average, most models tend to represent properly the SST pattern corresponding to SVD1, with a mean correlation value of 0.69 ranging between 0.32 and 0.9. However, the representation of the rainfall pattern in SESA region is less satisfactory, associated with mean correlation values of 0.45, but extended between -0.75 and 0.82. Several models tend to reproduce a dipole rainfall correlation pattern in southern South America, instead of the observed monopole. These results allows us to conclude that most models in CMIP5 historical simulations are able to reproduce reasonably well the spatial leading pattern of co-variability between SST and SESA rainfall.

Concluding remarks

The co-variability between global SST anomalies and precipitation anomalies in SESA during summer was assessed through a SVD analysis over the period 1902-2010. The temporal series of the SVD1 exhibits significant variability on interannual timescales, modulated by long-term trends. The mode is positively correlated with SST anomalies almost everywhere with maximum values in

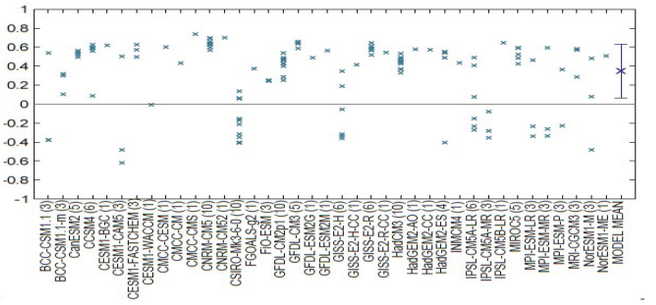

Figure 3: M index (see text for details) for WCRP/CMIP5 models members and model mean. Brackets indicate number of members for each model. Blue bar indicate inter model dispersion for model ensemble mean.

the tropical portions of the Pacific and Indian Oceans, and also exhibits positive correlations with rainfall anomalies in SESA. When detrended anomalies of both variables were considered, the corresponding SVD1 temporal series presents a strong decadal modulation of its year-to-year activity. The corresponding mode shows positive correlations with rainfall anomalies in SESA and SST anomalies in equatorial Pacific and Indian Oceans, and negative correlations with SST anomalies in the North and South Pacific distributed in a 'horseshoe-like' spatial pattern resembling that associated with ENSO or the PDO. Periods of high coupling (1930s-1940s, 1990s) and low coupling (1980s) between undetrended and detrended anomalies of both variables could be identified.

A preliminary analysis of CMIP5 models representation of SVD1 was also performed. Most models in CMIP5 historical simulations are able to reproduce reasonably well the spatial leading pattern of co-variability between SST and SESA rainfall. The reasonable ability that many CMIP5 models exhibits in representing the global SST influence on summer precipitation in SESA, suggests that some model prediction skill might be obtained by simulations that account for a proper initialization of the ocean. Recently, it has been shown that the CMIP5 decadal predictions have some predictive skill in different ocean basins for a few years (e.g. Meehl et al., 2014). As a consequence, future research will be advocated to the evaluation of the decadal predictability of the SST anomalies in those regions influencing SESA rainfall.

Acknowledgments

Leandro Diaz acknowledges the World Climate Research Programme (WCRP) for funding his assistance to the CLIVAR Open Science Conference (Qingdao, 2016), where this work has been awarded. The research was supported by Consejo Nacional de Investigaciones Científicas y Técnicas (CONICET) PIP 112-20120100626CO, UBACyT 20020130100489BA, PIDDEF 2014/2017 Nro 15, andthe CLIMAX Project funded by Belmont Forum. Leandro Díazwas supported by a PhD grant from CONICET, Argentina.

References

Barreiro, M., N. Díaz, and M. Renom, 2014: Role of the global oceans and land-atmosphere interaction on summertime interdecadal variability over northern Argentina. Clim. Dyn., 42, 1733–1753, doi:10.1007/s00382-014-2088-6.

Fogt, R. L., and D. H. Bromwich, 2006: Decadal variability of the ENSO teleconnection to the high-latitude south pacific governed by coupling with the Southern Annular mode. J. Clim., 19, 979–997, doi:10.1175/JCLI3671.1.

Grimm, A. M., 2011: Interannual climate variability in South America: Impacts on seasonal precipitation, extreme events, and possible effects of climate change. Stoch. Environ. Res. Risk Assess., 25, 537–554, doi:10.1007/s00477-010-0420-1.

Hartmann, D. L., and Coauthors, 2013: Observations: Atmosphere and surface. Climate Change 2013: The Physical Science Basis, T. F. Stocker et al., Eds., Cambridge University Press, 159–254.

Kayano, M. T., and R. V. Andreoli, 2007: Relations of South American summer rainfall interannual variations with the Pacific Decadal Oscillation. Int. J. Climatol., 27, 531–540, doi:10.1002/joc.1417.

Kayano, M. T., and V. B. Capistrano, 2014: How the Atlantic multidecadal oscillation (AMO) modifies the ENSO influence on the South American rainfall. Int. J. Climatol., 34, 162–178, doi:10.1002/joc.3674.

Kiladis, G. N., and H. F. Diaz, 1989: Global Climatic Anomalies Associated with Extremes in the Southern Oscillation. J. Clim., 2, 1069–1090, doi:10.1175/1520-0442(1989)002<1069:GCAAWE>2.0.CO;2.

Liebmann, B., C. Vera, L. Carvalho, I. Camilloni, M. Hoerling, D. Allured, V. Barros, J. Báez, and M. Bidegain, 2004: An Observed Trend in Central South American Precipitation. J. Climate, 17, 4357–4367, doi: 10.1175/3205.1.

Martín-Gómez, V., E. Hernández-Garcia, M. Barreiro, and C. López, 2016: Interdecadal Variability of Southeastern South America Rainfall and Moisture Sources during the Austral Summertime. J. Climate, 29, 6751–6763, doi: 10.1175/JCLI-D-15-0803.1.

Meehl, G., L. Goddard, G. Boer, R. Burgman, G. Branstator, C. Cassou, S. Corti, G. Danabasoglu, F. Doblas-Reyes, E. Hawkins, A. Karspeck, M. Kimoto, A. Kumar, D. Matei, J. Mignot, R. Msadek, A. Navarra, H. Pohlmann, M. Rienecker, T. Rosati, E. Schneider, D. Smith, R. Sutton, H. Teng, G. van Oldenborgh, G. Vecchi, and S. Yeager, 2014: Decadal Climate Prediction: An Update from the Trenches Bull. Amer. Meteor. Soc., 95, 243–267, doi: 10.1175/BAMS-D-12-00241.1.

Penalba, O. C., and F. A. Robledo, 2010: Spatial and temporal variability of the frequency of extreme daily rainfall regime in the La Plata Basin during the 20th century. Clim. Change, 98, 531–550, doi:10.1007/s10584-009-9744-6.

Re, M., and V. R. Barros, 2009: Extreme rainfalls in SE South America. Clim. Change, 96, 119–136,doi:10.1007/s10584-009-9619-x.

Robledo, F. A., O. C. Penalba, and M. L. Bettolli, 2013: Teleconnections between tropical-extratropical oceans and the daily intensity of extreme rainfall over Argentina. Int. J. Climatol., 33, 735–745, doi:10.1002/joc.3467.

Ropelewski, C. F., and M. S. Halpert, 1987: Global and Regional Scale Precipitation Patterns Associated with the El Niño/Southern Oscillation. Mon. Weather Rev., 115, 1606–1626, doi:10.1175/1520-0493(1987)115<1606:GARSPP>2.0.CO;2.

Saurral, R. I., I. A. Camilloni, and V. R. Barros, 2016: Low-frequency variability and trends in centennial precipitation stations in southern South America. Int. J. Climatol., doi:10.1002/joc.4810.

Schneider, U., A. Becker, P. Finger, A. Meyer-Christoffer, B. Rudolf, and M. Ziese, 2011: GPCC Full Data Reanalysis Version 6.0 at 2.5°: Monthly Land-Surface Precipitation from Rain-Gauges built on GTS-based and Historic Data, doi: 10.5676/DWD_GPCC/FD_M_V7_250

Smith, T. M., R. W. Reynolds, T. C. Peterson, and J. Lawrimore, 2008: Improvements to NOAA's historical merged land-ocean surface temperature analysis (1880-2006). J. Clim., 21, 2283–2296, doi:10.1175/2007JCLI2100.1.

Taylor, K. E., R. J. Stouffer, and G. A. Meehl, 2012: An overview of CMIP5 and the experiment design. Bull. Am. Meteorol. Soc., 93, 485–498, doi:10.1175/BAMS-D-11-00094.1.

Venegas, S. A., L. A. Mysak, and D. N. Straub, 1997: Atmosphere-ocean coupled variability in the South Atlantic. J. Clim., 10, 2904–2920, doi:10.1175/1520-0442(1997)010<2904:AOCVIT>2.0.CO;2.

Vera, C., G. Silvestri, V. Barros, and A. Carril, 2004: Differences in El-Niño response over the southern hemisphere. J. Clim., 1741–1753, doi:10.1175/1520-0442(2004)017<1741:DIENRO>2.0.CO;2.

Vera, C. S., and L. Díaz, 2015: Anthropogenic influence on summer precipitation trends over South America in CMIP5 models. Int. J. Climatol., 35, 3172–3177, doi:10.1002/joc.4153.

On the relative importance of dynamical and stochastic contributions to Atlantic Niño SST variability

Tina Dippe[1], Richard Greatbatch[1], Hui Ding[2]

[1]GEOMAR Helmholtz Centre for Ocean Research Kiel, Germany

[2]Cooperate Institute for Research in Environmental Sciences - University of Colorado and NOAA Earth Systems Research Laboratory, Boulder, USA

Contact e-mail: *tdippe@geomar.de*

Introduction

The Atlantic Niño is the dominant mode of interannual variability in equatorial Atlantic sea surface temperature (SST). It modulates the seasonal development of the equatorial Atlantic cold tongue and peaks during May-August (Xie & Carton, 2004). Similar to other modes of equatorial SST variability, it is the source of a number of teleconnections (Mohino & Losada, 2015), both regionally and globally. Via its close relationship with the meridional location of the Inter-Tropical Convergence Zone, it especially affects rainfall variability over the surrounding continents, exerting a non-negligible socio-economic impact (Hirst & Hastenrath, 1983).

Efforts to simulate and predict equatorial Atlantic seasonal-to-interannual SST variability with state-of-the-art coupled global climate models (CGCMs) have, so far, not been successful (Stockdale et al. , 2006). One reason for this is that most CGCMs suffer from a strong coupled bias in the tropical Atlantic that alters the physical mechanisms establishing and modulating the tropical Atlantic mean state, including the summer cold tongue (e.g. Richter & Xie, 2008; Grodsky et al. , 2012; Wang et al. , 2014). Another reason is that the dynamics of the Atlantic Niño are not fully understood yet. In a recent study based on CMIP3 simulations, Nnamchi et al. , 2015 proposed that the Atlantic Niño may be driven by stochastic processes in the atmosphere. This is in contrast to a number of older publications that identify the (dynamical) Bjerknes feedback as the driver of the Atlantic Niño variability (e.g. Zebiak, 1993; Keenlyside & Latif, 2007).

Here, we address two questions: First, do dynamical processes contribute to SST variability in the tropical Atlantic? Is there a seasonality to the ratio of dynamical and stochastic contributions? And second, does the presence of the SST bias affect the models' ability to accurately reproduce the observed dynamical SST variance? To answer these questions, we use two assimilation runs of the Kiel Climate Model and reanalysis data and decompose SST variance into a part that is due to dynamical processes in the ocean and a stochastic part due to noise.

Impact of heat flux correction on the modelled Atlantic cold tongue

With the Kiel Climate Model (KCM, Park et al. 2009), we perform two sets of experiments. The first set uses a standard version of the KCM ("STD"). The STD SST climatology contains the SST bias in the southern subtropical Atlantic, which is qualitatively comparable to corresponding biases in other CGCMs (shown for example by Davey et al., 2002; Richter & Xie, 2008). Importantly, the STD run fails to establish the summer cold tongue in May-August. The second experiment employs additional surface heat flux correction ("FLX", see Ding et al., 2015 for the method) to reduce the SST bias. While the annual mean bias in the eastern tropical Atlantic (Atl3, 20°W to 0°E, 3°S to 3°N) is strongly reduced in this experiment, the initial cooling of the cold tongue in April is too weak, effectively delaying the onset of the cold tongue by about one month. We expect that this delay is due to a zonal wind stress bias that occurs in the western tropical Atlantic and is strongest in April and May, when the magnitude of the model wind stress is substantially too weak. In agreement with the observational study of Marin et al. (2009), we suspect that the weak spring wind stress systematically fails to precondition the Atl3 thermocline and inhibits an earlier onset of surface cooling. As a result, Atl3 in FLX is roughly 1.2°C warmer than observations in May-July. In August, the cold tongue in FLX, too, is fully established and FLX SSTs converge with observed SST. Both experiments were conducted in partially coupled mode (e.g. Ding et al., 2013). In partial coupling, the ocean and sea-ice components of the coupled model are forced with observed wind stress anomalies — obtained from ERA-Interim, in our case — that are added to the model's native wind stress climatology. To compare our experiments with the real world, we use ERA-Interim for SST and zonal wind (u10), and AVISO for sea surface height (SSH).

SST variance decomposition

Observed total SST variance in Atl3 is characterised by a clear peak in May-July and a secondary peak in November-December (Fig. 1a). While STD fails to simulate this variance distribution, FLX is able to produce a summer variance peak in July-August. The delay in peak variance in FLX is in agreement with the delayed onset of the cold tongue.

To assess how dynamical processes contribute to total SST variance in Atl3, we decompose SST variance into a dynamically driven and a stochastically forced component. The canonical approach for such a decomposition is to equate the ensemble mean of a simulation with the dynamical contribution to a signal. The observed climate record, however, corresponds to a single realisation of a climate simulation and does not allow for such a simple decomposition.

Our alternative decomposition approach uses empirical models of dynamical SST with multiple predictors. We base our choice of SST predictors on processes in the coupled equatorial ocean-atmosphere system that have a demonstrated impact on SST: The (i) thermocline and (ii) zonal advection feedbacks both support the growth of SST anomalies and are in turn related to the Bjerknes feedback (Bjerknes, 1969). We represent these feedbacks by our predictors of dynamical SST: (i) Sea surface height (SSH) is strongly related to the equatorial thermocline depth and upper ocean heat content and is our stand-in for the thermocline feedback. (ii) Zonal surface wind anomalies (u10) are related to zonal surface current anomalies and hence to the zonal advection feedback. We estimate the parameters of our empirical models of dynamical SST via least-squares fitting of SSH and u10 to SST. All variables are used in their anomaly form. We build separate models for observations (ERA-Interim/AVISO) and the two KCM experiments (FLX, STD). Note that for our empirical models based on the KCM experiments, we use observed u10 instead of model u10. The reason is that our KCM experiments are partially coupled: The ocean does not "see" the modeled, but observed wind stress anomalies. For each ensemble member and calendar month, we build a separate empirical model. We identify the response of our empirical model to our two predictor variables SSH and u10 as dynamical SST. Stochastic SST is the difference between the dynamical SST and the full SST (anomaly) that we used to build our empirical models with. Dynamical and stochastic SST variances are obtained as follows: For observations, we compute the variance of the two SST datasets for each calendar month. For the model experiments, we concatenate the (dynamical and stochastic SST) data for each calendar month from all ensemble members, and then compute the variance of the extended SST time series.

When we compare our empirical SST variance decomposition approach with the ensemble-averaging approach for our two experiments, we find that it is a valid approximation.

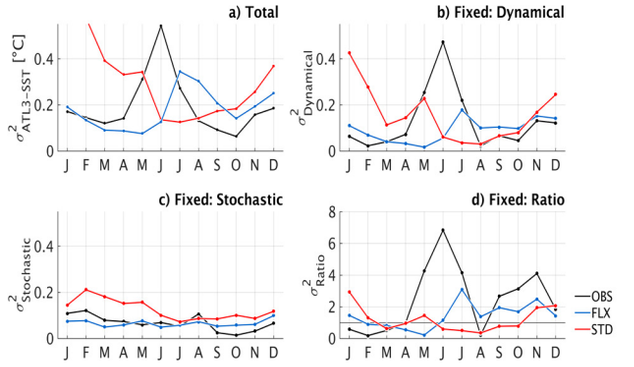

Figure 1: Atl3 seasonal cycle of **(a)** total variance, **(b)** dynamical variance, **(c)** stochastic variance, and **(d)** the ratio of dynamical and stochastic variance, for (black, blue, red) ERA-Interim/AVISO, FLX, and STD. Note that the total STD variance in (a) is not shown completely due to y-axis scaling. The missing values for January and February are 0.67 and 0.58°C^2, respectively.

Results: Impact of a realistic background state on the strength of dynamical SST variance

Figs. 1b,c show the dynamical and stochastic SST variances from our empirical model for Atl3. The ratio of the two variances is shown in Fig. 1d.

Observations: Observed dynamical SST clearly dominates SST variance during early boreal summer (May-July, Fig. 1b, black line). Dynamical SST variance then is roughly 4-7 times larger than the stochastic contribution to total SST variability (Fig. 1c). A secondary peak occurs during October and November. These two periods of enhanced dynamical SST variability are separated by phases during which stochastic SST variance is larger than dynamical SST variance. This is the case in January-March and again in August, when dynamical SST variance vanishes and observed stochastic SST variance reaches its peak. Note that observed stochastic SST variance is much less variable over the course of the year (Fig. 1c). This implies that stochastic SST variance is indeed driven by processes that are independent of seasonal processes — it represents noise. Lastly, comparing (observed) dynamical SST variance with total (observed) SST variance (Figs. 1a,b) shows a generally good agreement. This suggests that the (observed) seasonal cycle of total SST variability in Atl3 is largely shaped by the variable dynamical contribution.

Model simulations: FLX dynamical and stochastic SST variances are comparable to observations (blue). Dynamical SST variance peaks in boreal summer and again, more weakly, in early boreal winter (Fig. 1b). However, the timing of the dynamical SST variance peaks does not match observations: The summer peak lags

behind observations by one month and is strongly reduced in amplitude. The absolute minimum of dynamical SST variance occurs in May, when observed dynamical SST variance is already high and contributes substantially to the overall boreal summer peak. Additionally, dynamical SST variance does not decrease as strongly in August, and the secondary peak is hardly a peak at all.

The reason for these shortcomings in the FLX dynamical SST is most likely related to systematic differences between the observed and heat-flux corrected seasonal cycles. In the framework of our empirical models, the one-month delay in the climatological onset of the cold tongue development in FLX explains the absence of dynamical processes during May: These processes depend on the presence of the cold tongue. However, once the cold tongue is established, the feedbacks set in and contribute to dynamical SST variability.

FLX Stochastic SST variance is similar to observations in both magnitude and seasonality (Fig. 1c). The ratio of the variances in the FLX run bears similarities to observations but lacks the clear double peak structure (Fig. 1d): Dynamical SST variance does not vanish in FLX, as it does in August in the observations. One reason could be that, similar to the delayed cooling during the onset of the cold tongue, initial warming in August-September is weaker in FLX than in observations. In contrast to observations, where August disrupts the surface-subsurface coupling in Atl3 (see below), the thermocline feedback stays active in FLX.

The STD experiment does not capture the observed SST variance distribution (red). On the contrary: Dynamical SST variance is at its lowest in July-August and increased in boreal winter. In fact, once the observed cold tongue has dissolved and the SST bias decreases—in other words: when our empirical models operate on similar background states in observations, FLX, and STD—dynamical SST variance is comparable to observations and FLX.

These findings suggest that the background state, i.e. the seasonal cycle of the system is crucial for a realistic simulation of dynamical SST variance. While the FLX experiment is not perfect, it clearly improves the STD experiment, whose background state lacks the Atlantic cold tongue.

Additionally, our findings show that observed SST is clearly dominated by dynamical SST variance in May-July. This coincides with the peak phase of the Atlantic Niño and suggests that a major part of the Atlantic Niño-variability could indeed be caused by dynamical, i.e. predictable ocean processes. This is at odds with the results of Nnamchi et al., 2015. A reason could be that Nnamchi et al., 2015 did not take fully into account the fundamental impact that the tropical Atlantic bias has on the coupled climate system. Note that our analysis of STD, too, suggests that SST variability in summer is mainly driven by stochastic processes (Fig. 1d). However, the bias inhibits the development of the cold tongue in the Atlantic in STD. The processes that are responsible for dynamical SST variability can not act on the thermocline-SST-zonal wind-system under these circumstances. Observed SST variability — with its strong dynamically driven contribution — can not be established.

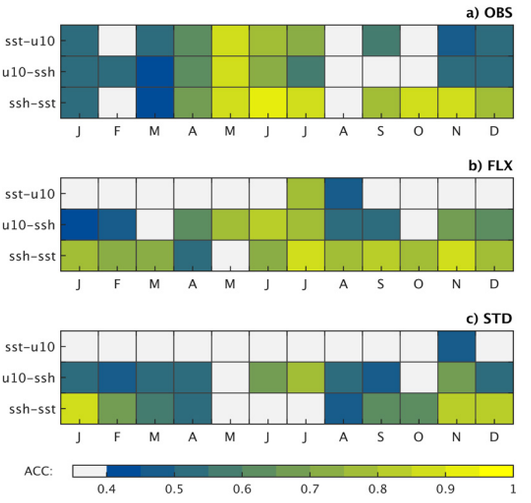

Figure 2: Instantaneous relationships between SST, u10, and SSH in the tropical Atlantic for **(a, b, c)** observations, FLX, and STD. The relationship strength is measured via the anomaly correlation coefficient (ACC). ACC values that are not significantly different from 0 at the 95% level according to a Student t test are shown in grey.

Concluding remarks

To conclude our study, we consider the relationships between our predictors and Atl3 SST (Fig. 2). Our motivation is that SST, SSH, and u10 are not independent of each other in the tropical ocean basins. Rather, they are related to each other by the Bjerknes feedback (Bjerknes, 1969), the positive feedback mechanism that lends growth to the Pacific and Atlantic Niños. The three elements of the feedback are: (i) Eastern ocean basin SST anomalies force u10 anomalies in the western ocean basin, (ii) u10 anomalies trigger a thermocline (in our framework: SSH) response across the basin, and (iii) eastern basin thermocline anomalies amplify the initial SST anomaly. A closed Bjerknes feedback loop is present when all three elements of the Bjerknes feedback are active simultaneously. Here, we assess the instantaneous relationships between these three key variables. The strength of the three feedback elements varies over the course of the year. In observations (Fig. 2a), feedback elements concerned with wind variability are generally strongest in early boreal summer. The coupling between the subsurface and surface captured in the SSH-SST relationship on the other hand appears to be strong from late boreal spring through to boreal winter, with the notable exception of August, when the

ACC values for the two thermocline relationships dip. This implies that the communication between surface processes and the ocean interior temporarily fades in late boreal summer, disrupting the closed Bjerknes feedback loop that was persisting from April to July.

The KCM experiments struggle to capture the observed relationships that form the instantaneous Bjerknes feedback in the tropical Atlantic (Figs. 2b,c). For example, the FLX and STD SST-u10 relationships are hardly captured at all. A single exception is July in the FLX experiment: Here, the KCM captures a relationship that is comparable to observations and is able to simulate a closed Bjerknes feedback loop. Note that FLX simulates a reasonable SSH-SST relationship in boreal winter, but fails to produce this crucial relationship in May. Again, we suspect that the bias in the onset of the cold tongue is responsible for this behaviour: Because cold tongue development only really sets in in June in FLX, the thermocline cannot communicate with SST in May. FLX fails to establish the observed relationship. For the same reason, STD is not able to produce the SST-SSH relationship of the instantaneous Bjerknes feedback in boreal summer. While STD does not produce a closed Bjerknes feedback at all, it is limited to July in FLX.

In summary, our analysis shows that dynamical contributions to SST variability dominate SST variance during the peak phase of the Atlantic Niño in observations, and again in early boreal winter. The bias inhibits important processes that help to establish dynamical SST variance. When the bias issue is addressed, the KCM, too, simulates a boreal summer contribution to SST variability that is dynamical in nature. However, a number of issues remain in the FLX experiment that need to be addressed in future research, among them the delay in cold tongue onset and the inability of the FLX mode to simulate a closed Bjerknes feedback loop.

References

Bjerknes, J. 1969. Atmospheric Teleconnections From The Equatorial Pacific. Monthly weather review, 97(3), 163-172.

Davey, M., Huddleston, M., Sperber, K., Braconnot, P., Bryan, F., Chen, D., Colman, R., Cooper, C., Cubasch, U., Delecluse, P., DeWitt, D., Fairhead, L., Flato, G., Gordon, C., Hogan, T., Ji, M., Kimoto, M., Kitoh, A., Knutson, T., Latif, M., Le Treut, H., Li, T., Manabe, S., Mechoso, C., Meehl, G., Power, S., Roeckner, E., Terray, L., Vintzileos, A., Voss, R., Wang, B., Washington, W., Yoshikawa, I., Yu, J., Yukimoto, S., & Zebiak, S. 2002. STOIC: A study of coupled model climatology and variability in tropical ocean regions. Climate dynamics, 18(5), 403-420.

Ding, Hui, Greatbatch, Richard J., Park, Wonsun, Latif, Mojib, Semenov, Vladimir a., & Sun, Xuguang. 2013. The variability of the East Asian summer monsoon and its relationship to ENSO in a partially coupled climate model. Climate dynamics, 42(1-2), 367-379.

Ding, Hui, Greatbatch, Richard J., Latif, Mojib, & Park, Wonsun. 2015. The impact of sea surface temperature bias on equatorial Atlantic interannual variability in partially coupled model experiments. Geophysical research letters, 42(13), 5540-5546.

Grodsky, Semyon A., Carton, James A., Nigam, Sumant, & Okumura, Yuko M. 2012. Tropical Atlantic Biases in CCSM4. Journal of climate, 25(11), 3684-3701.

Hirst, Antrony C, & Hastenrath, Stefan. 1983. Atmosphere-ocean mechanisms of climate anomalies in the Angola-tropical Atlantic sector. Journal of physical oceanography, 13(7), 1146-1157.

Keenlyside, Noel S, & Latif, Mojib. 2007. Understanding Equatorial Atlantic Interannual Variability. Journal of climate, 20(1), 131-142.

Marin, Frederic, Caniaux, Guy, Giordani, Herve, Bourles, Bernard, Gouriou, Yves, & Erica, Key. 2009. Why Were Sea Surface Temperatures so Different in the Eastern Equatorial Atlantic in June 2005 and 2006? Journal of physical oceanography, 39(6), 1416-1431.

Mohino, Elsa, & Losada, Teresa. 2015. Impacts of the Atlantic Equatorial Mode in a warmer climate. Climate dynamics, 45(7-8), 2255-2271.

Nnamchi, Hyacinth C, Li, Jianping, Kucharski, Fred, Kang, In-Sik, Keenlyside, Noel S, Chang, Ping, & Farneti, Riccardo. 2015. Thermodynamic controls of the Atlantic Nino. Nat commun, 6(nov).

Park, W, Keenlyside, N, Latif, M, Stroh, A, Redler, R, Roeckner, E, & Madec, G. 2009. Tropical Pacific Climate and Its Response to Global Warming in the Kiel Climate Model. Journal of climate, 22 (1), 71-92.

Richter, Ingo, & Xie, Shang-Ping. 2008. On the origin of equatorial Atlantic biases in coupled general circulation models. Climate dynamics, 31(5), 587-598.

Stockdale, Timothy N, Balmaseda, Magdalena A, & Vidard, Arthur. 2006. Tropical Atlantic SST Prediction with Coupled Ocean-Atmosphere GCMs. Journal of climate, 19(23), 6047-6061.

Wang, Chunzai, Zhang, Liping, Lee, Sk, Wu, Lixin, & Mechoso, Carlos R. 2014. A global perspective on CMIP5 climate model biases. Nature climate change, 4 (February), 201-205.

Xie, Shang-Ping, & Carton, James A. 2004. Tropical Atlantic Variability: Patterns, Mechanisms, and Impacts. Pages 121-142 of: Earth's climate. American Geophysical Union.

Zebiak, S. E. 1993. Air-sea interaction in the equatorial Atlantic region. Journal of climate 6(8), 1567-1586

A stronger Indonesian Through flow Related to Enhanced Regional Rainfall

Shijian Hu[1,2,3,4], Janet Sprintall[2]

[1]Key Laboratory of Ocean Circulation and Wave, Institute of Oceanology, Chinese Academy of Sciences, Qingdao, China

[2]Scripps Institution of Oceanography, U.C. San Diego, La Jolla, California, USA

[3]University of Chinese Academy of Sciences, Beijing, China

[4]Laboratoryfor Ocean and Climate Dynamics, Qingdao National Laboratory for Marine Science and Technology, Qingdao, China

Contact e-mail: *sjhu@qdio.ac.cn*

Introduction

The Indonesian Seas are of unique importance in the ocean and climate system of the planet. They provide the only pathway that connects tropical ocean basins and contribute significant inter-ocean exchanges of heat and freshwater via the Indonesian Throughflow (ITF, Fig 1). The ITF is a strong current with a complicated structure and a mean volume transport of about 15 Sverdrup (Sv, 1 Sv=10^6 m^3 s^{-1}, positive for westward transport) that flows through various straits and passages of the Indonesian archipelago (Fig 1). The ITF plays an important part in the global thermohaline circulation system and has been paid long-term and wide attention by the international community of ocean circulation and climate research (e.g., Gordon, 1986; Sprintall et al., 2014).

The Indonesian Seas are located in the Inter-tropical Convergence Zone that has one of the highest mean precipitation rates in the world ocean. The ITF thus gains massive freshwater from the atmosphere at the sea surface and from the surrounding regions including the South China Sea and western Pacific Ocean via horizontal advection. Due to strong tidal mixing, freshwater input and wind-forced ocean stirring in the Indonesian Seas, ITF waters fed by the tropical western Pacific Ocean and South China Sea are strongly mixed and the temperature-salinity relationship in the ITF is significantly modulated (Hautala et al., 1996; Gordon and Susanto, 2001; Koch-Larrouy et al., 2010; Valsala et al., 2011; Gordon et al., 2012; Sprintall et al., 2012, 2014).

An early hypothesis suggested that the ITF is controlled by the pressure gradient over the western Pacific and Indian Oceans (Wyrtki, 1987). The hypothesis has been verified to a large extent by numerous studies (e.g. Clarke and Liu, 1994; Meyers, 1996; Sprintall et al.,2000, 2003, 2009; Susanto et al., 2000; Wijffels and Meyers, 2004), the wind forcing over the tropical Indo-Pacific Oceans as well as oceanic waves forced by the wind forcing are a major cause of temporal variability of the ITF. However the pressure gradient is also determined by buoyancy contributions from both haline (salinity) variations and thermal (temperature) contributions. For example, the building up and dissipation of a freshwater plug in the western Sulawesi Sea and Java Sea associated with ENSO-related variability of the South China Sea Throughflow, is found to influence the Makassar Strait Throughflow(Gordon et al., 2012). Andersson and Stigebrandt (2005, hereafter AS05) put forward the importance of buoyancy forcing in the ITF transport variability particularly that associated with the significant freshwater flux. AS05 suggested that the control of the ITF is set by the baroclinic transport capacity of the region where the ITF enters into the Indian Ocean relative to the adjacent "background" Indian Ocean that is not directly influenced by the ITF.

Hu and Sprintall(2016, hereafter HS16) applied the methodology proposed by AS05 and separated out the salinity effect from the temperature effect to produce a total outflow proxy transport time series from temperature and salinity data. HS16 found that the salinity effect contributes about 36(±7)% to the total interannual variability of ITF transport. This implies that the salinity variability in the Indonesian Seas plays an important role, although not the dominant role, in determining the interannual variability of total ITF transport. Ocean salinity in the Indonesian Seas is clearly modulated by freshwater input from the sea surface, and salinity anomaly signals seem to propagate toward the Indian Ocean along the ITF pathway due to horizontal advection by the ITF (HS16).

Under the context of warming climate scenarios, it is suggested that the climate system would experience 'wet-gets-wetter' (Chou et al., 2009) and 'warmer-gets-wetter' (Tan et al., 2015) trend. In addition, the Indonesian

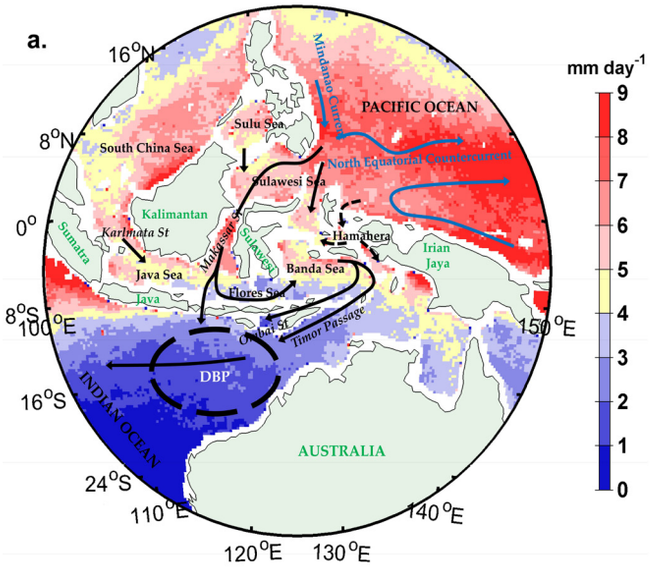

Figure 1: (a) Mean rainfall rate (color, unit in mm day-1) from the Tropical Rainfall Measuring Mission (TRMM) data and averaged over January 1998 - December 2008.

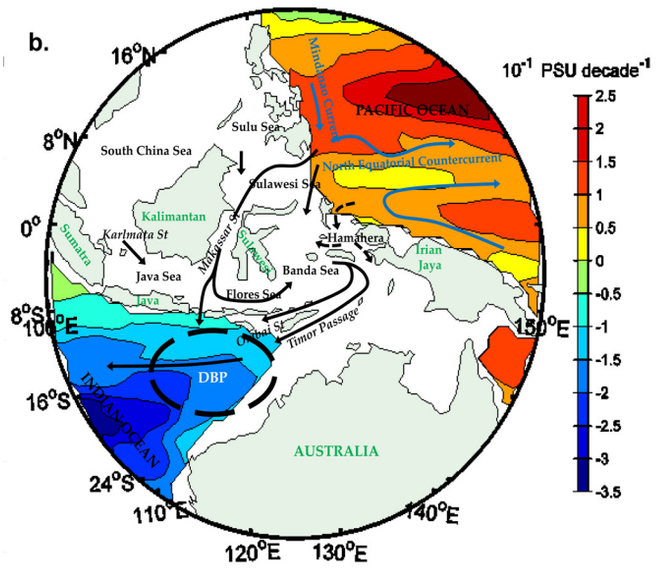

(b) linear trend of Argo salinity (unit in 10-1 PSU decade-1) averaged over the upper 200-dbar during 2004-2014. The ITF pathways are indicated in black arrows according to Sprintall et al. 2015. The dashed black ellipse indicates where the ITF enters into the Indian Ocean.

region has experienced a decadal increase in rainfall due to a phase change of the Inter-decadal Pacific Oscillation (IPO) (Dong and Dai, 2015). Therefore, it is of interest to determine how the ITF responds to the intensified precipitation and how this might impact ITF heat and freshwater transports into the Indian Ocean.

Method and Data

The method used by AS05 and HS16 is used to calculate the proxy ITF transport anomaly (ITF') and its salinity contribution (ITF_S') and temperature contribution (ITF_T'). For details of the method, please see the papers by AS05 and HS16. Here we present some primary results from a recent study by Hu and Sprintall (2017).

As described by HS16, temperature and salinity data in the eastern Indian Ocean and where the ITF enters into the North Australian Basin are needed to calculate density and the ITF volume transport. The analysis is focused on the recent Argo era since 2004 when salinity observations become relatively abundant. Temperature and salinity data used include: (a) the Roemmich-Gilson Argo Climatology monthly gridded data (Roemmich and Gilson, 2009) produced from Argo profiles over the period 2004–2014 with a horizontal resolution of 1°×1°; (b) the EN4 data set Version 4.1.1 from the Met Office Hadley Centre (Good et al., 2013); (c) the European Centre for Medium-Range Weather Forecasts Ocean Analysis/Reanalysis System 3 (ECMWF-ORA S3) (Balmaseda et al., 2008); and (d) the Ensemble Coupled Data Assimilation v3.1 from the NOAA Geophysical Fluid Dynamics Laboratory (GFDL-ECDA) (Chang et al., 2013). Results from three reanalysis/assimilation datasets (EN4, ECMWF-ORA S3 and GFDL-ECDA) are used to make an ensemble mean and compared to the ITF derived from the Argo climatology data set. Direct measurements of the ITF transport from the INSTANT (International Nusantara Stratification and Transport program, Sprintall et al., 2004) moorings were used by US16 to verify the method and the results (Sprintall et al., 2009).

Climatological rainfall rate data (averaged over January 1998 - December 2008) from the Tropical Rainfall Measuring Mission (TRMM) (Theon, 1994) illustrate the spatial structure of precipitation over the Indonesian archipelago. An "Evaporation minus Precipitation" (E-P) time series is also estimated using the monthly surface precipitation (P) time series from the Global Precipitation Climatology Project (GPCP) analysis (Adler et al., 2003), with a resolution of 2.5°× 2.5° (January 1979 to December 2014), and the monthly evaporation (E) provided by the Objectively Analyzed air-sea Fluxes (OAFlux, 1985–2012) (Yu et al., 2008).

Results

The 2004–2006 ITF mean volume transports calculated by HS16 using the Argo data is about 15 Sv which, along with the time series variability, agrees well with directly observations over the same period (Sprintall et al., 2009; HS16).An ensemble mean based on the proxy ITF time series computed using the EN4 data, ECMWF-ORA S3 and GFDL-ECDA is calculated and the trends are determined through linear regression (Table 1). The ensemble mean ITF_T' has a significant decreasing trend of -2.2 Sv decade^{-1} during 1970-2010, while the ITF_S' shows a significant increasing trend of 1.8 Sv decade^{-1}. The two components together lead to a slightly decreasing trend of -0.4 Sv decade^{-1} in the whole ITF'. During the period between 2002 and 2010, the increasing trend of the ITFT'

rises to 0.9 SV decade^{-1} and is still not significant, but the ITF_S' shows a significant increasing trend with a rate of 4.6 SV decade^{-1}. As a result, the ITF' shows a significant increasing trend of 5.8 SV decade^{-1}. Linear trends of the ITF' and its components estimated from the gridded Argo Climatology data set show a comparable significant increasing trend of about 5.9 SV decade^{-1} in ITF'. This trend is mainly a result from the significant increasing trend of 4.1 SV decade^{-1}in the ITF_S', while the increasing trend of 1.8 SV decade^{-1} in the ITF_T' is not significant (Table 1). Therefore, the ensemble mean ITF transport from the reanalysis data sets indicate a similar trend to that resolved by the ITF transport determined from the Argo Climatology data set. Most importantly, the increasing trend in the ITF transport during the past decade is primarily induced by the increase of the halosteric component ITF_S'.

As described by AS05 and HS16, the freshwater input influences the ITF transport by regulating the salinity and density structure in the region where the ITF enters the Indian Ocean. Linear trends of the in situ temperature and salinity in the upper 200 dbar show a significant warming trend in the Indo-Pacific Ocean, freshening in the eastern Indian Ocean and an increasing trend in salinity for the western Pacific Ocean (Fig 1b). Hence, the source water of the ITF in the western Pacific Ocean seems to have become saltier, suggesting that the freshening trend in the outflow ITF region must be caused by the freshwater input into the surface within the Indonesian Seas.

Freshwater flux over the Indonesian Seas is investigated by calculating the linear trends of evaporation minus precipitation (E-P) during 2000-2011 (Fig 2, upper panel). Clearly the Indonesian Seas show a strong enhancement of freshwater input, which is mainly a result of intensified precipitation (not shown). In contrast, there is a significant decrease in precipitation and freshwater input over the eastern Indian and central-western Pacific Oceans. This feature explains the decreasing trend in the salinity in the region where the ITF enters the Indian Ocean and the increasing trend of the halosteric component of the ITF transport. Advection of freshwater may also contribute to the salinity trend in the ITF, but this cannot as yet be confirmed due to a lack of salinity observations in this region.

The strengthened ITF transport leads to enhancement of tropical inter-basin exchange and contributes to the ocean and climate change in the Indo-Pacific Oceans (e.g., Lee et al., 2015). Using Argo data and derived volume transport, we calculated the heat and salinity transports by the ITF, which are defined as $Q_T = Tran_{ITF} \cdot \Delta T$ and $Q_S = Tran_{ITF} \cdot \Delta S$, where $Tran_{ITF}$ is ITF transport, ΔT is temperature difference, and ΔS is salinity difference. As a result, we find that: (a) the temperature transport has a small but significant increasing trend of 5.5°C Sv decade^{-1}, suggesting a significant heat input into the Indian Ocean by the ITF; and (b) the salinity transport from the Indonesian seas shows a significant trend of about -2.8 PSU Sv decade^{-1}, indicating that the ITF transfers much more freshwater from the Indonesian Seas into the eastern Indian Ocean. The trends in heat and salinity transports by the ITF significantly contribute to the temperature and salinity trends in the eastern Indian Ocean, implying that the ITF variability induced by freshwater input plays a remarkable important role in the redistribution of heat and freshwater in the tropical Indo-Pacific Ocean.

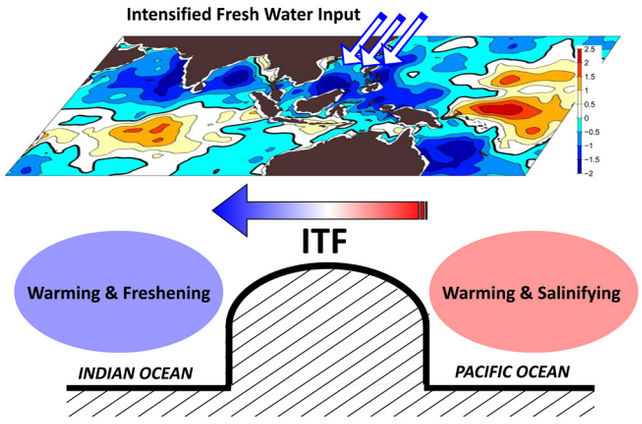

Figure 2: Schematic representation of the climate effect of the enhancement of the ITF during the past decade. Upper panel shows linear trend of (E-P) (unit: mm hour^{-1} decade^{-1}) during 2000-2011 and lower panel shows the impact that this has had on the surrounding oceans.

Discussion

The global ocean and climate system experiences strong natural inter-decadal variability and external changes forced by anthropogenic activities like increasing concentrations of greenhouse gases over the past decades (e.g., Chou et al., 2009; Hu and Hu, 2012, 2014; Dong and Dai, 2015; Hu et al., 2015; Tan et al., 2015). The long-term trend of the ITF might be related to both the background global warming trend (manifested in various regional features) and/or phase changes of inter-decadal variability. The IPO switched from a positive phase during 2004–2007 to a negative phase after 2008. Meanwhile, the precipitation during the past decades has shown a significant increasing trend in the Indonesian seas and far western Pacific Ocean that might be a result of global warming (Chou et al., 2009; Tan et al., 2015). Therefore, both the natural inter-decadal variability and external forcing are likely responsible for the intensification of the ITF transport during the past decade.

The ITF plays as a pivotal part in the global thermohaline circulation (Gordon1986; Sprintall et al. 2014), thus the intensified heat and freshwater transports by the ITF are expected to act as an important regulator in changing the global thermohaline circulation and redistributing the global pattern of heat and freshwater. Quantifying this impact needs in situ observations, especially salinity profiles, within the Indonesian and regional seas.

	Ensemble (1970-2010)	Ensemble (2002-2010)	Argo (2004-2014)
ITF'	-0.4	5.8	5.9
ITF_T'	-2.2	0.9	1.8
ITF_S'	1.8	4.6	4.1

Table 1: Trends of ITF transports (SV decade^{-1}) calculated from an Ensemble mean of the ITF computed using the EN4 data, ECMWF-ORA S3 and GFDL-ECDA for the periods (1970-2010) and (2002-2010) compared to trends of ITF transport calculated using Argo data (2004-2014).

Acknowledgments

S.H was supported by the Key Research Program of Frontier Sciences, CAS (Number QYZDB-SSW-SYS023), the National Natural Science Foundation of China (Grants 41406016 and 41421005) and the Open Fund of State Key Laboratory of Satellite Ocean Environment Dynamics, Second Institute of Oceanography, SOA (No. QNHX1601). Support for J.S. was provided by the Physical Oceanography program of the National Aeronautics and Space Administration (NASA) under grant NNX13AO38G. We are grateful to Dr. Nico Caltabiano and an anonymous Guest Editor for their helpful comments and suggestions.

References

Adler, R. F., and Coauthors, 2003: The version-2 global precipitation climatology project (GPCP) monthly precipitation analysis (1979-present). Journal of hydrometeorology, 4, 1147-1167.

Andersson, H. C., and A. Stigebrandt, 2005: Regulation of the Indonesian Throughflow by baroclinic draining of the North Australian Basin. Deep Sea Research Part I: Oceanographic Research Papers, 52, 2214-2233.

Balmaseda, M. A., A. Vidard, and D. L. Anderson, 2008: The ECMWF ocean analysis system: ORA-S3. Monthly Weather Review, 136, 3018-3034.

Chang, Y.-S., S. Zhang, A. Rosati, T. L. Delworth, and W. F. Stern, 2013: An assessment of oceanic variability for 1960–2010 from the GFDL ensemble coupled data assimilation, Climate Dyn., 40(3-4), 775-803.

Chou, C., J. D. Neelin, C.-A. Chen, and J.-Y. Tu, 2009: Evaluating the "rich-get-richer" mechanism in tropical precipitation change under global warming. Journal of Climate, 22, 1982-2005.

Clarke, A. J., and X. Liu, 1994: Interannual sea level in the northern and eastern Indian Ocean. Journal of Physical Oceanography, 24, 1224-1235.

Dong, B., and A. Dai, 2015: The influence of the Interdecadal Pacific Oscillation on Temperature and Precipitation over the Globe. Climate Dynamics, 1-15.

Good, S. A., M. J. Martin, and N. A. Rayner, 2013: EN4: quality controlled ocean temperature and salinity profiles and monthly objective analyses with uncertainty estimates. Journal of Geophysical Research: Oceans, 118, 6704-6716.

Gordon, A. L., 1986: Interocean exchange of thermocline water. Journal of Geophysical Research: Oceans (1978–2012), 91, 5037-5046.

Gordon, A. L., and R. D. Susanto, 2001: Banda Sea surface-layer divergence. Ocean Dynamics, 52, 2-10.

Gordon, A. L., B. A. Huber, E. J. Metzger, R. D. Susanto, H. E. Hurlburt, and T. R. Adi, 2012: South China Sea throughflow impact on the Indonesian throughflow. Geophysical Research Letters, 39.

Hautala, S. L., J. L. Reid, and N. Bray, 1996: The distribution and mixing of Pacific water masses in the Indonesian Seas. Journal of Geophysical Research: Oceans (1978–2012), 101, 12375-12389.

Hu, D., and Coauthors, 2015: Pacific western boundary currents and their roles in climate. Nature, 522, 299-308.

Hu, S., and D. Hu, 2012: Heat center of the western Pacific warm pool. Chin. J. Oceanol. Liimol., 30, 169 - 176.

Hu, S., and D. Hu, 2014: Variability of the Pacific North Equatorial Current from repeated shipboard acoustic Doppler current profiler measurements. J. Oceanogr., 70, 559-571.

Hu, S., and J. Sprintall, 2016: Interannual Variability of the Indonesian Throughflow: the Salinity Effect. J. Geophys. Res., 121, 2596-2615.

Hu, S., and J. Sprintall, 2017: Observed Strengthening of Interbasin Exchange via the Indonesian Seas due to Rainfall Intensification, Geophysical Research Letters, 44, doi:10.1002/2016GL072494.

Koch-Larrouy, A., M. Lengaigne, P. Terray, G. Madec, and S. Masson, 2010: Tidal mixing in the Indonesian Seas and its effect on the tropical climate system. Climate Dynamics, 34, 891-904.

Lee, S.-K., W. Park, M. O. Baringer, A. L. Gordon, B. Huber, and Y. Liu, 2015: Pacific origin of the abrupt increase in

Indian Ocean heat content during the warming hiatus, Nature Geoscience, 8(6), 445-449.

Meyers, G., 1996: Variation of Indonesian throughflow and the El Niño-Southern Oscillation. Journal of Geophysical Research: Oceans (1978–2012), 101, 12255-12263.

Roemmich, D., and J. Gilson, 2009: The 2004–2008 mean and annual cycle of temperature, salinity, and steric height in the global ocean from the Argo Program. Progress in Oceanography, 82, 81-100.

Sprintall, J., A. L. Gordon, R. Murtugudde, and R. D. Susanto, 2000: A semiannual Indian Ocean forced Kelvin wave observed in the Indonesian seas in May 1997. Journal of Geophysical Research: Oceans (1978–2012), 105, 17217-17230.

Sprintall, J., J. T. Potemra, S. L. Hautala, N. A. Bray, and W. W. Pandoe, 2003: Temperature and salinity variability in the exit passages of the Indonesian Throughflow. Deep Sea Research Part II: Topical Studies in Oceanography, 50, 2183-2204.

Sprintall, J., S. Wijffels, A. L. Gordon, A. Ffield, R. Molcard, R. D. Susanto, I. Soesilo, J. Sopaheluwakan, Y. Surachman, and H. M. Aken, 2004: INSTANT: A new international array to measure the Indonesian Throughflow, Eos, Transactions American Geophysical Union, 85(39), 369-376.

Sprintall, J., S. E. Wijffels, R. Molcard, and I. Jaya, 2009: Direct estimates of the Indonesian Throughflow entering the Indian Ocean: 2004–2006. Journal of Geophysical Research: Oceans (1978–2012), 114.

Sprintall, J., A. L. Gordon, A. Koch-Larrouy, T. Lee, J. T. Potemra, K. Pujiana, and S. E. Wijffels, 2014: The Indonesian seas and their role in the coupled ocean-climate system. Nature Geoscience, 7, 487-492.

Sprintall, J., A. L. Gordon, P. Flament, and C. L. Villanoy, 2012: Observations of exchange between the South China Sea and the Sulu Sea. Journal of Geophysical Research: Oceans (1978–2012), 117.

Sprintall, J., and A. Révelard, 2014: The Indonesian Throughflow response to Indo-Pacific climate variability. Journal of Geophysical Research: Oceans, 119, 1161-1175.

Susanto, R. D., A. L. Gordon, J. Sprintall, and B. Herunadi, 2000: Intraseasonal variability and tides in Makassar Strait. Geophysical Research Letters, 27, 1499-1502.

Tan, J., C. Jakob, W. B. Rossow, and G. Tselioudis, 2015: Increases in tropical rainfall driven by changes in frequency of organized deep convection. Nature, 519, 451-454.

Theon, J. S., 1994: The tropical rainfall measuring mission (TRMM). Advances in Space Research, 14, 159-165.

Valsala, V., S. Maksyutov, and R. Murtugudde, 2011: Interannual to interdecadal variabilities of the Indonesian Throughflow source water pathways in the Pacific Ocean. Journal of Physical Oceanography, 41, 1921-1940.

Wijffels, S., and G. Meyers, 2004: An intersection of oceanic waveguides: Variability in the Indonesian throughflow region. Journal of Physical Oceanography, 34, 1232-1253.

Wyrtki, K., 1987: Indonesian through flow and the associated pressure gradient, Journal of Geophysical Research: Oceans (1978–2012), 92(C12), 12941-12946.

Yu, L., X. Jin, and R. Weller, 2008: Multidecade Global Flux Datasets from the Objectively Analyzed Air-sea Fluxes (OAFlux) Project: Latent and sensible heat fluxes, ocean evaporation, and related surface meteorological variables. OAFlux Project Technical Report. OA-2008-01, 64pp.

An Interplay between westerly and easterly wind bursts shaping El Niño development in 2014-2016

Shineng Hu, Alexey V. Fedorov

Department of Geology and Geophysics, Yale University, New Haven, CT, USA

Contact e-mail: *shineng.hu@yale.edu*

Introduction

At the beginning of 2014, many in the scientific community anticipated that a moderate to strong El Niño could develop by year-end (e.g. NOAA CPC, 2014; ECMWF, 2014; NASA, 2014), which was supported by satellite observations and climate model forecasts. However, the event's progression quickly stalled, and formally the warm event did not qualify as El Niño (Fig. 1b).

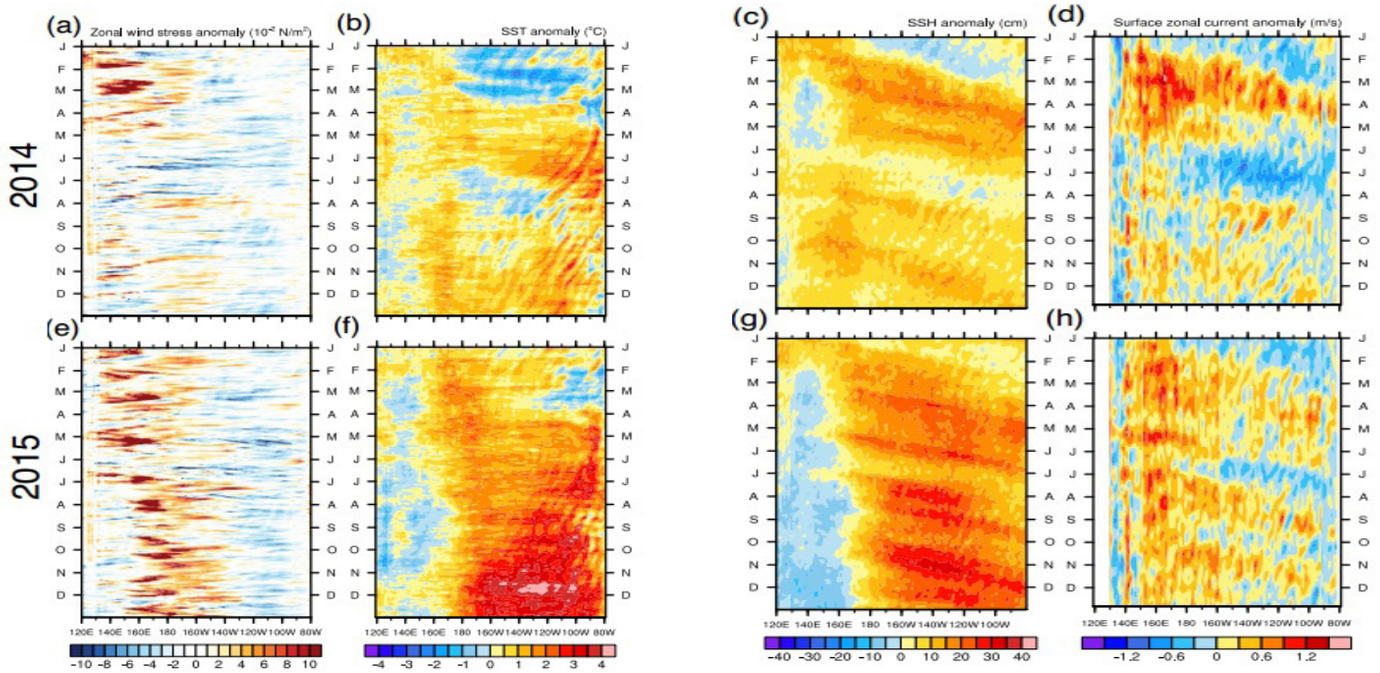

Figure 1: Hovmöller diagrams showing anomalies in **(a,e)** zonal wind stress (10^{-2} N/m^2), **(b,f)** SST (°C), **(c,g)** SSH (cm), and **(d,h)** surface zonal currents (m/s) in the equatorial Pacific during (top) 2014 and (bottom) 2015. Modified from Hu and Fedorov (2017a).

Again in early 2015, a strong El Niño was anticipated with several climate models predicting the ensemble mean wintertime Niño3.4 index close to 3°C. The 2015 event indeed reached such a large magnitude (Fig. 1f), comparable to that for the extreme El Niño events of 1997 or 1982, and continued until May-June of 2016. Here we summarize the results of our recent studies (Hu and Fedorov, 2016; 2017a) on the El Niño development in 2014-2016, focusing on the role of westerly and easterly wind bursts (WWBs and EWBs, respectively; also sometimes referred to as wind events or surges).

Westerly and easterly wind bursts

WWBs and EWBs reflect intraseasonal surface wind variability in the equatorial Pacific (Fig. 2a,b), and their occurrence results in the relaxation or strengthening of the easterly trade winds that can last from days to a few weeks (Harrison and Vecchi, 1997; Chiodi and Harrison, 2015). WWBs are typically confined to the western or central equatorial Pacific (see an example in Fig. 2c), and are often associated with twin tropical cyclones, the Madden-Julian Oscillation, or extratropical wind surges (Keen, 1982; Hartten, 1996; Seiki and Takayabu , 2007;

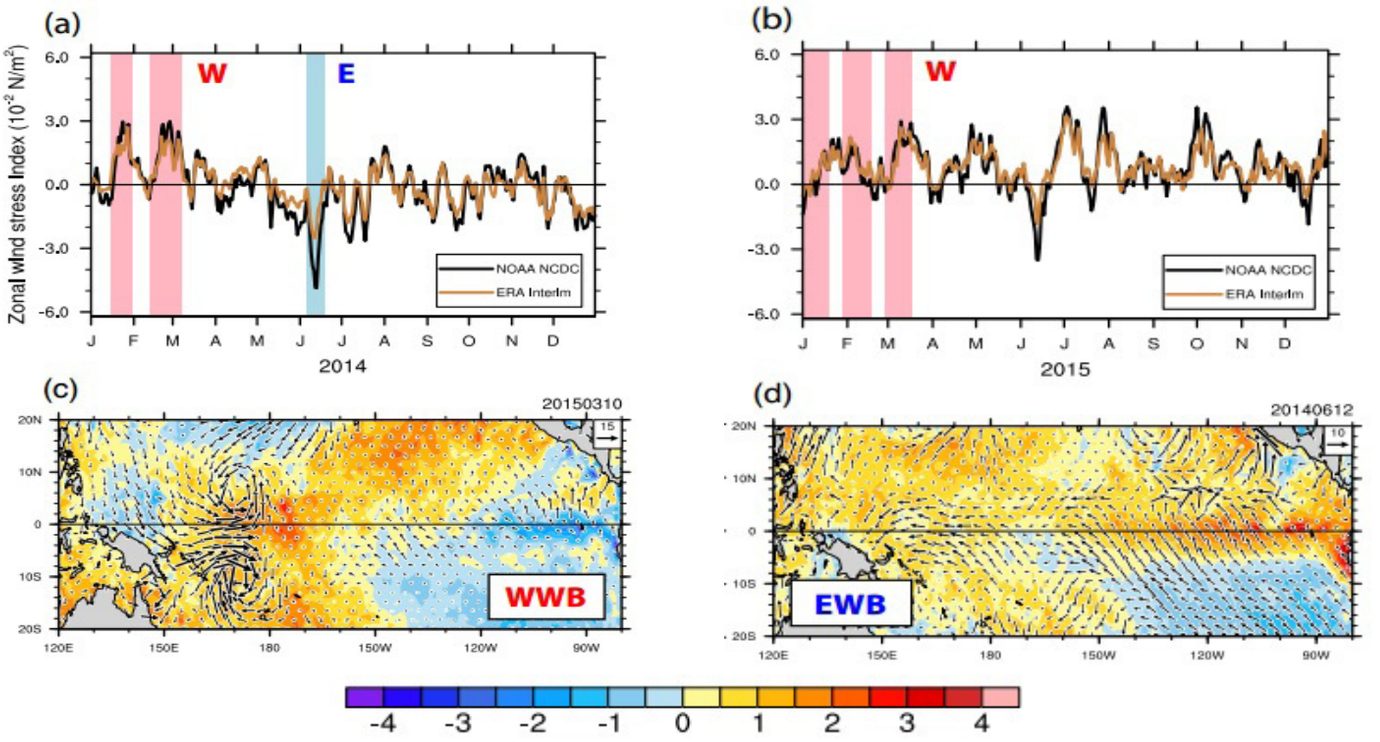

Figure 2: (a,b) Variations in the zonal wind stress indices in **(a)** 2014 and **(b)** 2015 as computed from satellite-based winds (NOAA NCDC) and an atmospheric reanalysis (ERA Interim). These indices are obtained by averaging wind stress anomalies (in 10^{-2} N/m^2) in the equatorial Pacific zonally and between 5°S-5°N. Winter-spring WWBs and the June 2014 EWB are found in both satellite observations and atmospheric reanalysis, and are highlighted by light blue and pink bands, respectively. The graphs start on January 1. (c,d) Examples of the spatial structure of these bursts. Anomalies in surface wind field (vectors; m/s) and SST (colors; °C) are shown near the peak of the bursts, for **(c)** March 10 in 2015 and **(d)** June 12 in 2014.

Harrison and Chiodi, 2009). In contrast, EWBs can have a broader spatial extent (see an example in Fig. 2d), and yet they have received little attention until recently (Su et al., 2014; Chiodi and Harrison, 2015; Hu and Fedorov, 2016).

These intraseasonal wind bursts play an important role in the development and thus the predictability of El Niño events (Kleeman and Moore, 1997; Fedorov et al., 2003,Lengaigne et al., 2004). For example, it was suggested that the 1997 extreme El Niño was precipitated by a strong WWB in March 1997 (McPhaden, 1999). Moreover, recent studies suggest that WWBs effectively modulate El Niño diversity in a broad continuum, and their impacts on El Niño development are dependent on the ocean state when the bursts occur (Hu et al., 2014; Fedorov et al., 2015). As we will show later, the recent El Niño development in 2014-2016 presents another example for how intraseasonal wind bursts affect El Niño development and predictability.

The failed El Niño of 2014

At the beginning of 2014, the western equatorial Pacific was recharged with anomalously warm water, which is favorable for El Niño development (McPhaden, 2015). In January-February, two strong WWBs occurred (Fig. 1a), pushing the warm pool eastward and exciting downwelling equatorial Kelvin waves which induced warming in the eastern Pacific (Fig. 1b-d). As a result, the anomalous equatorial SST developed two warming centers: one associated with the warm pool displacement in the central Pacific, and the other associated with thermocline deepening in the eastern Pacific induced by the Kelvin waves (Fig. 1b). These impacts of WWBs were indicative of El Niño development, and suggested a high probability of a moderate to strong El Niño event, leading to the broad expectations that an El Niño could occur by year-end.

However, the strengthening of easterly winds that started in May and culminated in an exceptionally strong easterly wind burst in June (Fig. 1a), quickly impeded the development of El Niño by pushing the warm pool back to the west and exciting an upwelling Kelvin wave (Fig. 1b-d), just opposite to what WWBs had done previously. This EWB had a basin-wide structure that extended across the entire equatorial Pacific, and was associated with a strengthening of the subtropical high in the south Pacific (Fig. 2d). In terms of the zonally-averaged zonal wind stress anomaly, this EWB turned out to be the strongest event to date in the satellite-based data (Hu and Fedorov , 2016). The burst is also evident in reanalysis products (Fig. 2a) and in-situ observations (TAO array data, http://www.pmel.noaa.gov/tao), although its magnitude differs across different datasets. Here, we rely on the satellite-based data because it has been shown to be superior

over atmospheric reanalysis products (e.g. Chelton et al. , 2004), and also because the TAO array had unfortunate observational gaps in the eastern equatorial Pacific during the time of interest in 2014 (Tollefson, 2014).

Due to the exceptional strength and basin-wide zonal extent of the June EWB, its impacts were felt almost immediately. In particular, a strong westward anomaly in ocean surface current was observed during June-July (Fig. 1d), advecting cold water from the east to the west along the equator. Between May and September of 2014, SST in the eastern Pacific decreased by 2.5°C and the warm pool retreated by 10° of longitude, far greater than typical seasonal variations during El Niño years (Hu and Fedorov, 2016). Increased local ocean heat loss to the atmosphere, associated with the stronger trade winds, should have also contributed to the cooling.

Reflection of WWBs-induced Rossby waves at the western boundary can potentially be an alternative mechanism impeding the 2014 El Niño. However, examining the spatiotemporal evolution of SSH (Fig. S5 in Hu and Fedorov, 2016), we found little evidence supporting this hypothesis. Also, the exceptional strength of the mid-summer upwelling Kelvin wave (Fig. 1d) suggests a direct wind forcing, which the June EWB together with a subsequent, weaker easterly burst could have provided.

This secondary, weaker EWB occurred in July (Fig. 2a), now confined only to the western Pacific (Fig. 1a). It was likely a part of the response of the atmospheric tropical circulation to the establishment of the local SST gradient in the western-central equatorial Pacific after the cooling caused by the June EWB (Fig. 1b).

Because of the effects of the June and to a lesser degree July EWBs, the two warming centers in the central and eastern equatorial Pacific, initially generated by the early-year WWBs, persisted throughout the year (Fig. 1b). As a result, the expected relaxation of the east-west SST gradient along the equator did not occur, inhibiting the occurrence of subsequent WWBs and thus impeding El Niño development (Fig. 1a). Eventually, the El Niño of 2014 failed to develop into a strong event – only a weak but nearly uniform warm anomaly was observed, uncharacteristically stretching along the equator from the very west to the very east (Fig. 1b).

The extreme El Niño of 2015

In the winter-spring of 2015, another series of paired cyclones was generated in the western tropical Pacific, causing strong westerly anomalies along the equator (Fig. 1e); the burst in March was especially strong (Fig. 2c). Those WWBs had similar direct dynamical impacts as those in early 2014, including downwelling Kelvin waves which propagated eastward and induced an initial warming in the eastern equatorial Pacific in April (Fig. 1f-h). At the same time, these WWBs pushed the warm pool further to the east – by April the warm pool eastern edge had already reached 160°W, which was exceptionally far even compared to the events of 1982 and 1997 (Hu and Fedorov, 2017a). In May, another strong WWB occurred, which pushed the warm pool farther eastward and enhanced the eastern equatorial warming via Kelvin waves (Fig. 1e-h). This time the warming persisted through mid-year, even though a weak EWB occurred in the central Pacific at almost the same time as in June of 2014. The event eventually peaked near the end of theyear, and the SST anomaly in the eastern Pacific reached as high as 4°C.

Thus, the developments of El Niño in 2014 and 2015 differ to a large extent in the magnitude and characteristics of the changes that occurred in the tropical Pacific in June through August. One can interpret these differences in terms of the Bjerknes feedback, that is, a reduction in the east-west equatorial SST gradient leading to weaker zonal winds and further reduction in the SST gradient. In 2015, the reduction of the east-west SST gradient along the equator gradually continued through the year, allowing a strong Bjerknes feedback that manifested in state-dependent WWBs and further warming of the eastern equatorial Pacific in the second half of the year (Fig. 1e,f). This development contrasted sharply with that during 2014 when the Bjerknes feedback was suppressed in June-July (Fig. 1a,b).

The failure of El Niño in 2014 had nevertheless important dynamical implications. We argue that in fact the 2014 event set up favorable conditions for, or preconditioned the development of the following year's extreme El Niño. This preconditioning was again shaped by the interplay of WWBs and EWBs, and had two critical components as described below.

Typically, during El Niño development, westerly wind anomalies in the western and central equatorial Pacific discharge warm water away from the equatorial band, leading to the shoaling of the thermocline along the equator (e.g. Jin, 1997). For example El Niño of 2015 exhibits such heat discharge (which begins with thermocline shoaling in the western Pacific apparent in Fig. 1g). However, in 2014, the June EWB suppressed the Bjerknes feedback, inhibiting the occurrence of subsequent westerly wind anomalies in the central Pacific (Fig. 1a), which prevented heat discharge from the equatorial band. At the same time, EWBs acted to recharge the equatorial band. The two effects together produced a recharged ocean state by the end of 2014 and early in 2015, as seen in positive basin-wide SSH anomalies along the equator (Fig. 1c,g); for further discussion see Levine and McPhaden (2016) and Hu and Fedorov (2017a).

Not less important is that the western Pacific warm pool was extended eastward at the beginning of 2015 as suggested by the warm anomaly remaining after the

2014 event (Fig. 1b). The warm pool eastern edge was positioned nearly 15 degrees of longitude farther east in January of 2015 as compared to that in January of 2014 (Hu and Fedorov, 2017a), which facilitated El Niño development (Yu et al., 2003; Lengaigne et al., 2003; Hu et al., 2014). Thus, the combination of a recharged ocean, an expanded warm pool, and strong early-year WWBs favored the development of an extreme event in 2015.

Large-ensemble coupled simulations

To verify these observation-based conclusions on the role of intraseasonal wind bursts, we conducted large-ensemble coupled simulations with the Community Earth System Model (CESM). The model simulates a realistic ENSO (Deser et al., 2012; Capotondi, 2013), well resolves oceanic Kelvin and Rossby waves critical for the system response to wind bursts, and is able to generate its own intraseasonal wind bursts that mimic the stochastic dynamics in the tropical atmosphere (Hu and Fedorov, 2016; 2017a). The ocean initial conditions are picked from a long reference run, and mimic the observations in January of 2014.

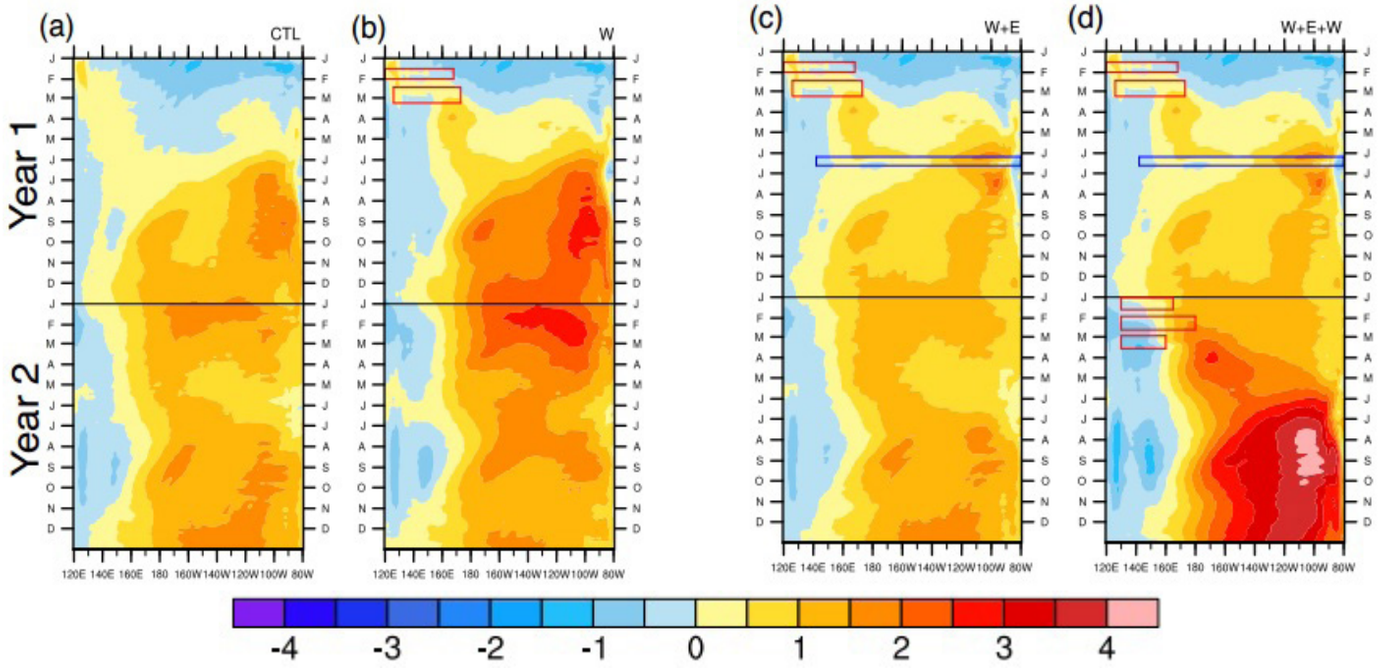

Figure 3: Hovmöller diagrams showing ensemble-mean SST anomalies (°C) in the equatorial Pacific for **(a)** the CTL set, and the perturbed sets **(b)** W, **(c)** W+E, and **(d)** W+E+W. The red and blue rectangles mark the occurrence of westerly and easterly wind bursts, respectively, superimposed in each set. Time goes downward; the horizontal black line separates Years 1 and 2. Modified from Hu and Fedorov (2017a).

Four sets of coupled simulations were conducted (named "CTL", "W", "W+E", and "W+E+W"), in which we successively add several observed WWBs and EWBs to the wind field that the model simulates. The CTL set has no externally imposed wind bursts; letters W and E represent WWBs and EWBs, respectively, highlighted in Fig. 2a,b. The timing, duration, and zonal extent of the superimposed bursts are shown in Fig. 3, and more details are provided in Hu and Fedorov (2017a). Computations last for two years and two months; hereafter we will refer to the first model year as "Year 1", and to the second model year as "Year 2". Each set of experiments includes 50 members.

Here we show the model response in the ensemble mean sense. Without any imposed bursts the CTL set develops into a moderate Central Pacific (CP) El Niño event by the end of Year 1. The W set, after two WWBs are superimposed in early months of Year 1, develops into a stronger El Niño event by the end of this year with the warming center shifted eastward, suggestive of an Eastern Pacific (EP) El Niño. The event terminates in the following year because of the heat discharge resulting from strong warm events in Year 1 (Fig. 3b). CP or EP El Niño simply refers to the warm event with maximum warming anomaly located in the central or eastern Pacific, respectively (e.g. Capotondi et al., 2015).

When we now superimpose the EWB of June of 2014, the W+E set only generates a weak El Niño by the end of Year 1 with a nearly uniform warm anomaly stretching along the equator (Fig. 3c), which resembles the conditions observed in 2014 (Fig. 1b). The resulting warming is a little weaker than that in the CTL. Thus, the effect of the imposed EWB, in the ensemble mean sense, is to negate the impacts of the WWBs imposed early in the year (-1.0 °C versus +0.8°C in terms of the relative impact on the winter time Niño3 in Year 1). A secondary, slightly stronger warming develops by the end of Year 2 (Fig. 3c). Overall, the two years of the W+E set do not look too different from the CTL, as far as the ensemble means are concerned.

In the W+E+W set, we superimpose three more WWBs during Year 2 of the simulations, as observed in early 2015. As a result, the W+E+W set generates a strong EP El Niño by the end of Year 2 with the maximum SST anomaly reaching 4°C (Fig. 3d), which is in stark contrast to the moderate warm event in Year 2 of the W+E set (Fig. 3c). The ensemble-mean impact on the wintertime Niño3 of imposing these 2015 wind bursts is almost double the effect of the 2014 WWBs (+1.5°C versus +0.8°C). Furthermore, examining individual ensemble members we find that 29 out of 50 members in Year 2 of the W+E+W set develop extreme El Niño conditions (DJF Niño3 index exceeding 3°C), in contrast to only 7 in Year 1 of the W set. Consequently, the probability of occurrence of extreme events increases from 14% to nearly 60%. Our sensitivity tests and further analysis suggest that these differences are related to the preconditioning of the ocean-atmosphere system by the interplay of westerly and easterly wind bursts during Year 1, and not to different characteristics of WWBs (Hu and Fedorov 2017a).

Summary and outlook

The evolution of El Niño during 2014 and 2015 presents two different examples of the impact of intraseasonal wind bursts on El Niño development and diversity, including the occurrence of extreme events. In the early months of both 2014 and 2015, there were clear indications pointing to the possibility of a strong El Niño, including a heat-recharged equatorial ocean and a series of strong westerly wind bursts. However, in 2014 the warm event was stalled by an exceptionally strong easterly wind burst and did not exceed the formal threshold for El Niño. Nevertheless, the failed 2014 event preconditioned for El Niño development in the following year, and the equatorial warming in 2015 developed into an extreme event. These conclusions are supported by satellite-based and other observations, and by large-ensemble coupled simulations with superimposed wind bursts.

Thus, our results highlight the limits to El Niño predictability, including the predictability of extreme events with vast global impacts. Indeed, even a combination of a recharged ocean state and strong winter-spring westerly wind bursts does not guarantee the development of an extreme El Niño. Furthermore, these results suggest three directions for future research.

First, how initial ocean heat content anomalies are distributed along the equator matters, and so do the details of easterly and westerly wind bursts generated in the course of the year. Therefore, continuous and accurate in-situ observations in the ocean surface and subsurface are critical. Second, the dynamical mechanisms and potential predictability of westerly and easterly wind bursts deserves further investigations. Third, one should investigate the connection between intraseasonal, interannual and decadal timescales, suggested by similarities between the spatial patterns of easterly wind bursts and recent decadal trends in surface winds (Hu and Fedorov, 2016). The occurrence of a similar, but weaker EWB in June of 2015 (Fig. 2b), at almost the same time as in 2014, provides another clue.

Together, the failed El Niño of 2014 and the extreme El Niño of 2015 sustained prolonged warm conditions in the tropical Pacific during 2014-2016. This prolonged warming released a large amount of heat into the atmosphere which, together with the continuing global warming trend, made 2014, 2015 and 2016 the three consecutive warmest years in the instrumental temperature record to date (Hu and Fedorov, 2017b).

Acknowledgements

This research was supported by funding from NOAA (grant NA14OAR4310277) and NASA, including an Earth and Space Sciences Fellowship to S.H. We also acknowledge computational support from the Yale University Faculty of Arts and Sciences High Performance Computing facility and from the NSF / NCAR Yellowstone Supercomputing Center. We also thank Brian Dobbins for his help in setting up computational environment.

References

Capotondi A (2013) ENSO diversity in the NCAR CCSM4 climate model. J Geophys Res-Oceans, 118(10), 4755-4770.

Capotondi A et al. (2015) Understanding ENSO diversity. B Am Meteorol Soc, 96(6), 921-938.

Chelton DB, Schlax MG, Freilich MH, Milliff RF (2004) Satellite measurements reveal persistent small-scale features in ocean winds. Science 303 (5660):978-983

Chiodi AM, Harrison DE (2015). Equatorial Pacific Easterly Wind Surges and the Onset of La Niña Events. J Climate, 28(2), 776-792.

Deser C, Phillips AS, Tomas RA, Okumura YM, Alexander MA, Capotondi A, Scott JD, Kwon YO, Ohba M (2012) ENSO and Pacific Decadal Variability in the Community Climate System Model Version 4. J Climate 25 (8):2622-2651

ECMWF Spring El Niño Forecast (2014). http://www.ecmwf.int/en/forecasts/charts/seasonal/nino-plumes-public-charts-long-range-forecast. Accessd 18 March 2016

Fedorov AV, Harper SL, Philander SG, Winter B, Wittenberg A (2003) How predictable is El Nino? B Am Meteorol Soc 84 (7):911

Fedorov AV, Hu S, Lengaigne M, Guilyardi E (2015) The impact of westerly wind bursts and ocean initial state on

the development, and diversity of El Nino events. Clim Dynam 44 (5-6):1381-1401

Harrison DE, Vecchi GA (1997) Westerly wind events in the tropical Pacific, 1986-95. J Climate 10 (12):3131-3156

Harrison DE, Chiodi AM (2009) Pre- and Post-1997/98 Westerly Wind Events and Equatorial Pacific Cold Tongue Warming. J Climate 22 (3):568-581

Hartten LM (1996) Synoptic settings of westerly wind bursts. J Geophys Res-Atmos 101 (D12):16997-17019

Hu S, Fedorov AV, Lengaigne M, Guilyardi E (2014) The impact of westerly wind bursts on the diversity and predictability of El Nino events: An ocean energetics perspective. Geophys Res Lett 41 (13):4654-4663

Hu S, Fedorov AV (2016) Exceptionally strong easterly wind burst stalling El Nino of 2014. P Natl Acad Sci USA 113 (8):2005-2010

Hu S, Fedorov AV (2017a) The extreme El Niño of 2015-2016: the role of westerly and easterly wind bursts, and preconditioning by the failed 2014 event. Clim Dynam, in press, doi: 10.1007/s00382-017-3531-2.

Hu S, Fedorov AV (2017b) The extreme El Niño of 2015-2016 and the end of global warming hiatus. Submitted

Jin FF (1997) An equatorial ocean recharge paradigm for ENSO .1. Conceptual model. J Atmos Sci 54 (7):811-829.

Keen RA (1982) The Role of Cross-Equatorial Tropical Cyclone Pairs in the Southern Oscillation. Mon Weather Rev 110 (10):1405-1416.

Kleeman R, Moore AM (1997) A theory for the limitation of ENSO predictability due to stochastic atmospheric transients. J Atmos Sci 54(6):753–767.

Lengaigne M, Boulanger JP, Menkes C, Delecluse P, Slingo J (2004) Westerly wind events in the tropical pacific and their influence on the coupled ocean-atmosphere system: A review. Geoph Monog Series 147:49-69

Lengaigne M, Boulanger JP, Menkes C, Madec G, Delecluse P, Guilyardi E, Slingo J (2003) The March 1997 Westerly Wind Event and the onset of the 1997/98 El Nino: Understanding the role of the atmospheric response. J Climate 16 (20):3330-3343.

Levine, AFZ, McPhaden MJ (2016) How the July 2014 Easterly Wind Burst Gave the 2015-6 El Niño a Head Start. Geophys Res Lett 43(12): 6503-6510

McPhaden MJ (1999) Genesis and evolution of the 1997-98 El Nino. Science 283 (5404):950- 954.

McPhaden MJ (2015) Commentary: Playing Hide and Seek with El Nino. Nat Clim Change 5 (9):791-795

NASA Scientific News (2014). http://science.nasa.gov/science-news/science-at-nasa/2014/19may_elnino. Accessd 18 March 2016

NOAA Climate Prediction Center (2014). http://www.cpc.ncep.noaa.gov/products/expert_assessment/ENSO_DD_archive.shtml. Accessd 18 March 2016

Seiki A, Takayabu YN (2007) Westerly Wind Bursts and Their Relationship with Intraseasonal Variations and ENSO. Part II: Energetics over the Western and Central Pacific. Mon Wea Rev 135:3346-3361

Su J, Xiang B, Wang B, Li T (2014) Abrupt termination of the 2012 Pacific warming and its implication on ENSO prediction. Geophys Res Lett, 41(24), 9058-9064.

Tollefson J (2014) El Niño monitoring system in failure mode. Nature

Yu L, Weller RA, Liu WT (2003). Case analysis of a role of ENSO in regulating the generation of westerly wind bursts in the western equatorial Pacific. J Geophys Res-Oceans, 108(C4).

Shoreline integrated SLR impact prediction in Mombasa and Lamu islands in Kenya

Valentine K. Ochanda, Daniel K. Irurah

School of Architecture and Planning, University of the Witwatersrand, Private Bag 3, P.O. Wits, Johannesburg, South Africa

Contact e-mail: *valochanda@gmail.com*

Introduction

Sea Level rise (SLR) and the encroachment of the sea waters into adjacent built environment and primarily residences, has caused negative impacts in coastal areas around Asia and some parts of Africa much to the inconvenience and threat to the residents (Walker et al., 2007). Current projections of sea level rise associate with climate change scenarios (Richard et al., 2007; Stocker et al, 2013) show that current century minimum of 1.8m poses a challenge to coastal communities in Kenya and especially for Mombasa island. The threat of climate change and SLR will most likely place the longevity of the highly rated star hotels, and government investments in infrastructure and services at risk. The effects of accelerated SLR are already under way in some small island nations and island cities. These efforts, unfortunately, are a new concept for the developing world, understandably due to the pressures of financial implications of coastal areas as compared for example to the developed economies.

Coastal flooding, salt intrusion, and increased coastal tides have led to the relocation and forced migration of some local communities inland. Except for South Africa, few developed countries have implemented several strategies to counter effects of increased SLR, especially in port cities to protect the investments and the communities living in these areas. These include Durban, in South Africa, and portions of the Nile delta.

The world is working to reduce the world temperatures to a maximum of 2^{o}C increment, most of these efforts require countries to adopt cleaner options of energy, reduce the reliance on fossil fuels, besides reducing their carbon footprint through several other initiatives. African countries, on the other hand, are forcefully coming into the oil and gas exploration market with the identification, mining and the use of fossil fuels, which have been a privilege of the developed countries. In East Africa, Kenya, Uganda and Tanzania are developing and mining fossil fuels, more so to meet the growing energy demands in their economies which increase the exposure to climate change effects. Kenya and the neighboring eight African countries again are at an advanced stage of building the Lamu Port South Sudan Ethiopia Transport Corridor (LAPSSET), to facilitate the transfer of resources as well as generate a pipeline for oil refin¬ing and export within these countries. The results of this investment could undermine the global effort of reduction of global warming, and will paradoxically have further severe SLR related consequences for these same countries and their related port cities. Those will suffer most from the impacts of climate change, therefore increasing their vulnerability and exposure to climate change induced impacts (Hallegatte et al., 2013).

Africa is known to have a significant and growing coastal population, most located in some important coastal cities. Many of these coastal cities are also important ports for national and regional trade, imports and exports (UN-Habitat, 2012). In the event of a coastal storm or extreme event, the effects on the unprotected average population and developed assets in these coastal regions are much higher.

This study investigates the vulnerability and inundation levels for the island city of Mombasa and Lamu. Failed assessments and planning are putting the lives of communities, government investments and people under threat from accelerated SLR. The island city of Mombasa is a well-documented tourist destination with several world class star rated hotels that contribute to the national Gross Domestic Product (GDP) in Kenya. The city is an important port city for the east and central African region, making it crucial in the eastern and central Africa's business port. As well as being the city targeted under the Kenya 2030 development blueprint that intends to push Kenya's development agenda higher, one of the pillars that are foreseen to improve the development of Kenya is hinged on tourism which is mainly in Mombasa and Lamu coastal cities. Based on the primary objective of assessing the impacts of climate-change-induced SLR for Mombasa and Lamu island cities. This study finds that by the end of this century almost 50% of Mombasa island and almost 71% of Lamu island falls under threat of inundation from SLR enhanced storm surges of a one storm surge in 100 years.

Methods

Primary data sources

Required primary data for the analysis of the areas under threat in the two islands, included the initial spatial and land uses along the coastline that is within the low-elevation coastal zone (LECZ) mark. This area, and selected infrastructural point data for the assessment of sectors that is low lying, were supplemented by data from the mini-charrette process, where community members identified areas of their interests and households. The aim of primary data collection was to gather both quantitative and qualitative information to be used in the vulnerability analysis. Point data were collected using Garmin GPS, while the land use data were gathered from the ministry of planning to identify the sites of significant infrastructure and areas of interest for the mapping of the area and threatened critical zones.

Secondary data sources

Secondary data collection was for the analysis of the quantitative data on the mapping and the positioning of Mombasa and Lamu island about SLR. Data collected in this phase included a complete and detailed inventory of the critically exposed assets and resources (land, population, and urban infrastructure) along the cities for qualitative analysis with the inundation zones, projected for a current 1-in-100-year storm surge. Also sourced were spatially-disaggregated data sets from various public sources such as the National Aeronautics and Space Administration (NASA), the US Geological Survey (USGS), Dynamic Interactive Vulnerability Assessment (DIVA), the World Wildlife Fund (WWF) and Centre for International Earth Science Information Network (CIESIN).

The dataset from NASA was necessary for the provision of the digital elevation model (DEM) for Lamu Island as it was clearer (less cloud interference and therefore, needed fewer modifications), while the USGS data included the DEM for Mombasa Island. Other data included land uses, and subdivision data collected from Kenya Regional Centre for Mapping of Resources for Development (RCMRD) based in Nairobi, Kenya. These data allowed for the comparison of the global DEM versus the localy developed DEM. The importance of comparison of remotely sensed data was to allow for the best data with better resolution for the purpose of analysis. The comparison was, therefore, necessary to reduce the magnitude of errors that can result from widely disaggregated data.

The Kenya Meteorological Department (KMD) data were used to assess the temperature and rainfall pattern for the two counties. These data were coupled with the SLR recording stations managed by the Kenya Marine and Fisheries Institute (KEMFRI), and then used as a guide for the low and high tide ranges in the two counties as a key factor when assessing the impact of a storm surge in the coastal zones. Other secondary data (including the Physical Planning Act, the county planning and development documents necessary in the analysis of the desired area and infrastructure) were from the Ministry of Devolution and Planning, and the Ministry of Land Housing and Urban Development as well as their county equivalent within the respective governments.

A) Study area

Mombasa district is in the South-Eastern part of Kenya. It is the smallest of the seven areas in the Coastal counties, covering an area of 294.6 km^2. Lamu Island has a total land area of about 50 km^2. About 19 km^2 of the island is covered by a double row of sand dunes located along the entire length of the coastline and especially from Shella covering the southern coast. The Island is a UNESCO world heritage site.

B) Scenarios Used

The inundation analysis was based on two Representative Concentration Pathways (RCP) scenarios; this is RCP 8.5 (pessimistic scenario) and RCP 2.6 (optimistic scenario). RCP 8.5 is considered a high emission, high energy-intensive scenario as a result of high population growth and a lower rate of technology development (Detlef et al., 2011). RCP 2.6 (optimistic scenario) which is the lowest emission and radiative forcing scenario that represents a set of mitigation measures aimed at limiting the increase in global mean temperature to 2^{o}C.

The research sites were also selected based on the national economic blueprint (Kenya's Vision 2030), aimed at driving Kenya's economic status in an upward trajectory. Kenya's Vision 2030 is the government's development plan designed to make Kenya a global leader, in technology, and tourism destination. The main projects envisioned included the LAPSSET project and the redevelopment of Mombasa port, which currently represent areas that are important for both conservation and the country's economy through the tourism industry.

C) Analysis of inundation areas

SLR scenario modeling using GIS techniques and guided by the Intergovernmental Panel on Climate Change (IPCC) under two SLR scenarios of Regional Concentration Pathways (RCP 2.6 and RCP 8.5), was applied to estimate the spatial extent, population, and infrastructure under threat. Areas prone to flooding as a result of SLR were mapped for the city of Mombasa and the Island of Lamu. Secondary data helped in identifying the land use pattern's and delineate built areas lying within the LECZ. The analysis of the areas under threat of inundation dueto the SLR is based on the 1 in 100 years repeat cycle was done using the Global Mapper and ArcGIS software.

The surface maps including population and urban extent were analyzed using the "Spatial Analyst" extension of the ArcGIS 10.2 TM software of the ArcGIS tool which allowed for the integration of several aspects towards the

derivation of the most exposed portions. Using Equation 1, the global SLR rates were adjusted for the coastline of Mombasa and Lamu after considering, uplift and subsidence, and the chances of a storm surge at the coast. The adjusted SLR rates provided the data that was input into the Global Mapper for a flood simulation to see areas susceptible to inundation and increased flooding. The flood maps were then overlaid through an overlaying process to the land areas and land use maps, the two indicators (population and spatial/urban extent). The synthesized inundation and demographic data then inputted into the GIS system for the final production of the vulnerability maps.

D) Calculating Assets and population at risk

The demographic and economic data were important in the derivation of the population density maps in the cities, as well as the financial status of the two cities. Other data included in the analysis include the point data to identify areas of interest in Mombasa and Lamu Island. The population data were projected to 2016 and used in the analysis of the inundation levels from a baseline of 2009 for comparison purposes and the production of the maps. The digital elevation model (DEM) for both islands forms the primary basis of the analysis of inundation zones. DEM characterization was used to describe the height levels through the contours and populations distributed along the contours. The analysis was based on the zero (m) elevation of the ocean, from which the characterized areas of inundation were identified.

The population exposed indicator was done by delineating population living within the Low elevation areas. This was through the analysis of population grid for the Island and associated with each grid cell and land area. Estimates for the population was collected and analyzed from the 2009 census data sets. For the calculation of exposed assets, the exposed population was translated into the amount of capital per inhabitant. This capital per inhabitant is computed from the GDP per capita in each county and an estimate of the ratio of "produced capital" to GDP. The ratio of produced capital to GDP is calculated using the World Bank dataset published with the "Changing Wealth of the Nations" report. Earlier the rate was calculated at 5 times the GDP his was later scaled down to the ratio equalling to 2.8 and is applied to the two island (Hallegatte et al., 2013). The analysis was done on a 30-year cycle.

E) Vulnerability to future SLR analysis

Assessing vulnerability to future SLR was a three-setup approach. Firstly after generating the digital elevation map, the map was then subjected to inundation scenarios and alternative storm-surge (wave height) scenarios analysis. The scenario analysis was after applying the equation (1) by Nicholls et al. (2007) under the RCP2.6, and RCP8.5 identified for the years 2030, 2060 and 2090. Secondly, the county surface maps for each exposure indicator were then prepared (population and urban extent). Third, these surface indicator maps were overlaid with the inundation zone layer. The overlaying of the maps helped in the determinat-ion of the spatial exposure of each of the two indicators (Population, urban extent) under inundation threat for the Islands. The calculation of storm surges (extreme sea levels), followed the method outlined by Nicholls et al. (2007) and also applied by several researchers Dasgupta et al. (2011), Hallegatte et al. (2011) in global studies where calculations for Future Storm Surges (FSS) are as follows:

(Equation 1)

$$FSS = S100 + SLR + \frac{\{UPLIFT * 100yrs\} + SUB + (S100 * x)}{1000},$$

where

- FSS= S100=1-in-100 years surge height(m),
- SLR=sea-level rise (based on the IPCC results from the CIMP models),
- UPLIFT=continental uplift/subsidence in mm/year,
- SUB=0.5mm (applies to deltas only),
- x=0.1, or increase of 10% applied only in coastal areas currently prone to tsunamis and tropical cyclones.

F) Calculating assets exposed to SLR effects

For the analysis of exposed assets, values for 2015 National per capita GDP and the Purchasing Power Parity (PPP) were used. Analysis of exposed assets was done using the formulae shown in equation (2). The national per capita is preferred to the local per capita which would be translated regarding the coastal contribution to the country GDP (Hallegatte et al., 2013; Nicholls et al., 2007). In estimating the anticipated economic losses, a method suggested by Hallegatte et al. (2013) and Nicholls et al. (2007) is described as follows:

(Equation 2)

$$Ea = Ep * GDPpercapita(PPP) * 2.8$$

where,

- Ea= Exposed assets
- Ep= Exposed populations
  GDPpercapitappp= the nation's per capita Gross Domestic Product(GDP) purchasing power parity (PPP)

According to Nicholls et al. (2011), the factor of 2.8 translates to per capita GDP, i.e. the annual production of the economy divided by population, to the per capita value of assets. In their argument, annual investments usually represent, on average, about 25 percent of GDP. Assuming that per capita asset value in the city is growing by 3 percent a year, a rapid calculation suggests that the value of these assets is between 2.8 and five times per capita GDP Consistent with this estimate.

Results and Discussions

A) Mombasa and Lamu Island

Table I illustrates the impacts of SLR in the two coastal islands. Mombasa average annual mean sea level changes are averaged at 4.32m as collected from the SLR measuring stations. By applying the sea level rise anticipated globally and the local high water tide to ascertain the inundation scenarios, different results were achieved for the year 2030, 2060 and 2090. As shown in different figures different inundation levels were identified for each of the areas within the island.

Item	Scenario	Mombasa	Lamu
Area	8.5	8.0Km^2 equivalent to 44.9%	103.5Km^2 leading to 71.5% threatened
	2.6	4.2Km^2 threatend	81.1Km^2 under threat
Assets	8.5	US$ 14.5 Billion exposed	US$ 1.2 Bilion
	2.6	US$ 6.4 Bilion assets exposed	US$ 435 Milion
People	8.5	9.7 Million exposed	452 Thousands
	2.6	6.1 Million people exposed	248 Thousands exposed

Table 1: Population and island exposed to SLR inundation by the end of the century for Mombasa and Lamu islands

B) Scenario 1: Under the RCP 2.6

The inundation-prone areas under the optimistic scenario of RCP 2.6 by the year 2060. The island area of up to 1.4Km^2 in Mombasa and 28.3 km^2 of Lamu island is low lying and is susceptible to inundation. The areas under threat translate into 10% for Mombasa and 42.6% for Lamu land mass from accelerated SLR. By the year 2090 island area of up to 2.3 km^2 for Mombasa and 35 km^2 for Lamu is low lying and is susceptible to ocean disturbances. A total of 22% and 60.4% respectively of the area of the islands that will be rendered unusable by the end of the century due to the effects of accelerated SLR.

C) Scenario 2: Under the RCP 8.5

In Mombasa Island, the area of the island under threat translated to 2Km^2 equivalents to the 8.2 % of the land exposed. Inundation in 2060, this increases to approximately 2.6Km^2 for Mombasa a percentage of 20% adding up to 28.2% of the island area under threat from the effects of an extreme event. By 2090 the coastal regions prone to inundation is 3.1Km^2. The land mass under threat translates to a total of 44.9% of the land mass under threat from accelerated SLR In Mombasa island.

D) Population and infrastructure under threat for the two scenarios

Under RCP 2.6 scenario the simulation findings indicate that exposure level to the 1:100 storm surge for Mombasa County at 4m elevation falls between 434,000 and 2.5 million people and over US$ 6.2 billion in assets exposed by 2090. For Lamu, the exposure is between 38,000 and 481,000 people and over US$ 79.6 million. Under increased urbanization, vulnerability for both Mombasa and Lamu increases to over 25.64 million inhabitants, with infrastructure losses of approximately US$ 614.9 million. Currently, 48% to 52% of the infrastructure falls within the Low Elevation Coastal Zones (LECZ) thus highlighting its extreme vulnerability. The most vulnerable sectors at the coast that contribute to Kenya's Vision 2030 and long-term development are at threat to SLR-induced disturbances.

The spatial analysis in vulnerability assessment for Mombasa and Lamu islands showed advanced effects on both the community and critical infrastructure apart from displacing populations in these islands. Accelerated SLR can impact Kenya's GDP where essential infrastructures such as the Nyali Bridge, the Mombasa Port, and the LAPPSET project are rendered vulnerable, and thus mitigation and adaptation techniques need to be in place to protect threatened assets and communities. Meanwhile such knowledge should be nationally included in the planning and implementation of sustainability interventions for coastal cities such as Mombasa and Lamu whose residents and infrastructure are under threat from impacts of accelerated SLR.

Conclusion

As discussed, a 25% of the residents of Mombasa island are living below the 10m sea level rise area, with a healthy 11.6% living below the centuries 1.8m sea level rise inundation areas translating into a population of 133,456 as at 2009 and projected to be 417,289 individuals by 2030 and 1.426,537 individuals by 2090. This area under the inundation zone includes part of the Mombasa port and essential to the east and central Africa transport hub as well as several star rated hotels and homesteads around the islands and those adjacent to it.

The socio-economic damages expected to arise in the absence of coastal protection barriers is in the area of 9.1 billion USD, well over 8% of the Kenyan budget. In case of a projected annual increase of 2.8% in population around the area, a larger number of residents will beunder threat from increased flooding and inundation. The current century-old planning laws are not helping either. The 90m coastal high water mark that has not changed for a long time, in the face of a changing climate, will leave most of the public spaces around this island vulnerable and exploited for commercial purposes, therefore putting the lives of many residents, as well as visitors, at risk. The nexus between businesses interests, the environment and the use and access to the public space, associated with

current trends of SLR, is a difficult mixture that needs rapid discussion on adaptation and mitigation strategies.

Critical infrastructure for Mombasa and Lamu islands, especially the five and three star rated hotels, along with important port city development initiatives that serve central and eastern African countries, are faced with inundation threat as a result of accelerated SLR, under both the optimistic and the pessimistic scenarios. SLR impacts, especially on the services of Mombasa port as described, will affect not only the Kenyan economy but also the neighboring countries that use and depend on the coastal city for transport and the daily exchange of goods and services including tourists. The county and national government thus need to implement plans and programs to protect this critical infrastructure from the impacts of the advancing ocean and especially the slow and gradual SLR. As of now, neither Kenya's climate change strategy nor the Mombasa and Lamu county development strategy explicitly and systematically factor this challenge into their planning processes or programs. The adaptation and related financial management for all the climate-related disturbances are lumped in one disaster preparedness budget that still lacks systematic preparedness measures for the specific impacts related to threats such as SLR.

Given the findings of the study, it is recommended that for the sustainability and protection of these two islands which are important to the economy of Kenya, policies on adaptation, coastal planning, and protection with SLR are put into place. Action plans should be included in the county development plans that are meant to protect the environment and enhance the protection of critical infrastructure in these areas. Since the climate action plan for the country is salient on the matter of SLR and coastal protection, it's recommended that an addendum to the legislation for adaptation and mitigation of SLR impacts to the coastal cities of Mombasa and Lamu

Acknowledgement

Global change and sustainability research institute of Wit's is acknowledged for financial support. The communities living around Mombasa Island are also acknowledged for allowing us to have you during data collection. The results of this paper were obtained during my Ph.D. studies at the University of The Witwatersrand and are also in my thesis albeit with a different title. I would like to express sincere gratitude to my supervisors Daniel Irurah and Dr. Obudho Omondi whose guidance and support were crucial for the successful completion of this project.

References

Dasgupta, S., Laplante, B., Murray, S., and Wheeler, D. (2011). Exposure to developing countries to sea-level rise and storm surges. Climatic change, 106(4):567–579.

Detlef, P. van Vuuren, Edmonds, Jae, Kainuma, Mikiko, Riahi, Keywan, Thomson, Alison, Hibbard, Kathy, Hutt, C. George, Kram, Tom, and Krey, Volker (2011). The representative concentration pathways: an overview Springer. Climatic Change, 109(1):5–31.

Hallegatte, S., Green, C., Nicholls, R. J., and Corfee-Morlot, J. (2013). Future flood losses in the main coastal cities. Nature climate change, 3(9):802–806.

Hallegatte, S., Ranger, N., Mestre, O., Dumas, P., Corfee-Morlot, J., Herweijer, C., and Wood, R. M. (2011). Assessing climate change impacts, sea level rise and storm surge risk in port cities: A case study on Copenhagen. Climatic change, 104(1):113–137.

Nicholls, R., Hanson, S., Herweijer, C., Patmore, N., Hal¬legatte, S., Corfee, J., Chateau, J., and Wood, R. M. (2007). Ranking port cities with high exposure and vul¬nerability to climate extremes. The environment is working pa¬per, OECD.

Richard, A., Terje, B., Nathaniel, B., Zhenlin, C., Amnat, C., Pierre, F., Jonathan, G., Gabriele, H., Martin, H., Bruce, H., Brian, H., Fortunat, J., Jean, J., Vladimir, K., Ulrike, L., Martin, M., Taroh, M., Mario, M., Neville, N., Jonathan, O., Dahe, Q., Graciela, R., Venkatacha¬lam, R., Jiawen, R., Matilde, R., Susan, S., Richard, S., Stocker, T., Peter, S., Ronald, J., Penny, W., Richard, A. W., and David, W. (2007). Regional Climate Projec-tions, Climate Change 2007: The Physical Science Basis Contribution of Working Group I to the Fourth Assess¬ment Report of the Intergovernmental Panel on Climate Change. Technical Report 1, IPCC, Geneva, Switzerland, Geneva, Switzerland.

Stocker, T., Qin, D., Gian-Kasper, P., Alexander, L.V, Allen, S.K, Bindoff, N.L, Bron, F.M, Church,J.A, Cubasch, U., Emori,S., Forster,P., Friedlingstein, P., Gillett,N., Gregory,J.M, Hartmann, D.L, Jansen, E., Kirtma,B., Krishna, K., Lemke, P., and Marotzk, J. (2013). Technical Summary. In: Climate Change 2013: ThePhysical Science Basis. The Contribution of Working Group I to the Fifth Assessment Report of the Inter-governmental Panel on ClimateChange. Technical Report, Cambridge University Press, Cambridge, United Kingdom and New York, NY, USA.

UN-Habitat (2012). State of the world cities 2012/2013. Technical Report HS/080/12E, UN¬HABITAT, Nairobi, Kenya.

Walker, I. J., Barrie, J. V., Dolan, H., Gedalof, Z., Man-son, G., Smith, D., and Wolfe, S. A. (2007). Coastal vulnerability to climate change and sea-level rise northeast Graham Island, Haida Gwaii (Queen Charlotte Islands), British Columbia. Technical report, British Columbia.

Impact of Oceanic Front on the Tropospheric Climatic Trend Induced by Ozone Depletion

Fumiaki Ogawa[1,2], Nour-Eddine Omrani[1,2], Hisashi Nakamura[3,4], Kazuaki Nishii[5], Noel Keenlyside[1,2]

[1]Geophysical Institute, University of Bergen, Bergen, Norway

[2]Bjerknes Centre for Climate Research, Bergen, Norway

[3]Research Center for Advanced Science and Technology, University of Tokyo, Tokyo, Japan.

[4]Japan Agency for Marine-Earth Science and Technology, Yokohama, Japan

[5]Mie University, Mie, Japan

Contact e-mail: *fumiaki.ogawa@gfi.uib.no*

Introduction

The extratropical tropospheric circulation fluctuates with various temporal and spatial scales. The dominant mode of its low-frequency variability, such as intraseasonal through interannual scales, is manifested as meridional shifts of the westerly jet axis in the extratropics with a high degree of zonal symmetry. This variability is often referred to as the annular mode, which influences climatic conditions over extensive regions in the extratropics (Limpasuvan and Hartmann, 1999; Thompson and Wallace , 2000). The circulation anomalies associated with the annular mode in the Southern Hemisphere (the southern annular mode; SAM) are maintained mainly through feedback forcing generated with anomalous activity of synoptic-scale eddies (Lorenz and Hartmann, 2001).

Recent observations indicate that in the late 20th century the tropospheric westerly jet axis in the Southern Hemisphere shifted poleward, leading to positive trend in the SAM (Thompson et al., 2011). While the observed SAM trend in most of the seasons has been attributed, at least in part, to the anthropogenic increase in greenhouse gases (Shindell and Schmidt, 2004; Cai and Cowan, 2007), the summertime trend has been attributed mainly to the depletion of stratospheric ozone (the "ozone hole") over Antarctica (Thompson et al., 2011). The ozone depletion strengthened the springtime polar vortex in the Antarctic stratosphere, which was then transmitted downward into the surface as the summertime positive SAM trend. This trend was reflected in strengthening of the surface westerlies on the poleward side (~60°S) of their climatological axis (~50°S) and weakening on the equatorward side (~35°S). It has been pointed out that the downward transmission through the SAM requires feedback forcing from tropospheric synoptic-scale eddies (Yang et al., 2015). On the other hand, recent studies indicate that the SAM and tropospheric synoptic-scale eddies are largely influenced by the presence of a sharp meridional gradient in midlatitude SST (sea surface temperature) (oceanic front; Nakamura et al., 2008, Sampe et al., 2013, Ogawa et al., 2016). An oceanic front maintains the cross-frontal gradient of near-surface air temperature (i.e., baroclinicity), which acts to strengthen both baroclinic eddies and the eddy-driven westerly polar front jet (PFJ) climatologically (Nakamura et al., 2004, 2008; Ogawa et al., 2012). As the dominant low-frequency variability of the PFJ, the summertime SAM behavior shows sensitivity to the intensity of the oceanic front (Sampe et al., 2013). Therefore, the oceanic front may have an impact on the stratosphere-troposphere coupling of the SAM, and thereby its observed summertime trend linked to the ozone hole. Our study (Ogawa et al., 2015) has addressed how much the trend could have been controlled by the Southern Hemisphere oceanic front.

Assessment through aqua-planet AGCM experiments

Both the essential signature of the SAM and impacts of oceanic front on it can be addressed through aqua-planet AGCM (atmospheric general circulation model) experiments (e.g. Nakamura et al. 2008). The idealized setting eliminates stationary waves forced by topography and land-sea thermal contrasts, to mimic the conditions of the Southern Hemisphere (SH). The AGCM used in our study was ECHAM5 (Roeckner et al., 2003). Its horizontal resolution is T63 (equivalent to ~180km grid intervals), which resolves the sharp SST gradient across the SH oceanic frontal zones. The model has 39 vertical levels up to 0.01hPa. The lower boundary was set as zonally symmetric SST without any landmass (i.e. aqua-planet). Prescribed two different meridional SST profiles were based on the climatological-mean (1982-2007) monthly data provided by NOAA (OISST: Reynolds et al., 2007). One was taken from the South Indian Ocean at 60°E, where the warm Agulhas Return Current is confluent with the cool Antarctic Circumpolar Current and thus a

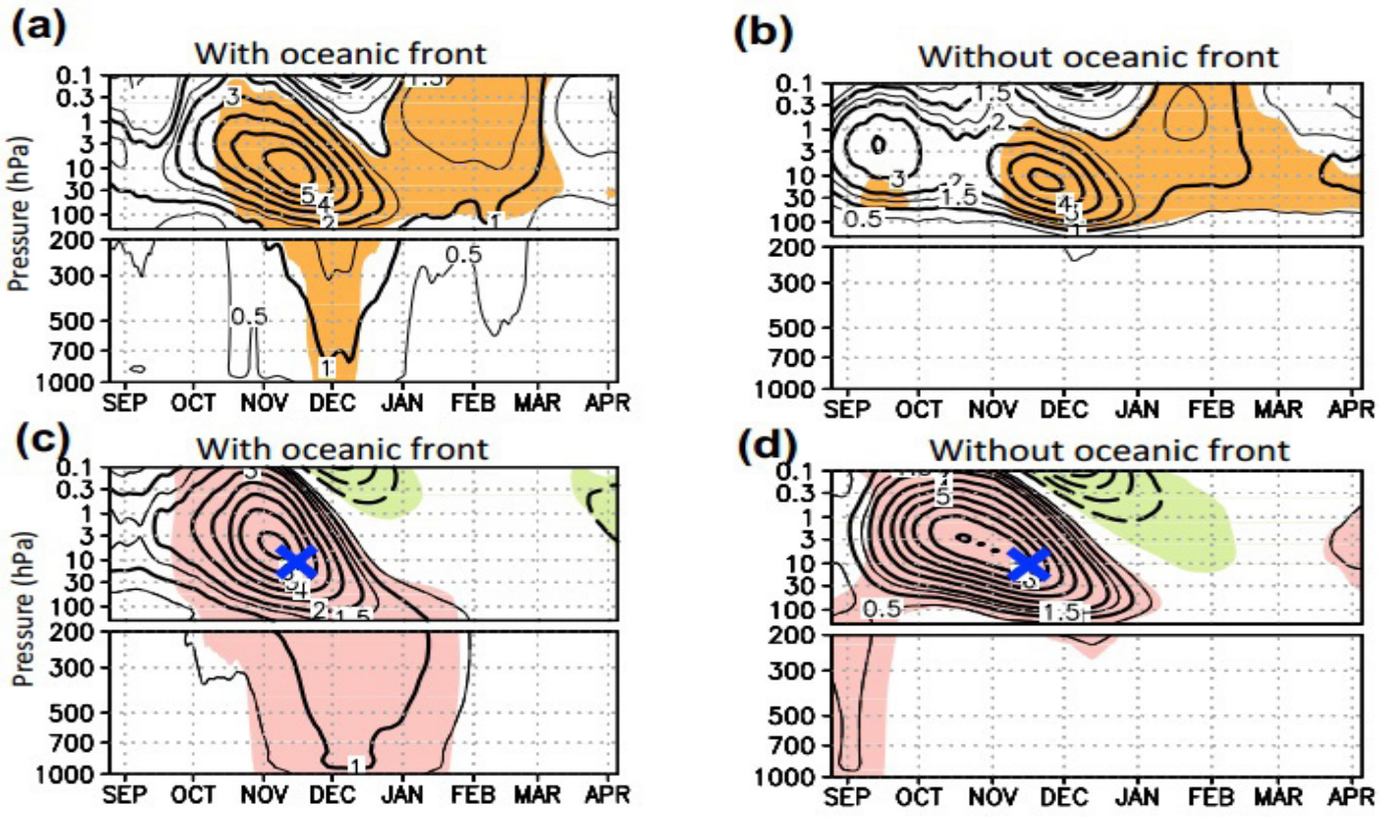

Figure 1: Time-height sections showing the seasonality of the simulated 31-day running-mean westerly response to the prescribed ozone depletion and anomalous westerlies associated with the stratospheric internal variability. **(a)-(b)** zonal-mean westerly response (ms^{-1}; contour) averaged between 45°S and 60°S for experiments **(a)** with and **(b)** without the oceanic front. Shading indicates the 95% statistical confidence based on the Student's t-test. **(c)-(d)** Typical 31-day running-mean anomalies in zonal-mean zonal wind (ms^{-1}) associated with year-to-year variability, regressed linearly on its PC1 time series at 13hPa (see text for details) in experiments **(c)** with the oceanic front and **(d)** without it. The reference pressure level (13hPa) and reference date (15th November) for the EOF analysis are marked by a cross in each panel. Shading indicates statistically significant signal at the 95% confidence level estimated from the correlation coefficient. After Ogawa et al., (2015).

prominent oceanic front is observed at 45°S throughout the year. In the other SST profile, the oceanic front has been smoothed by artificially warming the subpolar SST (Figs 1a-b in Ogawa et al., 2015). For each of the two seasonally varying SST profiles, simulations were conducted prescribing two different zonally symmetric ozone profiles. The ozone profiles were zonal averages of the JRA-25 reanalysis data (Onogi et al., 2007) averaged for the following two 3-year periods. One is from 1979 to 1981 that corresponds to the beginning of the ozone depletion, and the other from 1999 to 2001 when the ozone concentration reaches its minimum. The latter one shows less stratospheric ozone over the polar region in September and October (Fig 1c in Ogawa et al., 2015). For each of the two different SST profiles, response of the atmospheric circulation to the ozone depletion was defined as the climatological difference between the experiments with and without the ozone depletion. Four AGCM experiments as combinations of two prescribed SST and ozone profiles were conducted for 49 years after a 3-year spin up.

The simulated atmospheric circulation response to the ozone depletion (Fig 1a and 1b) shows the intensification of the springtime stratospheric westerlies regardless of the presence of the oceanic front. In contrast, a tropospheric response in late November through mid-December is found only in the presence of the oceanic front (Fig 1a). The simulated tropospheric response is consistent with the observed positive SAM trend (Thompson and Solomon, 2002). The westerly response is consistent with enhanced westerly acceleration driven by eddy forcing as estimated from the divergence of the Eliassen-Palm flux (Andrews et al., 1987). In the stratosphere, the ozone-induced strengthening of the stratospheric polar vortex was reinforced mainly by the planetary-scale waves regardless of the SST front. However, the positive SAM response simulated only in the presence of SST front was mainly associated with feedback forcing by the synoptic-scale waves in the troposphere (Ogawa et al., 2015). The importance of the planetary (synoptic) scale waves in the stratosphere (troposphere) simulated in the presence of oceanic front is consistent with the findings by Yang et al. (2015). This suggests that the activation of synoptic-scale eddies by near-surface baroclinicity associated with the midlatitude oceanic front can be crucial for the observed

transmission of the ozone-induced westerly trend from the stratosphere into the troposphere.

The results from the experiments further revealed that the appearance of the ozone-induced circulation trend is related to the stratosphere-troposphere SAM coupling. The leading mode of the year-to-year variability of the stratospheric polar vortex was identified as the 1st EOF mode of the zonally averaged westerly anomalies on 15th November, the day when the stratospheric westerly response to the ozone depletion is most significant. The contribution of the leading mode to the total variance was 80.1 (83.3) % when the oceanic front is present (absent). Since the meridional structure of the leading mode in our experiments is rather insensitive to the ozone profile, we combined the outputs from the two experiments with and without the ozone depletion under the same SST profiles for our EOF analysis. The significant tropospheric westerly anomalies associated with the dominant year-to-year stratospheric variability were simulated from late spring to midsummer in the presence of the oceanic front (Fig 1c), in good correspondence with the ozone-induced tropospheric climate trend (Fig 1a). In contrast, the tropospheric westerly anomaly associated with the stratospheric year-to-year variability become much less without the oceanic front (Fig 1d), consistent with the much reduced westerly response to the ozone depletion (Fig 1b). The striking difference in the vertical SAM coupling in our experiments can be understood from a viewpoint of the troposphere SAM signature. As discussed in previous studies (Nakamura et al., 2008; Sampe et al., 2013), the oceanic front strengthens the climatological mean eddy-driven westerlies in subpolar and mid-latitudes throughout the depth of the troposphere by activating synoptic-scale eddies. As the variability of the eddy-driven jet, the tropospheric SAM was simulated realistically only in the presence of the oceanic front in our experiment. Furthermore, the meridional structure of the simulated westerly response shows distinct similarity to the westerly anomalies associated with the simulated stratosphere-troposphere coupled year-to-year variability (Ogawa et al., 2015). The result suggests the importance of SAM representation in the troposphere for the vertical coupling.

Assessment through CMIP3/5 data sets

Our analysis of more sophisticated global climate model outputs (CMIP3/5 models: Meehl et al., 2007; Taylor et al., 2012) further revealed the potential of the midlatitude oceanic front to control the ozone-induced trend in the tropospheric westerlies in the summertime extratropical SH (Ogawa et al., 2015). It has already been shown that some of the CMIP3 models with realistic stratospheric ozone forcing can reproduce the SAM trend (Cai and Cowan, 2007; Son et al., 2009). In the present study, we focused on the 33 models showing the cooling trend (at the 99% confidence level) in the Antarctic stratosphere

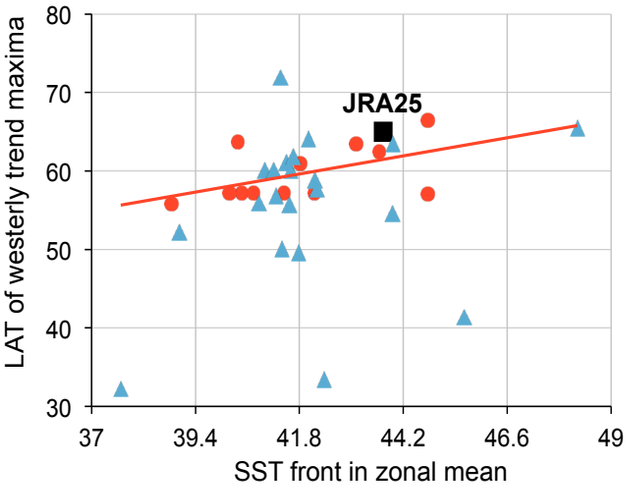

Figure 2: A scatter plot for the CMIP3/5 global climate models showing the relationship between summertime (Dec-Feb) climatological latitude of the midlatitude oceanic front (abscissa) and the peak latitude of an increasing trend in 850-hPa summertime zonal-mean westerlies (ordinate). The linear trend is evaluated at each latitudinal grid point for the period 1979/80-1998/99. A black square indicates those latitudes in the JRA25 data based on observations. Red line represents a linear regression among the 12 models (marked with red circles) that simulate midlatitude oceanic fronts stronger than in the JRA-25 data and stratospheric cooling trends over Antarctica significant at the 99% confidence level in spring and summer (Oct-Jan). Blue triangles signify those models in which the simulated stratospheric cooling trends are significant and midlatitude oceanic fronts are weaker than in JRA-25. After Ogawa et al., (2015).

during the last 20 years of the 20th century. The list of the model for the analysis is shown in the Tables 1 and 2. Fig 2 shows relationship between the climatological latitudes of oceanic fronts and the peak latitudes of the enhancing trends in 850-hPa zonal-mean westerlies both in austral summer. If all these 33 models are considered, those two latitudes indicate no obvious inter-model correlation (+0.25). However, the correlation greatly increases up to +0.51 with exceeding the 90% confidence level, if computed for the 12 models (red circles in Fig 2) which simulates cross-frontal SST gradient stronger than the climatological SST gradient in the JRA-25 reanalysis data (Onogi et al., 2007). This significant positive correlation is consistent with our AGCM experiments; a strong midlatitude oceanic front in a climate model acts to anchor the storm track and associated eddy-driven PFJ, determining the nodal latitude of SAM and thereby the meridional structure of its trend. For the remaining 21 models with weaker midlatitude SST gradients than in the reanalysis (blue triangles in Fig 2), in contrast, the inter-model correlation (+0.25) between these two latitudes loses its significance. These statistics suggest that an oceanic front can influence the ozone-induced SAM trend through its latitudinal position as well, if it has enough intensity. It is consistent with the previous findings that the latitude of an oceanic front can

influence the climatological latitudes of the storm track and the midlatitude eddy-driven PFJ if the frontal SST gradient is strong enough (Nakamura et al., 2008; Ogawa et al., 2012). While the SST gradient across the oceanic front can be strengthen associated with the SAM trend (Sen Gupta and England, 2006, 2007), the small change of SST gradient did not affect the selection of "stronger" and "weaker" SST gradient in our analysis. Our analysis on CMIP models (Ogawa et al., 2015) suggests that the latitudinal position of SST front can also impact on the internal tropospheric dynamics driving the observed stratosphere/troposphere coupling. One should be careful to regard individual models as independent samples because of their common origin (Masson and Knutti 2011). However, we do not consider our results biased significantly by this, as 8 from the 12 models can be considered as independent, and the results are consistent with our independent ECHAM model experiments discussed in chapter 2.

Conclusion

The above assessments (Ogawa et al., 2015) suggest the impact of an oceanic front on the ozone-induced downward stratosphere/troposphere coupling of the circulation anomalies and resulting tropospheric SAM-response. Firstly, our idealized aqua-planet AGCM experiments show that the presence of SST front is crucial for the ozone-induced climatic trend through enhancement of vertical coupling of SAM. The results support the role of synoptic and planetary-scale waves in the mechanisms proposed for the downward stratosphere/troposphere coupling (Yang et al., 2015). The realistic representation of midlatitude eddy-driven PFJ in the presence of oceanic front is found to be important for the tropospheric SAM response to the ozone depletion. Secondly, our analysis on the CMIP3/5 models shows that the latitude of a strong oceanic front may have influenced the reproduction of tropospheric SAM trend associated with the ozone depletion. It is therefore suggested that realistic representation of the oceanic front is a key for reliable future projection of the SH climate in a climate model under the forcing of the expected ozone recovery (Thompson et al., 2011; Son et al., 2008) and further global warming (Shindell and Schmidt, 2004; Cai and Cowan, 2007).

Acknowledgments

This was a collaborative study initiated under the Germany-Japan Bilateral Joint Research Project funded by the Japan Society for the Promotion of Science (JSPS) and Deutsche Forschungsgemeinschaft (DFG) (Co-PIs: S. Minobe and N. Keenlyside). The study is supported in part by the Japanese Ministry of Environment through the Environment Research and Technology Development Fund A-1201 and 2-1503 and by the Japanese Ministry of Education, Culture, Sports, Science and Technology (MEXT) through a Grant-in-Aid for Scientific Research in Innovative Areas 2205. F. Ogawa and N. Keenlyside acknowledge support from the NordForsk GREENICE project (Project 61841).

Model name	Ocean front	Atmos. grid	Institution(s)
CSIRO-Mk3.0	W	192x96	CSIRO Atmospheric Research
CSIRO-Mk3.5	S	192x96	
GFDL-CM2.1	W	144x90	US Dept. of Commerce / NOAA / Geophysical Fluid Dynamics Laboratory
GISS-ER	W	72x45	NASA / Goddard Institute for Space Studies
FGOALS-g1.0	W	128x60	LASG / Institute of Atmospheric Physics
INGV-SXG	W	320x160	Instituto Nazionale di Geofisica e Vulcanologia
MIROC3.2 (medres)	S	128x64	Center for Climate System Research (The University of Tokyo), National Institute for Environmental Studies, and Frontier Research Center for Global Change (JAMSTEC)
CCSM3	S	256x128	National Center for Atmospheric Research
PCM	S	128x64	
UKMO-HadCM3	S	96x73	Hadley Centre for Climate Prediction and Research / Met Office

Table 1: List of the 10 CMIP3 models used in the present study, which simulated a cooling trend in the stratosphere (100-hPa) over Antarctica from 1979/80 to 1998/99 in austral spring/summer (October–January) above the 99% confidence level. In the second column, "S" and "W" indicate that the SH oceanic front simulated in a particular model is stronger or weaker, respectively, compared to the SST field used for JRA-25. The third column denotes the numbers of grid points in longitude and latitude for atmospheric data provided. The fourth column denotes the institution(s) for each model. After Ogawa et al., (2015).

Model name	Ocean front	Atmos. grid		Institution(s)
ACCESS1-0	W	192x145		CSIRO (Commonwealth Scientific and Industrial Research Organisation, Australia), and BOM (Bureau of Meteorology, Australia)
BCC-CSM1.1	S	128x64		Beijing Climate Center, China Meteorological Administration
CanESM2	S	192x96		Canadian Centre for Climate Modelling and Analysis
CCSM4	S	288x192		National Center for Atmospheric Research
CESM1-FASTCHEM	S	288x192		National Science Foundation, Department of Energy, National Center for Atmospheric Research
CESM1-WACCM	W	144x96		
CMCC-CM	W	480x240		Centro Euro-Mediterraneo per I Cambiamenti Climatici
FGOALS-g2	W	128x60		LASG, Institute of Atmospheric Physics, Chinese Academy of Sciences
GFDL-CM3	W	144x90		Geophysical Fluid Dynamics Laboratory
GFDL-ESM2G	W	144x90		
GFDL-ESM2M	W	144x90		
GISS-E2-H	W	144x90		NASA Goddard Institute for Space Studies
GISS-E2-H-CC	W	144x90		
GISS-E2-R	W	144x90		
GISS-E2-R-CC	W	144x90		
INMCM4	W	180x120		Institute for Numerical Mathematics
IPSL-CM5A-LR	S	96x96		Institut Pierre-Simon Laplace
IPSL-CM5B-LR	W	96x96		Institut Pierre-Simon Laplace
MIROC4h	W	640x320		Atmosphere and Ocean Research Institute (The University of Tokyo), National Institute for Environmental Studies, and Japan Agency for Marine-Earth Science and Technology
MIROC5	W	256x128		
MIROC-ESM-CHEM	S	128x64		Japan Agency for Marine-Earth Science and Technology, Atmosphere and Ocean Research Institute (The University of Tokyo), and National Institute for Environmental Studies
MPI-ESM-P	W	192x96		Max Planck Institute for Meteorology (MPI-M)
NorESM1-ME	S	144x96		Norwegian Climate Centre

Table 2: As in Table S1 but for the 23 CMIP5 models. After Ogawa et al., (2015).

References

Andrews D. G., J. R. Holton, and C. B. Leovy, 1987: Middle Atmosphere Dynamics. Academic Press, San Diego.

Cai, W., and T. Cowan, 2007, Trends in Southern Hemisphere circulation in IPCC AR4 models over 1950–99: Ozone depletion versus greenhouse forcing, J. Clim., 20, 681–693, doi: 10.1175/JCLI4028.1.

Limpasuvan, V. and D. L. Hartmann, 1999, Eddies and annular modes of climate variability. Geo- phys. Res. Lett., 26, 3133–3136, doi:10.1029/1999GL010478.

Lorenz, D. J., and D. L. Hartmann, 2001: Eddy–zonal flow feedback in the Southern Hemisphere. J. Atmos. Sci., 58, 3312–3327, doi:10.1175/1520-0469(2001)058,3312:EZFFIT.2.0.CO;2.

Masson D. and R. Knutti, 2011, Climate model genealogy, Geophys. Res. Lett., 38, L08703, doi:10.1029/2011GL046864.

Meehl G. A. et al. , 2007, The WCRP CMIP3 multi-model dataset: A new era in climate change research, Bull. Am. Meteorol. Soc., 88, 1383–1394, doi: 10.1175/BAMS-88-9-1383.

Nakamura, H., T. Sampe, Y. Tanimoto, and A. Shimpo, 2004, Observed associations among storm tracks, jet streams and midlatitude oceanic fronts, AGU Geophys. Monogr., 147, 329–345, doi: 10.1029/147GM18.

Nakamura, H., T. Sampe, A. Goto, W. Ohfuchi, and S.-P. Xie, 2008, On the importance of midlatitude oceanic frontal zones for the mean state and dominant variability in the tropospheric circulation, Geophys. Res. Lett., 35, L15709, doi: 10.1029/2008GL034010.

Ogawa, F., H. Nakamura, K. Nishii, T. Miyasaka, and A. Kuwano-Yoshida, 2012, Dependence of the climatological axial latitudes of the tropospheric westerlies and storm tracks on the latitude of an extratropical oceanic front, Geophys. Res. Lett., 39, L05804, doi: 10.1029/2011GL049922.

Ogawa, F., N.-E. Omrani, K. Nishii, H. Nakamura, and N. Keenlyside, 2015: Ozone-induced climate change propped up by the Southern Hemisphere oceanic front. Geophys. Res. Lett., 42, 10055–10062, doi: 10.1002/2015GL066538.

Ogawa, F., H. Nakamura, K. Nishii, T. Miyasaka, and A. Kuwano-Yoshida, 2016: Importance of Mid-latitude Oceanic Frontal Zones for the Annular-Mode Variability: Inter-Basin Differences in the Southern Annular-Mode Signature. J. Clim., 29, 6179–6199, doi: 10.1175/JCLI-D-15-0885.1

Onogi, K. et al., 2007, The JRA-25 reanalysis, J. Meteorol. Soc. Jpn., 85, 369–432, doi: 10.2151/jmsj.85.369.

Reynolds, R. W. et al., 2007, Daily high-resolution-blended analyses for sea surface temperature. J. Clim., 20, 5473–5496, doi: 10.1175/2007JCLI1824.1.

Roeckner, E. et al., 2003, The atmospheric general circulation model ECHAM5. Part I: Model description. Max Planck Institute for Meteorology Rep., 349, 127 pp.

Sampe, T., H. Nakamura, and A. Goto, 2013, Potential influence of a midlatitude oceanic frontal zone on the annular variability in the extratropical atmosphere as revealed by aqua-planet experiments, J. Meteorol. Soc. Jpn., 91a, 243–267, doi: 10.2151/jmsj.2013-A09.

Sen Gupta, A., and M. H. England, 2006, Coupled ocean–atmosphere–ice response to variations in the Southern Annular Mode, J. Clim., 19, 4457–4486, doi: 10.1175/JCLI3843.1.

Sen Gupta, A., and M. H. England, 2007, Coupled ocean–atmosphere feedback in the Southern Annular Mode, J. Clim., 20, 3677-3692, doi: 10.1175/JCLI4200.1.

Shindell, D., and G. A. Schmidt, 2004, Southern Hemisphere climate response to ozone changes and greenhouse gas increases, Geophys. Res. Lett., 31, L18209, doi: 10.1029/2004GL020724.

Son, S.-W. et al., 2008 , The impact of stratospheric ozone recovery on the Southern Hemisphere westerly jet, Science, 320, 1486–1489, doi: 10.1126/science.1155939.

Son , S.-W., N. F. Tandon, L. M. Polvani, and D. W. Waugh, 2009, Ozone hole and Southern Hemisphere climate change, Geophys. Res. Lett., 36, L15705, doi:10.1175/JCLI-d-13-00698.

Taylor, K. E., R. J. Stouffer, and G. A. Meehl, 2012, An overview of CMIP5 and the experiment design, Bull. Am. Meteorol. Soc., 93, 485–498, doi: 10.1175/BAMS-d-11-00094.1.

Thompson, D. W. J., and J. M. Wallace, 2000, Annular modes in the extratropical circulation. Part I: Month-to-month variability, J. Clim., 13, 1000–1016.

Thompson, D. W. J., and S. Solomon, 2002, Interpretation of recent Southern Hemisphere climate change, Science, 296, 895–899, doi: 10.1126/science.1069270.

Thompson, D. W. J. et al., 2011, Signatures of the Antarctic ozone hole in Southern Hemisphere surface climate change, Nature Geoscience, 4, 741–749, doi: 10.1038/ngeo1296.

Yang, H., L. Sun, and G. Chen, 2015, Separating the mechanisms of transient responses to stratospheric ozone depletion-like cooling in an idealized atmospheric model, J. Atmos. Sci., 72, 763–773, doi:10.1175/JAS-D-13-0353.1.

Sub-decadal variability of the North Atlantic Oscillation in observations and the Kiel Climate Model

Annika Reintges[1], Mojib Latif[1,2], Wonsun Park[1]

[1]GEOMAR Helmholtz Centre for Ocean Research Kiel, Germany

[2]University of Kiel, Germany

Contact e-mail: *areintges@geomar.de*

Introduction

The North Atlantic Oscillation (NAO) is the most important mode of winter climate variability in the North Atlantic sector (Hurrell, 1995; Visbeck et al., 2001; Trigo et al., 2002; Hurrell et al., 2003; Hurrell and Deser, 2010). An index of the NAO can be defined as the sea level pressure (SLP) difference between the Azores high and the Icelandic low. A positive (negative) index reflects a strong (weak) SLP difference which is associated with a strong (weak) stormtrack over the mid-latitude North Atlantic. The NAO not only affects the storminess, but also causes temperature and precipitation anomalies over large parts of North America and Europe (Hurrel et al., 2003). Moreover, it has the potential to enhance the probability for the occurrence of weather extremes over these land areas (Scaife et al., 2008; Pinto et al., 2009).

Atmosphere-ocean interactions need to be considered when investigating the variability of the NAO. Interactions of the NAO with the ocean are suggested to work in both directions: on the one hand, the ocean responds to the NAO (Eden and Jung, 2001; Visbeck et al., 2003; Lohmann et al., 2009; Mecking et al., 2014; Delworth and Zeng, 2016; Delworth et al. 2016). On the other hand, the ocean is proposed to drive NAO variability (Rodwell et al., 1999; Watanabe and Kimoto, 1999; Mehta et al., 2000; Hoerling et al., 2001). The NAO index varies on a wide range of timescales (Hurrell et al., 2003). A significant peak in its power spectrum is found at a sub-decadal period (Czaja and Marshall, 2001; Fye et al., 2006). Other climate variables in the North Atlantic region, such as sea surface temperature (SST), also exhibit pronounced sub-decadal variability (Deser and Blackmon, 1993; Sutton and Allen, 1997; Czaja and Marshall, 2001; Saito et al., 2004; Fye et al., 2006; Álvarez-García et al., 2008). This article summarizes the findings of Reintges et al. (2016, hereafter R16). They show that there is statistically significant sub-decadal Atlantic sector climate variability in both instrumental observations and in the Kiel Climate Model (KCM; Park et al., 2009), a global coupled atmosphere-ocean-sea ice model.

Sub-decadal variability associated with the NAO

R16 analyzed the station-based wintertime (December-March, DJFM) NAO index as well as a 700 years long control integration of the KCM. The spatial structure and variability of the NAO simulated by the KCM are consistent with observations and that in other general circulation models (Semenov et al., 2008). The observed NAO index covers the period 1864-2014 (https://climatedataguide.ucar.edu/climate-data/hurrell-north-atlantic-oscillation-nao-index-station-based).

Sub-decadal modes were derived through Singular Spectrum Analysis (SSA; Vautard and Ghil, 1989). In the observed NAO index, a sub-decadal mode with a period of about 8 years explaining 18% of the total variance is found (Fig. 4a and 4b in R16). In the KCM, the sub-decadal NAO mode has a period of about 9 years and explains 4% of the total variance (Fig. 5a and 5b in R16). The relatively small explained variance in the KCM is due to the longer window that was chosen. The SLP and SST anomaly patterns (Fig. 6 and 7 in R16, respectively) associated with the sub-decadal NAO mode derived from data and the KCM are similar. The SST anomaly pattern depicts a dipolar structure, with one center in the subpolar North Atlantic and the other southwest of that off the coast of North America. This pattern is associated with an increased (decreased) meridional SST gradient during the positive (negative) NAO phase.

One example illustrating the strong link between the sub-decadal NAO variability and land surface air temperatures is shown in Fig 1. The independently derived sub-decadal SSA modes of the NAO index (DJFM) and of the surface air temperature (SAT) anomaly (DJFM) from Hamburg-Fuhlsbüttel, Germany (http://www.dwd.de/EN/Home/home_node.html) are highly correlated at r = 0.88 (for the period 1891-2014). The sub-decadal mode of the SATs in Hamburg explains as much as 25 % of the total variance. This stresses the importance of the NAO for the winter climate over Europe and the potential role of the sub-decadal NAO mode for multiyear predictability.

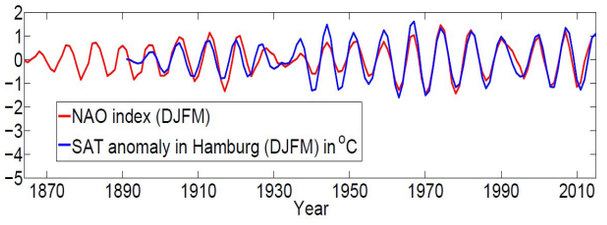

Figure 1: The sub-decadal winter (DJFM) modes of the station-based North Atlantic Oscillation (NAO) index and of the surface air temperature (SAT) anomaly in Hamburg-Fuhlsbüttel (Germany) derived through Singular Spectrum Analysis (SSA).

The origin of the sub-decadal NAO mode in the KCM

The mechanism behind the sub-decadal mode in the KCM is summarized in the following (for further details and additional Figs see R16). The main result is that atmosphere-ocean interactions are crucial to the sub-decadal mode. There is a positive feedback raising the sub-decadal mode to a significant level, as suggested in the hybrid coupled model study by Eden and Greatbatch (2003). The persistent dipolar SST anomaly pattern positively feeds back on the NAO. This positive feedback was demonstrated through two experiments with the atmospheric component of the KCM. A control simulation was forced by the SST climatology. The other experiment was forced by the dipolar SST anomaly pattern (associated with the positive phase of the sub-decadal NAO mode) superimposed on the SST climatology. The resulting SLP differences between the two experiments correspond to a positive NAO index, illustrating the positive feedback (Supplementary Fig. S4b in R16). There also is a delayed negative feedback which is responsible for the phase change of the sub-decadal mode. Both feedbacks become apparent in the lag-regression patterns associated with the sub-decadal NAO mode and are sketched in Fig 2. The displayed anomalies are shown for the lags -4 years (corresponding to the negative NAO phase), -2 years (the transition phase), and 0 years (the positive NAO phase).

Let us start with the negative phase of the sub-decadal NAO mode, which corresponds to a lag of –4 years. Accordingly, the SLP gradient between the subpolar low and the subtropical high is reduced. This is associated with weaker mid-latitude westerlies and causes anomalies in the net surface heat flux (positive values correspond to a heat flux anomaly into the ocean). The oceanic heat loss is reduced at around 55° N and enhanced over the Gulf Stream region off the American coast. The resulting SST change is dipolar with positive anomalies north of 45° N and negative anomalies to the southwest.

The latter, centered at about 40°N, strengthens at lag -2 years, which corresponds to the transition phase of the sub-decadal NAO mode. At this stage, the NAO index is weak and does not drive heat flux anomalies that could explain the intensification of the cold SST anomaly. In fact, the heat flux anomalies would tend to damp it (not shown). The extended cooling in this area is due to ocean dynamics. In agreement with the findings of Marshall et al. (2001), the zero-line of the wind stress curl moves southward during a negative NAO phase. The cyclonic anomaly in the barotropic streamfunction that develops between the subpolar and the subtropical gyre corresponds to a southward extension of the subpolar gyre. Because of its position between the average subpolar and subtropical gyre this anomaly is called the 'inter-gyre gyre'. The region at about 40°N, which features the elongated cooling during the transition phase (lag -2 years), is now more affected by the subpolar gyre thereby causing the cooling at 40°N through reduced heat advection.

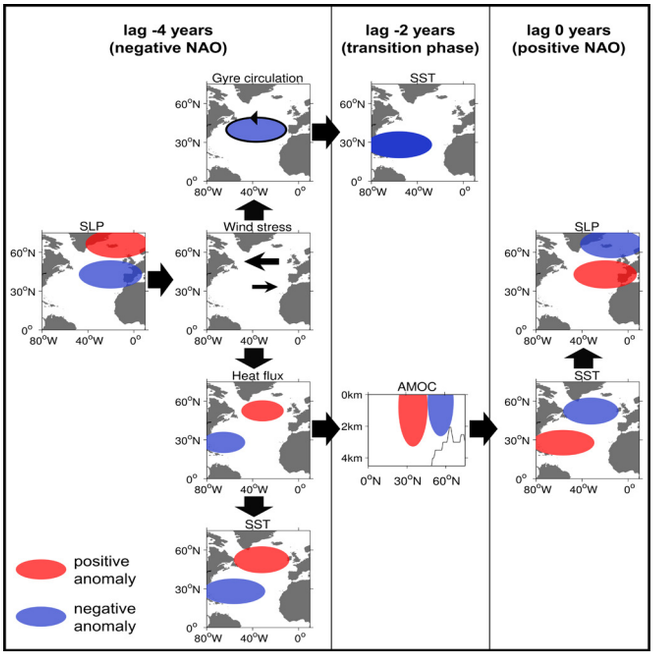

Figure 2: Schematic diagram of the two feedback mechanisms illustrated through idealized lag-regression patterns associated with the sub-decadal NAO mode based on results from the Kiel Climate Model (KCM). The gyre circulation is based on the barotropic streamfunction and positive heat flux values indicate a heat gain for the ocean.

The delayed negative feedback involves the Atlantic Meridional Overturning Circulation (AMOC) which responds to the dipolar heat flux anomalies. There is a delay in the response of the AMOC and its influence is seen at lag -2 years. A dipolar meridional overturning streamfunction anomaly pattern, consisting of two deep-reaching cells with a node at about 45°N, has developed. The associated anomalous meridional heat transport in the surface layer causes SST cooling north of 45°N and SST warming south of it (lag 0 years). This reverses the SST tendencies and initiates the phase change towards a

positive NAO index at lag 0 years. The delay in the AMOC and meridional heat transport response to the negative NAO-related heat flux forcing is important in setting the period of about 9 years. The close link between the NAO and the AMOC was further illustrated through SSA applied to an AMOC index defined as the maximum streamfunction at 30°N. The SSA of the AMOC index also revealed a sub-decadal mode with a period of 9 years explaining 8 % of the total variance (Fig. 5 in R16). The reconstructed sub-decadal time series of the NAO index and the AMOC index, which were derived independently, exhibit a correlation coefficient of r = 0.74, with the AMOC index leading the NAO index by 1 year. This emphasizes the important role that the AMOC plays in the generation of the sub-decadal NAO mode.

To verify the role of the AMOC for the sub-decadal NAO variability, the atmospheric component of the KCM was coupled to a slab-ocean model without active ocean dynamics. The power spectrum of the NAO index from the slab model experiment (cf. Fig. 2b and 2c in R16) does not depict a significant sub-decadal peak. This result is not sensitive to varying window type and length used for the computation of the power spectrum, and suggests that the ocean dynamics are essential to generate the sub-decadal NAO mode.

The SLP and SST anomaly patterns linked to the sub-decadal NAO variability in the KCM agree with those derived from observations. Finally, the observed AMOC index from the RAPID array at 26.5° N (http://www.rapid.ac.uk/rapidmoc/) (Smeed et al., 2015) was investigated. It also exhibits a sub-decadal variability (Cunningham et al., 2013; Bryden et al., 2014) that seems to lead the NAO index by 1 to 2 years (Fig. 3b in R16). This is consistent with the model results. However, the AMOC record from RAPID is much too short and not suitable for drawing conclusions about the origin of the sub-decadal variations. Thus, a continuation and possible extension of deep ocean observations will be useful to validate the model results and to enhance prediction of the NAO.

In summary, the enhanced variability in the North Atlantic at the sub-decadal timescale is suggested to originate from dynamical atmosphere-ocean interactions. This is supported by the following three major results obtained from the KCM: First, we find SSA modes with a period of 9 years in different atmospheric and oceanic quantities. Second, pronounced sub-decadal NAO variability is not simulated in a slab-ocean model version of the KCM, stressing that ocean dynamics are essential to create this mode. Third, when forcing the atmospheric component of the KCM with the SST anomalies associated with the positive phase of the sub-decadal NAO mode, the simulated SLP anomalies depict a positive NAO phase, demonstrating the existence of a positive feedback.

References

Álvarez-García, F., M. Latif, and A. Biastoch, 2008: On Multidecadal and Quasi-Decadal North Atlantic Variability. Journal of Climate, 21, 3433–3452.

Bryden, H.L., B.A. King, G.D. McCarthy, and E.L. McDonagh, 2014: Impact of a 30% reduction in Atlantic meridional overturning during 2009-2010. Ocean Science, 10, 683–691.

Czaja, A., and J. Marshall, 2001: Observations of atmosphere-ocean coupling in the North Atlantic. Quarterly Journal of the Royal Meteorological Society, 127, 1893–1916.

Cunningham, S.A., C.D. Roberts, E. Frajka-Williams, W.E. Johns, W. Hobbs, M.D. Palmer, ... and G. McCarthy, 2013: Atlantic Meridional Overturning Circulation slowdown cooled the subtropical ocean. Geophysical Research Letters, 40, 6202–6207.

Delworth, T.L., and F. Zeng, 2016: The impact of the North Atlantic Oscillation on climate through its influence on the Atlantic meridional overturning circulation. Journal of Climate, 29, 941–962.

Delworth, T.L., F. Zeng, G.A. Vecchi, X. Yang, L. Zhang, and R. Zhang, 2016: The North Atlantic Oscillation as a driver of rapid climate change in the Northern Hemisphere. Nature Geoscience, 9, 509–512.

Deser, C., and M. Blackmon, 1993: Surface climate variations over the North Atlantic Ocean during winter: 1900-1989. Journal of Climate, 6, 1743–1753.

Eden, C., and R. Greatbatch, 2003: A damped decadal oscillation in the North Atlantic climate system. Journal of Climate, 16, 4043–4060.

Eden, C., and T. Jung, 2001: North Atlantic interdecadal variability: Oceanic response to the North Atlantic oscillation (1865-1997). Journal of Climate, 14, 676–691.

Fye, F.K., D.W. Stahle, E.R. Cook, and M.K. Cleaveland, 2006: NAO influence on sub-decadal moisture variability over central North America. Geophysical Research Letters, 33, 1–5.

Hoerling, M.P., J.W. Hurrell, and T. Xu, 2001: Tropical Origins for Recent North Atlantic Climate Change. Science, 292, 90-92.

Hurrell, J.W., 1995: Decadal Trends in the North Atlantic Oscillation: Regional Temperatures and Precipitation. Science, 269, 676–9.

Hurrell, J.W., and C. Deser, 2010: North Atlantic climate

variability: The role of the North Atlantic Oscillation. Journal of Marine Systems, 79, 231–244.

Hurrell J.W., Y. Kushnir, G. Ottersen, and M. Visbeck, 2003: An overview of the North Atlantic Oscillation. In: Hurrell J.W., Y. Kushnir, G. Ottersen, and M. Visbeck (eds) The North Atlantic Oscillation: Climate significance and environmental impact. American Geophysical Union, Washington.

Lohmann, K., H. Drange, and M. Bentsen, 2009: Response of the North Atlantic subpolar gyre to persistent North Atlantic oscillation like forcing. Climate Dynamics, 32, 273–285.

Marshall, J., H. Johnson, and J. Goodman, 2001: A Study of the Interaction of the North Atlantic Oscillation with Ocean Circulation. Journal of Climate, 14, 1399-1421.

Mecking, J.V., N.S. Keenlyside, and R.J. Greatbatch, 2014: Stochastically-forced multidecadal variability in the North Atlantic: A model study. Climate Dynamics, 43, 271–288.

Mehta, V.M., M.J. Suarez, J.V. Manganello, and T.L. Delworth, 2000: Oceanic influence on the North Atlantic Oscillation and associated Northern Hemisphere climate variations: 1959-1993. Geophysical Research Letters, 27, 121–124.

Park, W., N.S. Keenlyside, M. Latif, A. Ströh, R. Redler, E. Roeckner, and G. Madec, 2009: Tropical Pacific Climate and Its Response to Global Warming in the Kiel Climate Model. Journal of Climate, 22, 71–92.

Pinto, J.G., S. Zacharias, A.H. Fink, G.C. Leckebusch, and U. Ulbrich, 2009: Factors contributing to the development of extreme North Atlantic cyclones and their relationship with the NAO. Climate Dynamics, 32, 711–737.

Reintges, A., M. Latif, and W. Park, 2016: Sub-Decadal North Atlantic Oscillation variability in observations and the Kiel Climate Model. Climate Dynamics, doi:10.1007/s00382-016-3279-0.

Rodwell, M. J., Rowell, D. P., & Folland, C. K. (1999). Oceanic forcing of the wintertime North Atlantic Oscillation and European climate. Nature, 398, 320–323.

Saito, K., T. Yasunari, and J. Cohen, 2004: Changes in the sub-decadal covariability between Northern Hemisphere snow cover and the general circulation of the atmosphere. International Journal of Climatology, 24, 33–44.

Scaife, A.A., C.K. Folland, L.V. Alexander, A. Moberg, and J.R. Knight, 2008: European climate extremes and the North Atlantic Oscillation. Journal of Climate, 21, 72–83.

Semenov, V.A., M. Latif, J.H. Jungclaus, and W. Park, 2008: Is the observed NAO variability during the instrumental record unusual? Geophysical Research Letters, 35, L11701.

Smeed, D., G. McCarthy, D. Rayner, B.I. Moat, W.E. Johns, M.O. Baringer, and C.S. Meinen, 2015: Atlantic meridional overturning circulation observed by the RAPID-MOCHA-WBTS (RAPID-Meridional Overturning Circulation and Heatflux Array-Western Boundary Time Series) array at 26N from 2004 to 2014. British Oceanographic Data Centre—Natural Environment Research Council, UK.

Sutton, R.T., and M.R. Allen, 1997: Decadal Predictability of North Atlantic sea surface temperature and climate. Nature, 388, 563–567.

Trigo, R.M., T.J. Osborn, and J.M. Corte-Real, 2002: The North Atlantic Oscillation influence on Europe: Climate impacts and associated physical mechanisms. Climate Research, 20, 9–17.

Vautard, R., and M. Ghil, 1989: Singular spectrum analysis in nonlinear dynamics, with applications to paleoclimatic time series. Physica D, 35, 395–424.

Visbeck, M., J.W. Hurrel, L. Polvani, H.M. Cullen, 2001: The North Atlantic Oscillation: past, present, and future. Proceedings of the National Academy of Sciences of the United States of America, 98, 12876–12877.

Visbeck, M., E. Chassignet, R. Curry, T. Delworth, R. Dickson, and G. Krahmann, 2003: The ocean's response to North Atlantic Oscillation variability. In: Hurrell J.W., Y. Kushnir, G. Ottersen, and M. Visbeck (eds) The North Atlantic Oscillation: Climate significance and environmental impact. American Geophysical Union, Washington.

Watanabe, M., and M. Kimoto, 1999: Tropical-extratropical connection in the Atlantic atmosphere-ocean variability. Geophysical Research Letters, 26, 2247–2250.

Isentropic Meridional Mass Circulation in Extratropics and Cold Air Outbreaks in Northern Hemisphere Winter

Yueyue Yu[1], Ming Cai[2], Rongcai Ren[3], Huug M. Van Den Dool[4]

[1]Geophysical Fluid Dynamics Institute, Florida State University, Tallahassee, Florida

[2]Department of Earth, Ocean and Atmospheric Science, Florida State University, Tallahassee, Florida

[3]LASG, Institute of Atmospheric Physics, Chinese Academy of Sciences, Beijing, China

[4]NOAA/NCEP/NWS/Climate Prediction Center, College Park, Maryland

Contact e-mail: *yyu4@fsu.edu*

Introduction

Cold air outbreak events in mid-latitudes in the northern hemisphere in winter (CAOs) are potentially severe weather phenomena that have a serious influence on residents, agriculture, and transportation. Various anomalous synoptic- and planetary-scale patterns have been identified as precursor signals for CAOs over different regions. Positive sea level pressure anomalies along the Alaska–Yukon border and the coexistence of a ridge over the Arctic (Walsh et al., 2001) and a trough over the Great Lakes region (Konrad, 1996) are good precursors for CAOs over North America. The intensification and expansion of the Siberian high (Ding, 1990) are closely related with CAOs over East Asia. The negative phase of the North Atlantic Oscillation (NAO) (Cellitti et al., 2006) and the Arctic Oscillation (AO) or the tropospheric northern annular mode (NAM) (Thompson and Wallace, 2001) tends to be followed by cold temperature over mid-latitudes. Besides the extratropics, the stratospheric circulation anomalies such as stratospheric polar vortex oscillation (Baldwin and Dunkerton, 1999; Thompson et al., 2002; Cai, 2003) and the equatorial quasi-biannual oscillation (QBO) and tropical forcing such as ENSO (Thompson et al., 2002) are also promising indicators for winter CAOs.

Johnson (1989) and some following works (e.g., Cai and Shin, 2014) established a hemisphere-wide single cell model for meridional mass circulation, connecting the tropical heating source to the polar heating sink via a poleward warm air branch in the upper troposphere and an equatorward cold branch in the lower troposphere. CAOs can be directly related to an anomalous strong meridional mass circulation, with more cold air discharged from the northern polar region into the lower latitudes within the cold air branch in lower isentropic layers (Iwasaki and Mochizuki, 2012). The strengthening of the cold air branch is further connected with the strengthening of the warm air branch in the upper atmosphere and is driven by the amplification of large-scale waves in the mid-latitudes. Therefore, the meridional mass circulation perspective not only allows us to capture the preferred routes of CAOs directly but also can help us to investigate the precursory changes in various circulation fields for cold air outbreaks.

Data and Analysis Procedures

The data fields used in this study include temperature, pressure, and meridional wind at the surface, and the three-dimensional air temperature, geopotential height, and meridional wind, which are derived from the daily ERA-Interim data for the 32 winters from 1 November 1979 to 28 February 2011 (ECMWF, 2012; Simmons et al., 2006; Dee et al., 2011). The data fields are on 1.5° latitude×1.5° longitude grids and on 37 pressure levels spanning from 1000 to1 hPa.

We have followed Yu et al. (2014) and Yu et al. (2015a, b, c) and calculated variables associated with isentropic meridional mass circulation including air mass (M), mass tendency, and meridional and vertical mass fluxes in isentropic layers (MF and VF) from daily fields. The zonally integrated field is then calculated and denoted using angle brackets. For example, the zonally integrated meridional mass flux is denoted as <MF>. Positive values of <MF> correspond to poleward mass transport across a given latitude within the two adjacent isentropic surfaces and negative values correspond to equatorward transport. On average, negative values of <MF> mainly appear in the lower troposphere within the equatorward cold air branch of the meridional mass circulation, while positive values mainly appear in upper layers within the poleward warm air branch. On the other hand, positive/negative values of zonally integrated VF, denoted as <VF>, correspond to upward/downward mass fluxes across the isentropic surface because of diabatic heating/cooling. Positive values of <VF> are observed mainly in the tropics and the surface layer in the extratropics; whereas negative

values are found outside of the tropics above the surface layer. After applying optimization methods as described in Yu et al. (2014), mass conservation at each latitude band and isentropic layer can be generally achieved such that the net mass change due to the convergence of <MF> and <VF> is equal to the daily tendency of the <M>.

Two sets of indices are derived in this study. In order to measure the intensity of the poleward warm air branch of meridional mass circulation at 60°N, we derived the WB60N index as the vertical sum of <MF> above the critical isentropic level that separates the warm and cold air branches at 60°N. Note that the critical isentropic level varies day to day within the range between 270 K and 290 K. We also derived the CB60N index as the sum of <MF> below the critical isentropic level to measure the intensity of the equatorward cold air branch crossing 60°N. In addition, we followed Cai (2003) and calculated warm and cold temperature area indices, defined as the spatial extent or the percentage of area occupied by warm or cold surface air temperature anomalies that exceed the 0.5 local standard deviation in a given region. Two regions are used in this study: mid-latitudes (25–60°N) and high latitudes (60–90°N).

Results

A) The relation of WB60N with temperature area indices

It is found that stronger warm air mass transport into the upper polar atmosphere is always accompanied by stronger equatorward advancement of cold air in the lower troposphere, and vice versa. Such highly in-phase variations of WB60N and CB60N are because they are simultaneous results of westward tilted waves in the extratropics, according to Johnson (1989). Lagged correlation and composite analyses of WB60N index and temperature area indices, together with the probability distribution function of temperature area indices associated with different intensity of WB60N, show that in the week after the peak dates of weaker meridional mass circulation events, the mid-latitudes tend to be anomalous warm while the high latitudes tend to be anomalous cold. Conversely, in the week after the peak dates of stronger WB60N synchronized with stronger equatorward discharge of cold polar air in the lower troposphere, massive CAOs tend to occur in mid-latitudes accompanied with anomalous warmth in high latitudes.

Such a relationship between the meridional mass circulation at 60°N and the general cold or warmth in mid- and high- latitudes is attributed to the redistribution of cold and warm air mass dominated by the adiabatic rather than the diabatic mass transport across the polar circle. During the strong meridional mass circulation events featured by a strengthening of the poleward mass transport in the upper troposphere within the warm air branch and the equatorward mass transport below within the cold air branch for example, in upper layers, the air mass transported adiabatically from mid-latitudes to the polar region overwhelms that transported downward across isentropic surfaces because of diabatic cooling, leading to a net increase of warm air mass in the high latitudes. In the lower layers, the air mass transported out of the polar region by the strengthened equatorward cold air branch dominates over that transported in from the upper layers because of diabatic cooling, resulting in a net decrease of cold air mass in the high latitudes. The opposite situation is found in the mid-latitudes. Therefore, it is the anomalous adiabatic mass transport across the polar circle that lead to the anomalous increase/decrease of cold air mass and decrease of surface temperature in the mid-/high- latitudes and the below-normal/above-normal temperatures in the mid-/high- latitudes during the following week.

B) The relation of WB60N with the spatial pattern of CAOs

The robust relation between the circulation and temperature area indices is further substantiated from the dominant geographical patterns of surface air temperature anomalies. There are two dominant geographical patterns of CAOs during the cold air discharge period (or 1 week after a stronger mass

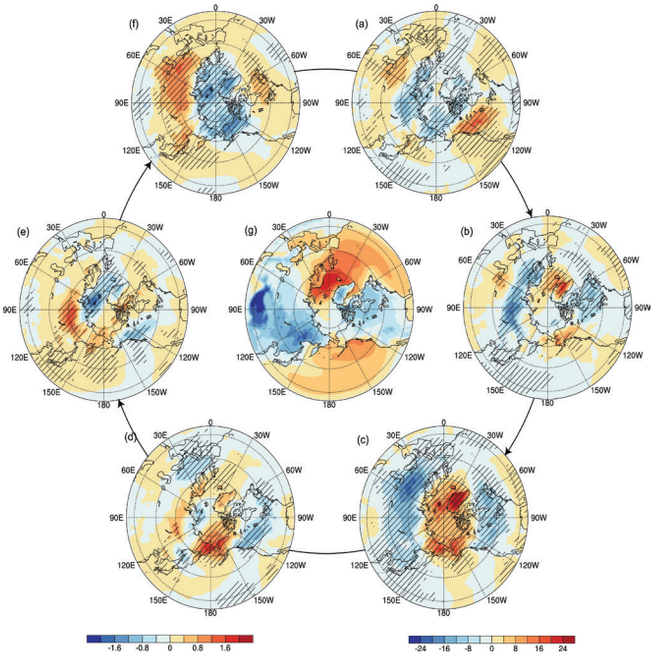

Figure 1: . Composite surface air temperature anomalies (K) in various phases of anomalous WB60N events in the domain of 25–90°N clockwise from top right: (a) −7 to−2, (b) −1 to 1, and (c) 2 to 7 days from the peak dates of weaker WB60N events; and (d)–(f) as in (a)–(c), but for stronger WB60N events. Slashed areas denote the composites are statistically significant above the 95% confidence level. (g) The stationary wave component of the 32-yr-, November–February (NDJF)-mean surface air temperature field. The contours for (a)–(f) are shown in the color bar in the bottom left, and those for (g) are in the bottom right.

circulation across 60°N). One represents CAOs of both North America and Eurasia, and the other is the dominance of CAOs only over one of the two continents with abnormal warmth over the other continent. The first pattern is represented by the composite mean surface air temperature anomalies associated with the stronger mass circulation events (Fig. 1c), and mainly contributed from the phase shifting toward positive polarity of the first and fourth leading empirical orthogonal functions (EOFs) of daily surface air temperature anomalies in winter. The second pattern is manifested by the increased probability of occurrence and amplitude of both phases of the second EOF mode. In contrast, during the cold air charge period (or 1 week after a weaker mass circulation across 60°N), the possibility of the occurrence and amplitude of the two dominant geographical patterns of CAOs are smaller.

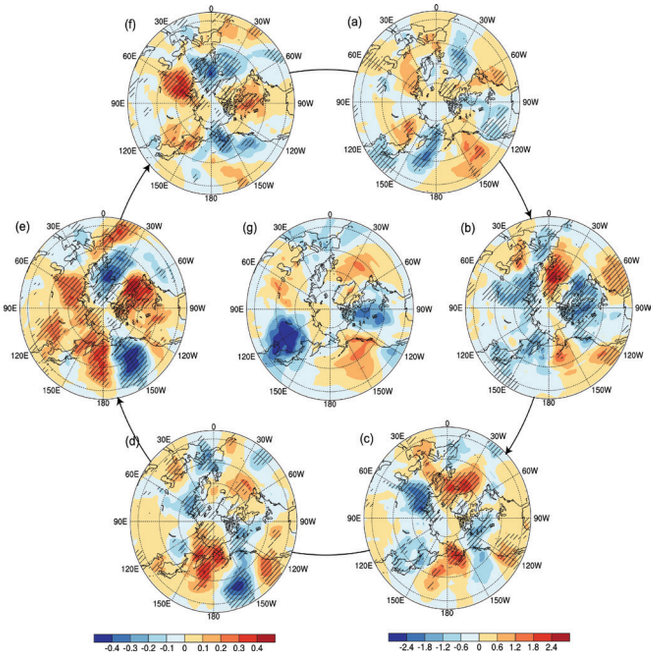

Figure 2: . As in Fig. 1, but for (a)–(f) the anomalies of the total meridional mass transport within the cold air branch (10^9kg s^{-1}) and (g) the corresponding winter climatological mean.

Displayed in Fig. 2 is the composite mean temporal evolution of meridonal mass flux anomalies within the cold air branch, which indicates the routes of cold and warm air mass, from 1 week before to 1 week after the peak dates of stronger and weaker WB60N events. As shown in Fig. 2, composite patterns of circulation anomalies during stronger mass circulation events greatly resemble that of the winter mean, indicating stronger wave activities of wavenumber-2. Accordingly, the cold air mass transport via two main routes of anomalous cold air outbreaks being along the climatological routes of polar cold air, namely, East Asia and North America, is strengthened. Note that the Siberian high shifts westward during stronger mass circulation events, opening up a third route of cold air outbreaks through Eastern Europe, where lies the poleward warm air route in the winter-mean condition. The strengthening of the Icelandic low and Azores high during stronger mass circulation events acts to close off the climatological-mean cold air route via western Europe; this is responsible for the comparatively normal temperature there. The composite pattern for weaker mass circulation events is generally reversed, where the weakening of the Icelandic low and Azores high, corresponding to the negative phase of the NAO, leads to the reopening and strengthening of the equatorward cold air route through western Europe, which is responsible for the cold anomalies there. The second dominant geographical pattern of cold air outbreaks that is closely associated with the WB60N, namely CAOs over one of the two continents, is found to be results of circulation anomalies due to stronger wavenumber-1 wave activities (not shown).

Concluding Remarks

This study proposes a new indicator of CAOs in the framework of isentropic meridional mass circulation. Driven by large-scale waves with deep structure in the extratropics, the warm air mass transported into the polar region tends to vary highly in phase with the polar cold air mass transported out below, thus it has statistically significant and physically direct relationship with individual CAO events. The two most commonly seen spatial patterns of CAO events in winter, namely cold temperatures over mid-latitudes of both continents and cold temperatures over only one of the two continents with the other anomalously warm, tend to occur in the week following stronger meridional mass circulation at 60°N. Details of this study have been presented in Yu et al. (2015a, b).

Moreover, our recent studies (Yu et al., 2015b; Cai et al., 2016) reported that the day-to-day variability of the warm air branch is positively correlated with its stratospheric portion, namely the variations of the poleward mass transport into the polar stratosphere, which is predictable by operational forecast models, such as Climate Forecast System Version 2 (Saha et al., 2014), up to 1 month ahead. This opens up a new opportunity for 30-day forecasts of continental-scale CAOs.

Acknowledgments

This study has been supported by the following projects: National Science Foundation (AGS-1262173and AGS-1354834), the NOAA CPO/CPPA program (NA10OAR4310168), and the DOE Office of RGCM program (DE-SC0004974), the National Basic Research Program of China (2012CB417203), and National Science Foundation of China (41430533, 91437105).

References

Baldwin, M. P., and T. J. Dunkerton, 1999: Propagation of the Arctic Oscillation from the stratosphere to the troposphere. J. Geophys. Res., 104, 30937–30946.

Cai, M., 2003: Potential vorticity intrusion index and climate variability of surface temperature. Geophys. Res. Lett., 30, 1119.

Cai, M., and C.-S. Shin, 2014: A total flow perspective of atmospheric mass and angular momentum circulations: Boreal winter mean state. J. Atmos. Sci., 71, 2244–2263.

Cai, M., Y.-Y. Yu, Y. Deng, H. van den Dool, R.-C. Ren, S. Saha, X.-R. Wu, and J. Huang, 2016: Feeling the pulse of the stratosphere: An emerging opportunity for predicting continental-scale cold air outbreaks one month in advance. Bull. Amer. Meteor. Soc., 97, 1475–1489.

Cellitti, M. P., J. E. Walsh, R. M. Rauber, and D. H. Portis, 2006: Extreme cold air outbreaks over the United States, the polar vortex, and the large-scale circulation. J. Geophys. Res., 111.

Dee, D. P., and Coauthors, 2011: The ERA-Interim reanalysis: Configuration and performance of the data assimilation system. Quart. J. Roy. Meteor. Soc., 137, 553–597.

Ding, Y., 1990: Build-up, air mass transformation and propagation of Siberian high and its relations to cold surge in East Asia. Meteor. Atmos. Phys., 44, 281–292.

ECMWF, 2012; ERA Interim, daily. European Centre for Medium-Range Weather Forecasts. Subset used: 1 November 1979–28 February 2011, accessed 1 July 2012. [Available online at http://apps.ecmwf.int/datasets/data/interim-full-daily/.]

Iwasaki, T., and Y. Mochizuki, 2012: Mass-weighted isentropic zonal mean equatorward flow in the Northern Hemispheric winter. SOLA, 8, 115–118.

Johnson, D. R., 1989: The forcing and maintenance of global monsoonal circulations: An isentropic analy¬sis. Advances in Geophysics, Vol. 31, Academic Press, 43–316.

Konrad, C. E., 1996: Relationships between the intensity of cold-air outbreaks and the evolution of synoptic and planetary-scale features over North America. Mon.Wea. Rev., 124, 1067–1083.

Saha, S., and Coauthors, 2014: The NCEP Climate Forecast System version 2. J. Climate, 27, 2185–2208.

Simmons, A., S. Uppala, D.Dee and S.Kobayashi, 2006: ERA-Interim: New ECMWF reanalysis products from 1989 onwards. ECMWF Newsletter, No. 110, ECMWF, Reading, United Kingdom, 26–35.

Thompson, D. W. J., M. P. Baldwin, and J. M. Wallace, 2002: Stratospheric connection to Northern Hemisphere wintertime weather: Implications for prediction. J. Climate, 15, 1421–1428.

Thompson, D. W. J., and J. M. Wallace, 2001: Regional climate impacts of the Northern Hemisphere annular mode. Science, 293, 85–89.

Yu, Y.-Y., R.-C. Ren, J.-G. Hu, and G.-X. Wu, 2014: A mass budget analysis on the interannual variability of the polar surface pressure in winter season. J. Atmos. Sci., 71, 3539–3553.

Yu, Y.-Y., M. Cai, R.-C. Ren, and H. van den Dool, 2015a: Relationship of warm air mass transport into up¬per polar atmosphere and cold air outbreaks in winter. J. Atmos. Sci., 72, 349–368.

Yu, Y.-Y., R.-C. Ren, and M. Cai, 2015b: Dynamical linkage between cold air outbreaks and intensity variations of the meridional mass circulation. J. Atmos. Sci., 72, 3214–3232.

Yu, Y.-Y., R.-C. Ren, and M. Cai, 2015c: Comparison of the mass circulation and AO indices as indicators of cold air outbreaks in northern winter. Geophys. Res. Lett., 42, 2442–2448.

Walsh, J. E., A. S. Phillips, D. H. Portis, and W. L. Chapman, 2001: Extreme cold outbreaks in the United States and Europe, 1948–99. J. Climate, 14, 2642–2658.

On the Dynamical Relationship Between Equatorial Pacific Surface Currents, Zonally-Averaged Equatorial Sea Level and El Niño Prediction

Xiaolin Zhang, Allan J. Clarke

Earth, Ocean and Atmospheric Science, Florida State University

Contact e-mail: *xz12j@my.fsu.edu*

Introduction

Fundamental to the dynamics of El Niño/Southern Oscillation(ENSO) climate fluctuations is an understanding of equatorial Pacific Ocean flows. Interannual variations in zonal equatorial flow, for example, advect warm water zonally and thus change sea surface temperature (SST), deep atmospheric convection and where the atmosphere is heated (McPhaden & Picaut 1990; Picaut et al. 1996; Jin & An 1999). In spite of the importance of interannul flows to SST and climate fluctuations, the zonal and meridional structure and the physics of these flows are largely unknow. In this table and elsewhere in this study equatorial sea level is based on monthly sea surface height (SSH) anomaly derived from satellite data from AVISO and the surface currents from OSCAR dataset.

At interannual frequencies Gill and Clarke (1974) showed that the large zonal-scale ocean response to wind stress forcing could be described by long wind-forced equatorial Kelvin and Rossby waves. Since Kelvin waves have surface zonal flow in phase with sea level while Rossby waves either have sea level in phase with zonal flow or 180° out of phase with it, the 2 to 3-month lead of the observed flow over sea level in Table 1 must be due some combination of interfering waves. In the eastern equatorial Pacific, the zonal interannual winds that are largely responsible for driving the interannual large zonal scale equatorial flow (see, e.g., the scaling arguments of Clarke, 2008) are weak (Fig. 1). Thus the interfering waves are to a first approximation unforced, and presumably are due to the combination of the Kelvin and Rossby waves associated with eastern ocean boundary reflection. The sum of these waves near an eastern ocean boundary converges very slowly, and this means it is difficult to interpret how the interference leads to a 2 to 3-month lead of zonal flow over sea level. Clarke (1983) showed that near an eastern ocean boundary the sum of the Kelvin and Rossby waves is in the form of long, westward propagating Rossby waves with propagation speed

$$\gamma = \beta c^2 / \beta^2 y^2 = \beta c^2 / f^2 \qquad (1.1)$$

Where β is the northward gradient of the Coriolis parameter f and c is the long internal gravity wave speed

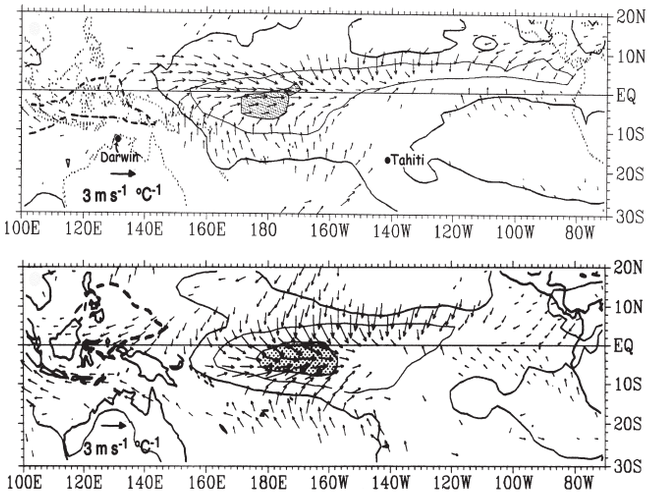

Figure 1: . (top) Regression of July-November surface wind (arrows) and Outgoing Longwave Radiation (OLR) onto an equatorial sea surface temperature (SST) index (July-November SST averaged over 6°S to 6°N, 180°W to 80°W). Wind vectors are only shown for those grid points whose *u* or *v* correlations with the SST index exceed 0.4 in absolute value. The OLR contour interval is 10Wm^{-2}/°C of the SST index; The zero contour is darkened and the positive contour is dashed. Value < -20W/m^2°C are shaded. The wind regressions are based on the period 1946-1985 and the OLR regression on 1974-1989 (1978 missing). (bottom) As for (top) but for December-February. [Redrawn from Deser and Wallace 1990].

for a given vertical mode, y is distance northward. Fedorov (2010) and Clarke (2010) later showed that at interannual and lower frequencies this near eastern boundary theory could be generalized to apply right across the Pacific, and also include wind forcing. In that case the equatorial response could be described in terms of wind-forced equatorial long Rossby waves with speed γ .

In our study these ideas will help us in our focus on the following two goals:

(i) understand the basic physics of why zonal eastern equatorial Pacific flow leads sea level and El Niño indicator; and
(ii) establish the dynamical connection between zonally-averaged equatorial sea level $\overline{\eta}$ and zonal equatorial flow and hence examine why $\overline{\eta}$ leads El Niño indicator.

Why is zonal eastern equatorial Pacific flow an El Niño predictor?

On El Niño timescales, zonal scales are very large. Based on this large zonal scale the eastern ocean boundary within 10^o of the equator acts dynamically like a meridional wall with boundary condition

$$u = 0 \text{ on } x = L \tag{2.1}$$

where u is the eastward perturbation velocity, x distance eastward, L the basin width. At and near this boundary we expect u to be small. This suggests that near the boundary for each vertical mode, in dimensional form, the zonal momentum equation can be written as

$$-fv = -p_x + X \tag{2.2}$$

Here we dropped the mode number subscription n, v is the northward perturbation velocity, p the pressure perturbation due to motion,($p = g\eta$), g the acceleration due to gravity, η the sea level perturbation, $X = \tau^x(\rho_{ref}H)^{-1}$ with τ^x the eastward windstress component, ρ_{ref} the reference seawater density and H is the equivalent depth. With damping and the large zonal scale, low frequency geostrophic approximation for the meridional momentum equation, the remaining governing equations are

$$fu = -p_y \tag{2.3}$$

$$(\partial/\partial t + \lambda)p/c^2 + u_x + v_y = 0 \tag{2.4}$$

where t is the time, λ^{-1} the dissipation time scale. Taking $\partial/\partial x$ of (2.3) minus $\partial/\partial y$ of (2.2) gives

$$fu_x + \beta v + fv_y = -X_y \tag{2.5}$$

Multiplying (2.5) by f and using (2.4) gives

$$\beta fv - f^2(\partial/\partial t+\lambda)p/c^2 = -fX_y \tag{2.6}$$

To obtain an equation for p we divide (2.6) by β and substitute for fv from (2.2) to obtain

$$-(f^2\beta^{-1}c^{-2})(\partial/\partial t+\lambda)p + p_x = -fX_y/\beta + X \tag{2.7}$$

Equation (2.7) is the wind-forced, damped, long Rossby wave equation often used away from the equator, but here used even at and near the equator. To see that (2.7) physically represents wind-forced damped long Rossby waves, consider the solution of (2.7) when there is no wind forcing. Then

$$p(x,y,t) = G(t + (x-L)/\gamma)\exp[(x-L)\lambda/\gamma] \tag{2.8}$$

where γ is the long Rossby wave speed as in (1.1) and G is any differentiable function. The solution represents a long westward propagating Rossby wave that propagates at speed $dx/dt = -\gamma$ and decays with e-folding scale γ/λ corresponding to the distance traveled by the wave in the dissipation time λ^{-1}. Since (2.8) represents damped Rossby waves when there is no wind forcing, the wind-forced equation (2.7) represents wind-forced damped Rossby waves. Under the eastern ocean boundary condition (2.1) and the geostrophic condition (2.3), p is constant along the boundary. Thus in the eastern Pacific at x=L, p is independent of y and the solution (2.8) in the absence of forcing is

$$p(x,y,t) = p_E(t + (x-L)/\gamma)\exp[(x-L)\lambda/\gamma] \tag{2.9}$$

where $p_E(t)$ is the pressure at the eastern boundary. Our interest is in the geostrophic zonal equatorial flow which can be calculated using (2.9). Define

$$t_* = t + (x-L)/\gamma \tag{2.10}$$

Then

$$\partial p/\partial y = dp_E/dt_*(2\beta f)\,(x-L)/(\beta c^2)$$

$$\exp((x-L)\,\lambda/\gamma) + p\,(2\beta f)\,(x-L)\,\lambda/(\beta c^2) \tag{2.11}$$

Since

$$\partial p_E/\partial t = dp_E/dt_* . \partial t_*/\partial t = dp_E/dt_* \tag{2.12}$$

(2.11) reduces to

$$\partial p/\partial y = 2\,(x-L)\,fc^{-2}(\partial/\partial t+\lambda)\,p \tag{2.13}$$

Thus from (2.3) and (2.13)

$$u = 2(L-x)c^{-2}(\partial/\partial t + \lambda)p \tag{2.14}$$

Our study showed that u-field was dominated by the second vertical mode, so the physics of the u-field is captured by (2.14) with $c = c_2$ and $\lambda = \lambda_2$ .Note that p in (2.14) is proportional to the sea level η since the pressure at the surface is $g\eta$. For ease of explaining of the physics described by (2.14), consider first the case where there

Location	η		η_E		h_E		*Niño3.4*	
	max lead month	**max cor (rcrit 95%)**	**max lead month**	**max cor (rcrit 95%)**	**max lead month**	**max cor (rcrit 95%)**	**max lead month**	**max cor (rcrit 95%)**
120°W	2	0.52(0.31)	2	0.56(0.30)	3	0.50(0.31)	4	0.50(0.33)
110°W	3	0.62(0.32)	3	0.61(0.32)	3	0.62(0.33)	4	0.60(0.33)
100°W	3	0.62(0.33)	3	0.62(0.32)	3	0.62(0.34)	4	0.55(0.34)
90°W	3	0.57(0.32)	2	0.57(0.31)	3	0.54(0.31)	4	0.45(0.31)

Table 1: Lead in months corresponding to the maximum correlation between the estimated interannual surface equatorial velocity at various eastern Pacific longitudes and interannual sea level at those longitudes, η_E , h_E (the depth of the 20°C isotherm in the eastern equatorial Pacific), and the El Niño index Niño3.4. Numerical entries in each box correspond to the lead in months at maximum correlation, the maximum correlation and, in brackets, critical correlation coefficient at the 95% significance level. The interannual eastward surface velocity at 120°W was obtained by averaging the interannual u (eastward) velocity from 2°S to 2°N, 130°W to 110°W. Similarly centered 4° by 20° equatorial boxes were used to obtain interannual equatorial u and SSH estimates at 110°W, 100°W and 90°W. The time series for η_E was based on the SSH data averaged over 2°S to 2°N, 82.67°W and h_E was based on the depth of 20°C isotherm data at 0°N, 110°W obtained from http://www.pmel.noaa.gov/tao/disdel/frames/main.html. Monthly data for Niño3.4 was obtained from http://www.cpc.ncep.noaa.gov/data/indices/ The missing monthly data for all 20°C isotherm depth were filled by linear interpolation.

is no damping. Then u is proportional to η_t and hence tells us how η will change in the future. The mathematical reason that u acts like a predictor of η is that u is, by geostrophy, proportional to η_y and η_y is proportional to η_t. The physical reason for this proportionality is that the Rossby wave speed $\beta c^2 / f^2$ decreases rapidly with increasing latitude near the equator. Therefore since all latitudes are in phase at the eastern boundary (where $\eta_y = 0$ because $u = 0$), η at a given longitude at the equator will lead η away from the equator. This implies that calculation of a gradient in latitude is like calculating a gradient in time. The key reason that u leads η is therefore that the low frequency sea level can be described by long unforced Rossby waves leaving the eastern boundary with propagation speed decreasing rapidly with latitude.

When dissipation is included u is proportional to $\eta_t + \lambda\eta = \lambda(\eta+\eta_t/\lambda)$. For low frequencies, by Taylor series expansion

$$\eta\left(t+\lambda^{-1}\right) = \eta(t) + \lambda^{-1}\eta_t(t) \qquad (2.15)$$

Thus u is approximately proportional to $\eta\left(t+\lambda^{-1}\right)$,i.e., u leads η by $\lambda^{-1} \approx 4 months$ for the second vertical mode. This is comparable to the observed lead of 2-4 months shown in Table1.

Note that while the u field is dominated by the second vertical mode, the sea level is dominated by the first two vertical modes. However, since both modes are proportional to each other in the eastern Pacific and proportional to the sea level as a whole, the theory remains consistent with the Table 1 results. Note also that since the thermocline displacement is proportional to sea level, u should also lead the thermocline displacement and therefore El Niño indicator in the eastern equatorial Pacific. Observations are consistent with this. Equatorial u leads thermocline displacement (20°C isotherm depth) by 3 months and Niño3.4 by 4 months.

What is the dynamical connection between zonally-averaged equatorial sea level and zonal equatorial flow and why does $\overline{\eta}$ lead El Niño indicator?

Based on our study, theoretical sea level is well-approximated by the sum of the first two vertical modes, so in the following explanation we shall only analyze these two modes. The zonally-averaged sea level $\overline{\eta}$ on the equator (f=0) can be calculated from the zonal momentum equation (2.2) with $u_t+\lambda u$ term included

$$u_t + \lambda u = -g\eta_x + \tau^x / \left(\rho_{ref} H\right) \qquad (3.1)$$

In previous section for modes n=1 and 2 we have adopted the basic balance between the wind stress and zonal pressure gradient and so have omitted the term.However, based on our study, this zonal velocity term influences the lead of $\overline{\eta}$ over η_E and El Niño. We therefore include this term by regarding it as a perturbation to our previous solution, and estimate it using the lowest order solution, which can be obtained by solving (2.2)-(2.4)

$$u(x,t) = 2gc^{-2}(L-x)\,\partial\eta_E(t)/\partial T - (\rho_{ref}\beta H)^{-1}\int_x^L \tau^x{}_{yy}(s,t)ds$$

$$-2(\rho_{ref}c^2H)^{-1}\,\partial/\partial T\int_x^L (s-x)\,\tau^x(s,t)ds \qquad (3.2)$$

Here and in the following part, we'll write $\partial/\partial T = \partial/\partial t + \lambda$. Integrating (3.1) from some general longitude x to the eastern boundary x=L and calculating the zonal average gives

$$\overline{\eta} = \eta_E - \int_0^L (x/L)\, \tau^x / \rho_{ref} g H \, dx + \partial/\partial T \int_0^L x u^{(0)} / gL \, dx \quad (3.3)$$

Here $u^{(0)}$ stands for the lowest order solution from (3.2), substitude $u^{(0)}$ into (3.3) gives

$$g^{-1} (\partial/\partial T) \int_0^L (x/L) u^{(0)} dx = L^2/3c^2 \, \partial^2 \eta_E / \partial T^2 + J \quad (3.4)$$

where

$$J = -(3 \rho_{ref} H g c^2 L)^{-1} \partial^2 / \partial T^2 \left(\int_0^L x^3 \tau^x dx\right)$$

$$-(2 \rho_{ref} L g H \beta)^{-1} \partial/\partial T \int_0^L x^2 \tau^x_{yy} dx \quad (3.5)$$

our calculations show that the first term on the right hand side of (3.4) dominates. This term is related to the unforced Rossby wave contribution described in section 2. Thus the large zonal-scale low-frequency linear theory suggests that the long Rossby wave physics discussed in section 2 not only explains the lead of u over η_E and El Niño, it also contributes to the lead of $\overline{\eta}$ over η_E. **(This article is a summary of our recent published work (Zhang & Clarke 2016) by Journal of Physical Oceanography. © American Meteorological Society).**

References

Clarke, A. J., 1983: The reflection of equatorial waves from oceanic boundaries. J. Phys. Oceanogr., 13(7), 1193-1207.

Clarke, A. J., 2008: An Introduction to the Dynamics of El Niño and the Southern Oscillation, Academic Press, 324 pp. ISBN: 978-0-12-088548-0.

Clarke, A. J., 2010: Analytical theory for the quasi-steady and low-frequency equatorial ocean response to wind forcing: The 'tilt' and 'warm water volume' modes. J. Phys. Oceanogr., 40(1), 121-137.

Deser, C., and J. M. Wallace, 1990: Large-scale atmospheric circulation features of warm and cold episodes in the Tropical Pacific. J. Climate, 3, 1254-1281.

Fedorov, A.V., 2010: Ocean response to wind variations, warm water volume, and simple models of ENSO in the low-frequency approximation. J. Climate, 23, 3855-3873.

Gill, A. E., and A. J. Clarke, 1974: Wind-induced upwelling, coastal currents and sea-level changes. Deep-Sea Res., 21, 325-345.

Jin, F.-F., and S-I. An, 1999: Thermocline and zonal advective feedbacks within the Equatorial Ocean Recharge Oscillator Model for ENSO. Geophys. Res. Lett., 26, 2989-2992.

McPhaden, M. J., and J. Picaut, 1990: El Niño-Southern Oscillation displacement of the western equatorial Pacific warm pool. Science, 250, 1385–1388.

Picaut, J., M. Ioualalen, C. Menkes, T. Delcroix and M. J. McPhaden, 1996: Mechanism of the zonal displacements of the Pacific Warm Pool: Implications for ENSO. Science 274(5292), 1486–1489, doi:10.1126/science.274.5292.1486. 29 Nov. 1996.

Zhang, X., and A. J. Clarke, 2016: On the Dynamical Relationship Between Equatorial Pacific Surface Currents, Zonally-Averaged Equatorial Sea Level and El Niño Prediction. (Accepted). J. Phys. Oceanogr.

Zhang, X., and A. J. Clarke, 2017: On the Dynamical Relationship between Equatorial Pacific Surface Currents, Zonally Averaged Equatorial Sea Level, and El Niño Prediction, 47, 323-337.

The First and Second Hackathons of the International CLIVAR C20C+ Detection and Attribution Project

Dáithí A. Stone[1], Harinarayan Krishnan[1], Rachel Lance[1], Sebastian Sippel[2], Michael F. Wehner[1]

[1]Lawrence Berkeley National Laboratory, California, U.S.A.

[2]Max Planck Institute for Biogeochemistry, Germany

Contact e-mail: *dstone@lbl.gov*

Extreme weather and climate events are a dominant contributor to overall climate-related risk, and there is a growing realisation that they may also play a major role in past, current, and future trends in climate-related risk in a world under the influence of human activities (Oppenheimer et al., 2014). In order to improve understanding of changes in extreme weather under climate change, the International CLIVAR Climate of the 20th Century Plus (C20C+) Detection and Attribution (D&A) subproject is producing a large number of climate model simulations within an experiment design configured specifically to diagnose the behaviour of extreme weather under climate change (Folland et al., 2014). In order to facilitate analysis by the broad climate research community, the project has held two week-long ``hackathons'' in which researchers from around the world can discuss the project and analyse output on the same machine on which the data portal is hosted.

C20C+ brings together researchers from around the world to develop understanding of variations and changes in the climate over periods up to the last 150 years, through analysis and comparison of observational and dynamical modelling data sets (Folland et al., 2014). Since 2010, C20C+ has been developing this interest into a capacity to understand extreme weather in the context of anthropogenic climate change, through the D&A subproject (http://portal.nersc.gov/c20c). C20C+ D&A is an international collaboration generating a large number of climate model simulations with relatively high resolution atmospheric models, with high frequency output distributed through a public data portal. Current archived output exceeds 3PB.

As part of an effort to facilitate research by the broader climate community, Lawrence Berkeley National Laboratory's CASCADE project and the National Energy Research Scientific Computing Center (NERSC) have hosted "hackathons" in Berkeley, California, during the week before the 2015 and 2016 Fall Meetings of the American Geophysical Union held across the bay. The aim has been to bring together researchers from around the world in order to:

- analyse large quantities of C20C+ D&A data on (and next door to) the machines which host the data portal;
- discuss the experiment design and implementation with researchers who are conducting the simulations;
- coordinate analyses and develop research plans.

Each hackathon involved about a dozen researchers from Africa, Asia, Australia, Europe, and North America, with most participants being early career researchers. The first day of each hackathon was dominated with presentations and discussions about the project, simulations, and NERSC computing systems. For the remaining days the researchers mostly worked on their own analyses on NERSC machines, with occasional spontaneous discussions and impromptu presentations on interesting results or issues, including on methods to estimate uncertainty in risk ratio-based (or fractional attributable risk-based) estimates of the role of anthropogenic emissions on extreme weather (C. Paciorek and colleagues, in preparation) and on the importance of experiment design for attribution assessment (Risser et al., 2017).

While the common and unifying theme of the research was "extreme climate events" and their attribution to human influence, the participants' analyses in both hackathons covered a large variety of different topics, including various simulated metrics and variables, spatio-temporal scales, and analysis methodologies. For example, the breadth of topics included the role and attributability of fire events in Australia, the role of atmospheric modes of variability in extreme events such as heat waves and intense precipitation, interannual

variability and attribution of flooding in Nigeria and southern Africa, and the effect of the land surface on extreme weather. Most of the researchers examined daily output from the climate model simulations, which would be more challenging outside of the hackathon venue.

Both hackathons ended on Friday afternoon with presentations of preliminary results and further analysis plans by all participants. Participants at the 2015 hackathon recommended an emphasis on participation by young researchers. Holding the event alongside the AGU Fall Meeting provides a synergy that is more effective for young researchers than for more mature researchers, who may be in the examination period and have other administrative responsibilities that preclude two weeks of travel. Obtaining travel funding for young researchers, also identified as a way of facilitating participation, helped the 2016 event.

While both hackathons thus far have been considered successful in stimulating and facilitating research, it may be beneficial to modify the approach in future by focusing meetings on specific topics. These could involve a regional focus, hosted anywhere with a high-speed connection to the NERSC portal or through organised staging of data through disk transfers, which would also facilitate travel for young researchers with limited funds in the selected region. There are also identified synergies with other activities which will be actively producing climate model output over the next couple of years, including the Half a degree Additional warming, Prognosis and Projected Impacts Project (HAPPI, Mitchell et al., 2017) (which shares the C20C+ D&A data portal), the Detection and Attribution Model Intercomparison Project (DAMIP, Gillett et al., 2016), Global Monsoons Modeling Intercomparison Project (GMMIP, Zhou et al., 2016), or High Resolution Model Intercomparison Project (HighResMIP, Haarsma et al., 2016), and thus joint hackathon events may be beneficial in facilitating multi-project research.

Participants of both hackathons, as well as the broader climate research community, are invited to submit publications to a special issue in Weather and Climate Extremes concerning "First results of the C20C+ Detection and Attribution Project" (submission deadline 30 June 2017). As with the hackathons, the special issue is intended as a venue to facilitate analyses of C20C+ D&A simulation output, and thus does not preclude publication elsewhere.

Acknowledgments

These hackathons were supported by the Regional and Global Climate Modeling Program of the Office of Biological and Environmental Research in the Department of Energy Office of Science under contract number DE-AC02-05CH11231. They used resources of the National Energy Research Scientific Computing Center, a DOE Office of Science User Facility supported by the Office of Science of the U.S. Department of Energy under the same contract.

References

Folland, C., D. Stone, C. Frederiksen, D. Karoly, and J. Kinter, 2014: The International CLIVAR Climate of the 20th Century plus (C20C+) Project: Report of the Sixth Workshop. CLIVAR Exchanges, 19, 57-59.

Gillett, N. P., H. Shiogama, B. Funke, G. Hegerl, R. Knutti, K. Matthes, B. D. Santer, D. Stone, and C. Tebaldi, 2016: The Detection and Attribution Model Intercomparison Project (DAMIP v1.0) contribution to CMIP6. Geosci. Model Dev., 9, 3685-3697.

Haarsma, R.J., M. J. Roberts, P. L. Vidale, C. A. Senior, A. Bellucci, Q. Bao, P. Chang, S. Corti, N. S. Fučkar, V. Guemas, J. von Hardenberg, W. Hazeleger, C. Kodama, T. Torben Koenigk, L. R. Leung, J. Lu, J.-J. Luo, J. Mao, M. S. Mizielinski, R. Mizuta, P. Nobre, M. Satoh, E. Scoccimarro, T. Semmler, J. Small, and J.-S. von Storch, 2016: High Resolution Model

Participants of the 2015 hackathon in front of NERSC's Cori supercomputer, then one week old.

Participants of the 2016 hackathon during a normal working moment, working on laptops, large screens, and writing on the wall. Images courtesy of M. Wehner and P. Kushner.

Intercomparison Project (HighResMIP v1.0) for CMIP6. Geosci. Model Dev., 9, 4185-4208.

Mitchell, D., K. AchutaRao, M. Allen, I. Bethke, A. Ciavarella, P. Forster, J. Fuglestvedt, N. Gillett, K. Haustein, W. Ingram, T. Iversen, S. Kharin, N. Klingaman, N. Massey, E. Fischer, C.-F. Schleussner, J. Scinocca, O. Se- land, H. Shiogama, E. Shuckburgh, S. Sparrow, D. Stone, P. Stott, P. Uhe, B. Urs, D. Wallom, M. Wehner, and R. Zaaboul, 2017: Half a degree Additional warming, Prognosis and Projected Impacts (HAPPI): background and experimental design. Geosci. Model Dev., 10.5194/gmd-10-1-2017.

Oppenheimer, M., M. Campos, R. Warren, J. Joern Birkmann, G. Luber, B. O'Neill, K. Takahashi, and et alii, 2014: Emergent risks and key vulnerabilities, Climate Change 2014: Impacts, Adaptation, and Vulnerability. Part A: Global and Sectoral Aspects. Contribution of Working Group II to the Fifth Assessment Report of the Intergovernmental Panel on Climate Change, C. B. Field, V. R. Barros, and et alii, eds., Cambridge University Press, 1039-1099.

Risser, M. D., D. A. Stone, C. J. Paciorek, M. F. Wehner, and O. Angélil, 2017: Quantifying the effect of interannual ocean variability on the attribution of extreme climate events to human influence. Clim. Dyn., 10.1007/s00382-016-3492-x.

Zhou, T., A. G. Turner, J. L. Kinter, B. Wang, Y. Qian, X. Xiaolong Chen, B. Wu, B. Wang, B. Liu, L. Zou, and B. He, 2016: GMMIP (v1.0) contribution to CMIP6: Global Monsoons Model Inter-comparison Project. Geosci. Model Dev., 9, 3589-3604.

13th Session of CLIVAR/IOC GOOS Indian Ocean Region Panel

ICPO and IORP co-chairs

From January 30th to February 1st, the CLIVAR/IOC-GOOS Indian Ocean Region Panel (IORP) met for its 13th session in Perth, Australia. The main agenda item of the meeting was the (Indian Ocean Observing System (IndOOS) Review Workshop, jointly organized with the Sustained Indian Ocean Biogeochemistry and Ecosystem Research (SIBER), the IndOOS Resources Forum (IRF) and Global Ocean Observing System in the Indian Ocean (IO-GOOS). The IndOOS Review is being co-ordinated by IORP on behalf of the international community. During the workshop, there were 24 presentations to discuss about the background on the past and present of IndOOS, new scientific drivers in the Indian Ocean, as well as new technologies that could be incorporated to improve IndOOS in the future.

By the end of the workshop, the overall objective of IndOOS, terms of reference of IndOOS Review, and most importantly, the outlines of scientific drivers and observation requirements for IndOOS have been initially identified. The draft IndOOS Review white paper is expected to be delivered by September 2017, and the second IndOOS Review Workshop is planned to be organized in February 2018, together with next IORP meeting. The detailed timelines will be worked out by IORP co-chairs shortly. The IORP co-chairs will also be responsible to contact the individual scientists to compose the white paper written team.

The IORP-13 has been organized back to back with the annual meeting of IOGOOS-13, SIBER-7, IRF-7, the first Scientific Steering meeting of IIOE-2 and Bio-Argo Workshop. More details can be found at http://www.clivar.org/events/iogoosiopsiberirf-annual-meetings-and-1st-iioe-2-steering-committee-meeting-and-bio-argo

CLIVAR Exchanges

No. 71 February 2017

The CLIVAR Exchanges is published by the International CLIVAR Project Office ISSN No: 1026-0471

Editor: Nico Caltabiano (ICPO)
Guest editors: Pascale Braconnot (IPSL, France), Noel Baker (Germany) and Ed Hawkins (University of Reading, UK)

Layout: Harish J. Borse, ICMPO at IITM, Pune, India
Production: Jing Li, ICGPO at FIO, Qingdao, China
Printing of this issue supported by the ICMPO with support of IITM and the Indian Ministry of Earth Sciences, India

सत्यमेव जयते
Ministry of Earth Sciences

The ICPO is supported by China State Oceanographic Administration /First Institute of Oceanography (FIO), Indian Ministry of Earth Sciences/ Indian Institute of Tropical Meteorology (IITM) and NASA, NOAA, NSF and DoE through US CLIVAR.

WCRP is sponsored by the World Meteorological Organization,the International Council for Science and the Intergovernmental Oceanographic Commission of UNESCO.

Contact:
Executive Director, ICPO
First Institute of Oceanography, SOA, 6 Xianxialing Road, Laoshan District, Qingdao 266061, China
icpo@clivar.org
http://www.clivar.org